School of Science
Department of Imaging and Applied Physics

Geopolymer from a Western Australian Fly Ash

Nigel W. Chen-Tan

This thesis is presented for the Degree of
Doctor of Philosophy
of
Curtin University of Technology

December 2010

Declaration

To the best of my knowledge and belief this thesis contains no material previously published by any other person except where due acknowledgment has been made.

This thesis contains no material which has been accepted for the award of any other degree or diploma in any university.

Signature: …….

Date: ……...

Acknowledgements

Nothing is ever done alone even if a person is the only one in the office or a laboratory. There are always senior members, colleagues, students, friends, family and even furry little animals that help in one way or another.

Professor Arie van Riessen is a man of good character who is patient, supportive and full of advice. Thank you for being my supervisor and putting up with my eccentricities.

My thanks go to Curtin University for providing a Curtin University Postgraduate Scholarship (CUPS) and the Centre for Sustainable Resource Processing (CSRP) for a CSRP top-up scholarship.

I would also like to acknowledge the Centre of Materials Research at Curtin University for allowing me access to both the microscopy and x-ray laboratories as well as technical knowledge required for the completion of this thesis with special thanks to Amanda Kirby and Elaine Miller.

My sincerest thanks go out to those who helped me during the Ph.D. To Dr. Daniel Southam and Dr. Robert Hart, thank you for helping me get established in my first year. To Glen Lawson, thanks for helping me out with everything laboratory based. To all the past and present HDR students, thanks for all the good times both fun and embarrassing.

My humblest thanks go to my parents, closest friends and Dr. Jack Faigenbaum. Thank you all for being with me during my roughest times and for helping resolve the large problem that I had.

Abstract

Ordinary Portland cement is utilised worldwide as a mainstay construction material. Worldwide consumption of cement in 2009 was estimated to be 2.8 billion tonnes, which unfortunately equates to the production of 2.8 billion tonnes of CO_2 via the sintering procedure required to produce cement clinkers. With worldwide concern over climate change, this value is a substantial contribution to greenhouse gas emission.

Fly ash is a by-product of coal combustion from thermoelectric power stations. World production of fly ash was estimated at 600 million tonnes with only 9% utilisation (Kayali 2007). The remainder is typically disposed of in landfills or ash ponds. This takes up usable land for development, introduces environmental hazards and can lead to undesirable events with an example being the rupture of a fly ash pond barrier at the Kingston Fossil Plant, Tennessee in 2008 (Reilly 2008) known as the TVA Spill.

Geopolymer is a cementitious binder and is considered an environmentally friendly alternative to cement as it emits no CO_2 during production. Production of geopolymer is a simple process that involves mixing an amorphous aluminosilicate feedstock with alkaline activating solution. In addition this process is able to utilise low cost industrial by-products such as blast furnace slag and fly ash as feedstock.

Although fly ash is suitable as a feedstock for synthesis of geopolymer its inherent heterogeneity limits development of a general formulation for processing geopolymer. Beneficiation of fly ash can be considered a method for alleviating this limitation, leading to a more homogeneous geopolymer with improved properties.

Collie fly ash from Western Australia was selected as the fly ash to investigate as it is the dominant fly ash in the State and had been successfully used previously to make geopolymer. The amorphous content of Collie fly ash was determined by dissolution and a combination of QXRD and XRF. Collie fly ash was

thoroughly characterised by QXRD and XRF, revealing a reactive amorphous content of 54.5 wt.% and secondary phases of carbon, hematite, maghemite, magnetite, mullite and quartz. The amorphous component was found to contain a modest amorphous iron oxide (5.5 wt.%) which after dissolution studies and subsequent analysis by QEMSCAN, was determined not to play a direct role in geopolymerisation. Crystalline quartz was found to exist as primary quartz separate from the fly ash spheres and secondary quartz embedded in the spheres believed to have exsolved from the decomposition of clay in the production of mullite.

Beneficiation of the fly ash was conducted in a three stage procedure using sieving, milling and magnetic separation to improve fly ash homogeneity and reactivity. Sieving was effective in reducing large carbon and free primary quartz content. Interestingly most of the carbon was found to be small and finely dispersed throughout the material making it unfeasible to remove by sieving. Sieving in conjunction with milling increased surface area from 9.83 m^2/g to 10.7 m^2/g. Magnetic separation revealed that the amorphous iron was not magnetic though the complete removal of crystalline iron phases is not possible without a robust separation technique. The removal of magnetic phases increased the surface area of the sieved and milled fly ash to 12.9 m^2/g.

At each stage of beneficiation the proportion of reactive amorphous material increases resulting in increased reactivity. This increase in reactivity necessitated changes in solids:liquids ratio to maintain a workable geopolymer mixture. The least beneficiated fly ash (sieved < 45 µm) produced the strongest geopolymer with a compressive strength of 132 MPa. The most beneficiated fly ash (sieved/milled/magnetically separated) produced geopolymer with the same compressive strength as geopolymer from unmodified fly ash (100 MPa). However, the highly beneficiated fly ash geopolymer proved to be highly resistant to high temperature cracking even after exposure to 900 ºC. The outcomes from this project clearly identifies that different levels of fly ash beneficiation lead to different geopolymer properties which in turn extend the range of applications for which geopolymers can be used.

Contents

Chapter 4 Characterisation of Fly Ash

Chapter 5 Beneficiation of Fly Ash

Chapter 6 Geopolymers from Beneficiated Fly Ash

Chapter 7 Conclusions and Future Work

List of Figures

List of Tables

List of Abbreviations

EDS	Energy dispersive x-ray spectroscopy
LOI	Loss on ignition
MAG-MFA	Magnetic milled sieved fly ash
MAG-SFA	Magnetic sieved fly ash
MAG-UFA	Magnetic unmodified fly ash
MFA	Milled sieved fly ash
NMR	Nuclear magnetic resonance
NM-MFA	Non-magnetic milled sieved fly ash
NM-SFA	Non-magnetic sieved fly ash
NM-UFA	Non-magnetic unmodified fly ash
OPC	Ordinary Portland Cement
PDB	Powder diffraction beamline
PDF	Pair distribution function
QEMSCAN	Quantitative evaluation of minerals by scanning electron microscopy
SEM	Scanning electron microscopy
SFA	Sieved fly ash
UFA	Unmodified fly ash
XAS	X-ray absorption spectroscopy
XAFS	X-ray absorption fine structure
XRD	X-ray diffraction
XRF	X-ray fluorescence spectroscopy

Chapter 1

Introduction

1.1 Fly Ash

Fly ash is an industrial by-product formed during the coal combustion process. Coal combustion is one of the primary methods of energy production utilised internationally due to the abundance of coal. Coal combustion produces a large amount of waste by-products in the form of fly ash and bottom ash. These by-products produce three concerns for the power production industry namely potential ecological damage, health hazards and the locking up of land for storage of fly ash as stockpiles or in ponds (Edugreen n.d.).

Fly ash and bottom ash may contain toxic elements (such as cadmium, lead, arsenic and vanadium), radioactive material (such as uranium, thorium and radium) and organic contaminants (such as polychlorinated dibenzo-p-dioxins and polychlorinated dibenzofurans) and when disposed of in ponds or stockpiles are considered hazardous to natural ecosystems (Edugreen n.d., Goodwin 1993). Fly ash when wet is capable of seeping into the soil, contaminating both ground water sources and soil. Once it has seeped into the ground, it blocks natural drainage systems, causes siltation, alters pH of water sources and renders water non-potable (Edugreen n.d.). Aside from the fly ash itself water is also able to transport impurities (typically trace elements) from the surface of fly ash spheres (Gurba, Heidrich & Ward 2007). Thus fly ash being stored in ponds allows problematic elements (such as Mo, Se, Cr and S) to be readily leached out and contaminate the water. This contaminated water can then be carried to surface water bodies, underground aquifers and to aquatic environments.

Fly ash is often an underestimated health hazard due to the fineness of the particles. Due to the large amount of crystalline silica found within fly ash and the relative ease with which it can become airborne when dry, inhalation may lead to

lung damage causing silicosis. The calcium oxide (lime) content adds to the danger of fly ash as it reacts with water in order to form calcium hydroxide thereby giving fly ash a pH range of a medium to strong base (10 to 12 pH) depending upon the class of the fly ash. Due to this, additional lung damage can occur when inhaled as well as skin damage when the fly ash is stored in a humid or wet climate.

The Ash Development Association of Australia (Ash Development Association of Australia n.d.) claims that during the year 2006/07 an estimated 13.5 Mt of fly ash and bottom ash was produced in Australia and New Zealand of which approximately 6.165 Mt was utilised in applications such as concrete manufacturing. On a world scale, fly ash production is enormous with 600 Mt produced in 2007.

Due to the limited utilisation of fly ash as a marketable product, disposal of the material is a constant priority of coal burning power stations. Fly ash is disposed of either in stockpiles with a sprinkler system to minimise dust or in ash ponds. Regardless of which method of disposal is utilised, a large amount of land is dedicated to this inefficient storage of industry by-product.

There have been concerted attempts at curbing the growing stockpile of fly ash produced internationally. Noticeable efforts include the use of fly ash for:

- Stabilisation of soil for agricultural purposes
- Stabilisation of road base
- Manufacture of insulating bricks
- Additive for cement and concrete
- Landfill applications
- Mine backfill applications

Current utilisation of fly ash reserves is still low, with a majority of its use in cements and concretes as an additive. However, recent development of a relatively new construction based product coined ‘Geopolymer’ the utilisation of a large proportion of stockpiled fly ash maybe possible.

1.2 Geopolymer

Aluminosilicate inorganic polymers, commonly known as geopolymer due to its similarities with geological rock samples, has come to the forefront of construction technology due to its environmentally friendly nature and low cost of production (Davidovits 1991). This is due to the main constituents being abundant and inexpensive and processing producing very little carbon dioxide (CO_2).

Geopolymer production itself does not produce any CO_2 unlike traditional Ordinary Portland Cement (OPC). For every tonne of OPC produced, an equal amount of CO_2 is emitted into the atmosphere (Davidovits 1991). In comparison, it is estimated that for every one tonne of geopolymer produced, there will be approximately 0.1 tonne of CO_2 emitted (Davidovits 1991). This emission is due to the power required for the processing of the geopolymer and the manufacturing of alkaline silicate activator. Geopolymer technology has the potential to supplement the OPC industry thus providing a "green" alternative, utilising low cost materials for products of superior quality and functionality than current OPC mortars and concrete.

Geopolymer is produced by the alkaline activation of aluminosilicate material such as clays and fly ashes. However there are many factors that must be taken into account when creating geopolymer products to ensure consistent mechanical and structural properties.

Fernandez-Jimenez *et al.* (2005) and Palomo *et al.* (1999) stated that the primary variables which have a profound impact upon geopolymer properties are:

- Concentration of chemical species, specifically $[OH]^-$
- Temperature and time of curing
- Type of alkaline element (M)
- Chemical composition of the reactant bulk (Al:Si:M ratio)
- Particle size distribution of the starting fly ash
- Mineral composition of the starting fly ash

The majority of geopolymer literature has focused on the chemical composition of the aluminosilicate precursors and alkaline environment in conjunction with temperature and time of curing to produce the geopolymers with high compressive strength.

Current research is focussing on understanding the effect of the mineral composition of the starting fly ash and the effect it has upon the reaction rate and process as well as the properties of the end product. Fernandez-Jimenez *et al.* (2005) conducted detailed research into the intricate characteristics of fly ash precursor material and related this to the reaction and formation of the geopolymer end product. However, there has been limited investigation into the effect of particle size distribution of the starting fly ash. Fernandez-Jimenez *et al.* (2005) did refer to the importance of particle size distribution to the geopolymer reaction rate and investigations into particle size effect were also presented by Nugteren *et al.* (2009).

1.3 Objectives

This thesis addresses the significance of the fly ash precursor material in regards to the reaction rate and formation of geopolymer. Collie fly ash was selected for the study as it was locally available, abundant and others had demonstrated that it was suitable for production of geopolymer. The specific objectives considered in this study were:

- Determine how chemical, morphology and particle size of Collie fly ash influences the geopolymer reaction and end product characteristics.
- Determine how beneficiation of the fly ash can be used to tailor the geopolymer properties.

1.4 Project Design

Unclassified Collie fly ash was selected as feedstock for this study as it is readily available and underutilised. Coal mined at Collie in Western Australia (213 km south of Perth) is used at several power stations: Collie (Verve Energy), Muja (Verve Energy) and Bluewater (Griffin Energy). Collie fly ash is known to be a very fine powder and to have relatively high iron content in comparison with other Australian fly ashes (Thomas 2005).

Research was divided into three sections. The first section concentrated on the characterisation of Collie fly ash with a focus on the reactive component. The second section focussed on methods of beneficiating Collie fly ash with the aim of increasing the reactivity of the feedstock. The third section compared geopolymer from unmodified Collie fly ash with geopolymer created from beneficiated fly ash. The specifics of the various methods and analysis techniques will be explained in Chapter 3 ‘Experimental Program’. The summary of the project design is presented in Figure 1.1.

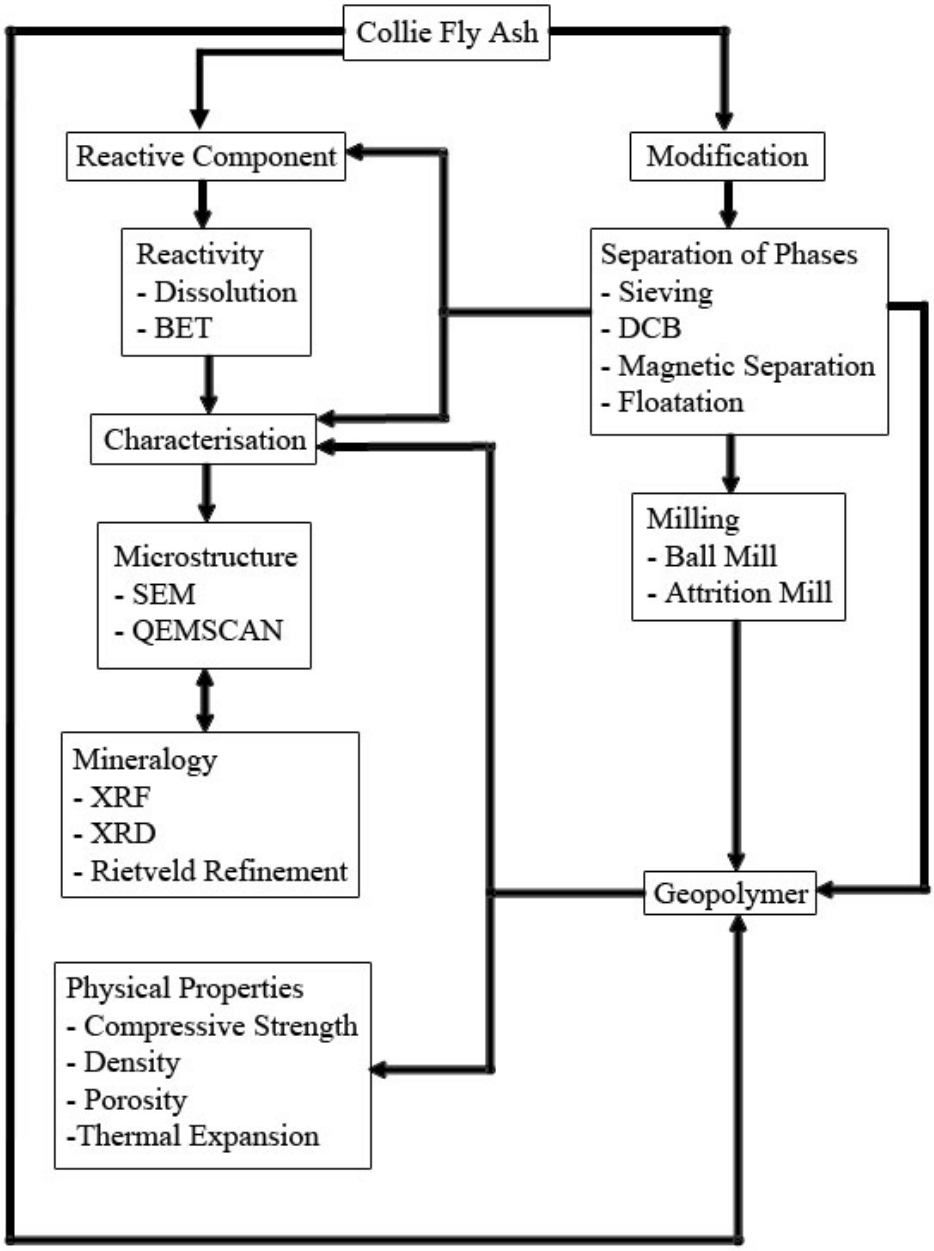

Figure 1.1: Project design.

The section ‘Characterisation of Fly Ash’ will describe various analytical techniques used for the characterisation of Collie fly ash. X-ray fluorescence (XRF) spectroscopy and x-ray diffraction (XRD) were utilised to determine the chemistry and mineralogy of Collie fly ash. Scanning electron microscopy (SEM) was utilised to view the morphology and particle sizes of the various phases. Dissolution studies were conducted to determine the reactive components of Collie fly ash as well as the order in which they are dissolved. Quantitative Evaluation of Minerals by Scanning Electron Microscope (QEM*SEM) marketed as QEMSCAN by Intellection was conducted to confirm results from x-ray analysis and SEM.

The second section ‘Beneficiation of Fly Ash’ describes the various methods used to separate secondary phases from the amorphous aluminosilicate component in Collie fly ash including methods for increasing surface area of the reactive component. Dissolution studies, SEM, XRD and XRF were utilised to analyse the effectiveness of the various methods in regards to the improvement of the reactivity of the Collie fly ash feedstock.

The third section ‘Geopolymers from Beneficiated Fly Ash’ compares the geopolymer made from as provided Collie fly ash with the geopolymers made from enhanced Collie fly ash. Compressive strength was the primary method used to assess the quality of the geopolymer. This was supported by SEM, XRD and XRF analysis.

Chapter 2

Literature Review

2.1 Fly Ash

Fly ash is the non-volatile, incombustible, thermally altered fine mineral powder formed during the coal combustion process. The primary content of fly ash is the x-ray amorphous aluminosilicate that is formed by the melting of clays and resulting ex-solution of mullite from the melt (Scheetz n.d).

It is known that fly ashes are materials that can contain trace amounts of toxic elements (such as cadmium, lead, arsenic and vanadium) and organic contaminants (such as polychlorinated dibenzo-p-dioxins and polychlorinated dibenzofurans) depending upon the locality of the coal basin and the associated mineral deposits from that region (EduGreen: Fly Ash n.d., Goodwin 1993). The ponds or stockpiles used to store fly ash are considered hazardous to natural ecosystems. Fly ash and its leachants are capable of seeping into the soil, contaminating both ground water sources and soil. Once it has seeped into the ground, it has the potential to block natural drainage systems, cause siltation, alter the pH of water sources and decreases water potability.

The primary concern about utilising fly ash as a feedstock for the synthesis of geopolymer is the variability that occurs with fly ash formation. It is known that fly ash differs from region to region due to the variation in coal composition. This variability is transferred to the fly ash created after the coal has been combusted to produce electricity. It is also known that fly ash variability occurs at the same thermoelectric power stations using the same coal feedstock due to changes in operating conditions (Thomas 2005).

Global production of fly ash was estimated to be 600 million tonnes with a trifling 9% utilisation (Kayali 2007). Utilisation of the by-product has increased in

the past decade for both agriculture and building materials (Ash Development Association of Australia n.d.), especially as a lightweight aggregate to high performance concrete (Malhotra & Mehta 2002, Kayali 2007). An indication of the increased rate of usage was provided in Chapter 1 where in 2006 to 2007, Australia and New Zealand produced 13.5 Mt of fly ash and bottom ash with approximately 7.3 Mt bring stored in tailings dams (Ash Development Association of Australia n.d).

2.1.1 Mineralogy

Coal is primarily composed of carbon, hydrogen and oxygen with minor amounts of nitrogen, sulphur and non-combustible impurities consisting of clay, feldspar, limestone, quartz and shale (Malhotra & Mehta 1996). The amount of impurities found within the coal is dependent upon the quality of the coal and ranges from 10 to 40 weight percent (Malhotra & Mehta 1996).

Fly ash is a residue created by coal-fired thermal power plants. Finely ground coal is passed through an incinerator, where combustibles are consumed and the non-combustible mineral impurities are fused. The impurities are suspended in the flue gas and undergo rapid cooling after passing through the high-temperature zone, generally transforming into solid spherical glassy particles. Particles that are suspended in the flue gas are generally transported with the gas to cleaning systems such as mechanical separators and electrostatic precipitators, however a small amount does collect together to form bottom ash (Goodwin 1993, Malhotra & Mehta 1996). Approximately 75% of fly ash is produced with a particle size of less than 45 μm (Malhotra & Mehta 2002).

The morphology of fly ash varies but is predominantly spherical. Particle morphology is controlled by the processing conditions of the coal burning and primarily by the combustion temperature and cooling rate (Kutchko & Kim 2006). When the coal is passed through the high temperature region of the furnace (1400 °C – 1700 °C), the feedstock liquefies into molten droplets which is then cooled rapidly after leaving the region (Kutchko & Kim 2006, Chung & Smith 2000). The majority of the molten droplets are comprised of aluminosilicate glass. The spherical droplets are capable of encapsulating crystalline material (such as iron oxides and mullite)

due to surface tension. However, crystalline phases formed on cooling or those that did not melt nor react during the time spent in the high temperature region will not be spherical. These non-spherical crystalline phases tend to be quartz particles, iron oxides derived from pyrite oxidation (which have not agglomerated with the aluminosilicate glass), and carbon particles of incompletely combusted coal (Chung & Smith 2000).

An in-depth study into the characterisation of the inorganic chemical composition of individual fly ash particles was conducted by Ramsden and Shibaoka (1982) using optical and electron microscopy in conjunction with quantitative electron microprobe analysis. This study resulted in classification of seven categories of fly ash particles. The categories are as stated by Ramsden and Shibaoka (1982):

(1) Unfused detrital minerals (principally quartz)
(2) Irregular-spongy particles derived from partly-fused clay minerals
(3) Vesicular colourless glass (in the form of irregular particles and cenospheres) derived from viscous melts
(4) Solid glass (mostly in the form of spherical particles and sometimes pigmented) derived from fluid melts
(5) Dendritic iron oxide particles (mostly spherical) containing variable amounts of glass matrix
(6) Crystalline iron oxide particles (mostly spherical) containing minimal amounts of glass
(7) Unburnt char particles.

Composition of fly ash differs depending upon the quality and type of coal combusted. ASTM Standard Specification C 618 identifies two classes of fly ash. Class F fly ash is created by the combustion of anthracite or bituminous coal and has low calcium content. Class C fly ash is created by the combustion of lignite or sub-bituminous coal and has high calcium content. Fly ash tends to have high levels of silica (50 to 90 percent) with moderate levels of alumina (Malhotra & Mehta 1996). Chemical composition and reactivity of the silica is dependent upon the calcium content of fly ash, thus the aluminosilicate glass found in Class F fly ash is less reactive than its calcium aluminosilicate glass counterpart found in Class C fly ash

(Malhotra & Mehta 1996). Class F fly ash typically contains the minerals hematite (Fe_2O_3), magnetite (Fe_3O_4), mullite ($3Al_2O_3.2SiO_2$), quartz (SiO_2) and sillimanite ($Al_2O_3.SiO_2$), while Class C fly ash contains alkali sulphate anhydrite ($CaSO_4$), calcium aluminosulphate ($4CaO.3Al_2O_3.SO_3$), free CaO, periclase (MgO), quartz (SiO_2) and tricalcium aluminate ($3CaO.Al_2O_3$) (Malhotra & Mehta 1996, Chung & Smith 2000). Kutchko and Kim (2006) state that iron-rich spheres are comprised of an iron oxide component and an amorphous alumino-silicate according to elemental analysis conducted with SEM. Chung and Smith (2000) state that the iron bearing particles are typically hematite (fully oxidised iron) or magnetite (partially oxidised iron) and occasionally maghemite. These iron oxide components ranged in texture or form from sphere to sphere. Calcium-rich material was determined to be distinctly different in both elemental composition and texture from the standard amorphous alumino-silicate spheres. The calcium-rich material was not associated with silicon or aluminium, but was instead associated with sulphur or phosphorous. The majority of the large particles were determined to be unburnt carbon however hollow cenospheres are also present as large particles. Agglomerated and irregularly shaped amorphous particles were speculated to be caused by inter-particle contact or rapid cooling.

Previous studies by Hinckley *et al.* (1980), Hower *et al.* (1999), Patil *et al.* (1983) and Warren and Dudas (1988) determined that iron bearing phases in fly ash are dependent upon the coal consumed during the combustion process. Typical iron bearing phases in bituminous coal fly ash as noted by Hower *et al.* (1999) include magnetite, hematite, goethite, Fe^{2+} and Fe^{3+} mixed spinels, Fe^{3+} bearing mullite and Fe^{2+} and Fe^{3+} silicates. It was noted that under oxidising conditions in excess of 1500 °C, the dominant fly ash phases are Fe^{2+} glass and Fe-Al spinels, while at temperatures below this threshold, approximately 50% of total Fe in the fly ash is found in Fe^{3+} glass with the remainder found as hematite and Ca-Mg ferrite spinel. Font *et al.* (2004) collected Mössbauer and XAFS spectroscopy data that agreed with observations from Hower *et al.* (1999) where iron was found to be predominantly Fe^{2+} in glass with minor amounts of Fe^{3+} and Fe sulfides. Hower *et al.* (1999) determined that the magnetic fractions in fly ash have abundant spinels and significant quantities of glass phases due to mixed magnetic/non-magnetic particles. Patil *et al.* (1983) notes that almost all fly ash contains iron in a variety of chemical

states such as complex oxides, silicates or sulphates. Hinckley *et al.* (1980) stated that fly ash contained six main types of iron containing phases that can be divided into two groups, one being iron oxides and the other iron ions in silicate. The iron oxide group consist of hematite, magnetite and goethite, while the iron ions in silicate contained three species, one ferric and two ferrous. Hinckley *et al.* (1980) also noted that the percentage of iron present as oxide varied from batch to batch of fly ash even though they came from the same power station.

2.1.2 Utilisation of Fly Ash

Many thermoelectric power stations dispose of their fly ash by mixing with water and transporting the slurry to holding or disposal ponds nearby. This process is not sustainable and there is a strong push to identify ways that fly ash can be utilised to create beneficial products (Chung & Smith 2000). These include:

- Fly ash as a mineral admixture for cement and concrete
- Fly ash as road sub-base and embankments
- Fly ash for soil conditioning

Despite the utilisation of fly ash in the applications listed above, a vast majority of the fly ash is disposed of in ash ponds which are eventually covered and converted to permanent landfills, conventional landfills or landfills at coal mine sites (Chung & Smith 2000).

However, due to the presence of the amorphous aluminosilicate in fly ash, there is the potential for full utilisation of fly ash as a cement replacement. The x-ray amorphous spheres can be alkali activated to make geopolymer cement. Placing the fly ash in an alkaline environment with a pH greater than 9.5 results in dissolution of the amorphous aluminosilicates followed by the formation of hydration products (Scheetz n.d). If the alkaline solution is alkali metal based (lithium, sodium potassium, rubidium, caesium and francium), the hydration products are proto-zeolitic phases. However if the solution is alkali earth metal based (beryllium, magnesium calcium, strontium, barium and radium), the hydration products are hydrous earth metal aluminosilicates which are equivalent to the hydration products

of Portland cement (example: Ca products hydrous calcium aluminosilicates C-A-S-H) (Scheetz n.d.).

Fly ash has the potential to be utilised in larger amounts if its chemical and physical nature is known. By understanding the mineral and bulk chemical composition of the fly ash, it can be made into a viable commodity instead of being viewed as an environmental pollutant.

2.2 Geopolymer

The word Geopolymer was coined for the cement-like material produced by alkali activation of amorphous aluminosilicate feedstock (Davidovits 1991). Geopolymer is a potential industrial material that can change the current image of industrial waste as a problem into a resource for production of useful by-products.

Typically geopolymers have been based around natural mineral aluminosilicates (kaolinite and meta-kaolinite) as they contain fewer impurities (Rowles 2004, Subaer 2004) however the use of industrial waste products containing the required amorphous aluminosilicate phase have been identified as a viable and low cost feedstock.

Current trends in research show an emphasis into the utilisation of different forms of aluminosilicate precursor material to produce geopolymers. Alternative aluminosilicate sources include industrial wastes such as fly ash, furnace slags, Bayer residue and pozzolans. Because of their potential for elimination of industrial waste products, aluminosilicate inorganic polymers are seen to have economical as well as environmental benefits. Economical benefits arise because primary industries are able to safely dispose of possibly toxic and previously unusable wastes.

The general consensus of geopolymer creation is that hydrothermal condensation polymerisation occurs after the amorphous aluminosilicate feedstock has reacted with an alkaline/alkaline silicate solution yielding a glassy geopolymer phase. This cement-like product has impressive mechanical properties and superior chemical and fire resistance when compared to traditional OPC.

Typical properties of aluminosilicate inorganic polymers are high early strength, compressive strength greater than OPC, acid resistance, freeze/thaw resistance and heat resistance (Davidovits 1994). The rapid condensation polymerisation yields structural integrity and reasonable strength in a relatively short time. Development of approximately 20% to 30% of final compressive strength can be achieved in the first few hours of setting and steadily increases with age. With its high strength and resistance to acid, aluminosilicate inorganic polymers can be theoretically utilised in toxic waste containment and in the construction of durable structures (Davidovits 1991, Davidovits 1994, Khalil & Merz 1994, van Jaarsveld *et al.* 1997, van Jaarsveld *et al.* 1998, van Jaarsveld *et al.* 2002, Izquierdo *et al.* 2009).

2.2.1 Proposed Geopolymer Chemistry

Due to the complex chemistry of geopolymer formation, the chemical process isn't completely understood. The accepted theory of geopolymer synthesis is that the formation mechanism for geopolymers is a hydrothermal condensation reaction similar to that utilised in the conversion of amorphous glass into zeolites (Alkan *et al.* 2005, Cundy & Cox 2005, Davidovits 1994, Inada *et al.* 2004, Murayama *et al.* 2001, Xu & van Deventer 2000). The hydrothermal condensation reaction of the aluminosilicate precursor material occurs with the addition of alkali metal hydroxide and/or silicate solution. This reaction leads to the conversion of the amorphous feedstock to a secondary amorphous material (geopolymer). The dissolution process results in a breakdown of covalent bonds Si-O-Si and Al-O-Al with the Al and Si ions passing into the solution. The condensation process forms a network heteropolymer composed of SiO_4 and AlO_4 tetrahedra joined by an oxygen bridge (Barbosa *et al.* 2000, Cundy & Cox 2005, Davidovits 1991, Davidovits 1994).

Davidovits (1991, 1994) predicted that geopolymers are comprised of amorphous silicon-oxo-aluminates (sialates) monomers in a network arrangement. The polysialates can be expressed by the empirical formula:

$$M_n\left[-\left(SiO_2\right)_z-\left(AlO_2\right)-\right]_n \qquad (2.1)$$

where M is a monovalent cation (alkali metal/earth metal), n is the degree of polymerisation and z ranges between the values of 1 and 3. The monovalent cation is required to balance the negative charge introduced by the presence of Al^{3+} in four-fold coordination. Alkali metals or alkaline earth metals are typically utilised as the cation, usually Na^{+}, K^{+}, Ca^{2+} or Mg^{2+}.

Barbosa *et al.* (2000) measured change in viscosity during the polymerisation of geopolymer mixtures and concluded that the polymerisation reaction is similar to the 'gel effect' which occurs during radical polymerisation. Xu and van Deventer (2000) complement this information by stating that before setting proceeds, the dissolution of Al and Si from aluminosilicate starting materials in alkaline solution produces hydrated reaction products in the form of $[M_x(AlO_2)_y(SiO_2)_z.n\text{MOH}.mH_2O]$ gel. The formation of this gel is dependent upon the extent of dissolution of the starting aluminosilicate material. A layer of the gel is formed on the surface of the starting material as it reacts with the alkaline solution. The gel then spreads from the surface of the particle into larger interstitial spaces between neighbouring particles with precipitation of gel and the simultaneous dissolution of the neighbouring particles. When the gel hardens, the neighbouring particles are tightly bound together (Xu & van Deventer 2000).

NMR studies of geopolymer identified a lack of long-range atomic order which is confirmed by x-ray diffraction (XRD) results (Barbosa *et al.* 2000). This indicates that geopolymers show structural characteristics similar to glasses or hydrated silicate minerals in having a range of Si environments but predominantly those of framework structures saturated in Al (Figure 2.1).

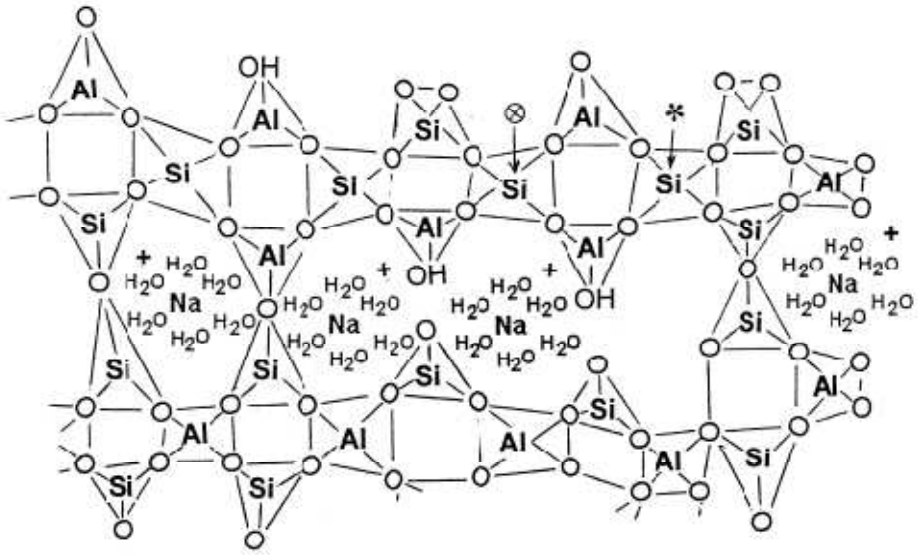

Figure 2.1: Proposed semi-schematic structure for Na-polysialate polymer (Barbosa *et al.* 2000).

Zeolite synthesis is seen to be similar to that of geopolymer synthesis where a hydrothermal condensation reaction is utilised to digest the starting SiO_2 and Al_2O_3 sources using highly concentrated alkaline solution. Cundy and Cox (2005) described the zeolite synthesis process as formations of two amorphous phases prior to the crystallisation of the final amorphous phase into zeolite (Figure 2.2). The two amorphous phases were titled primary and secondary amorphous phase. The initial primary amorphous phase is described as the immediate product of the feedstock and alkaline solution. This phase is a non-equilibrium heterogeneous product containing precipitated amorphous aluminosilicate material in conjunction with precipitated silica/alumina and unreacted starting material. The primary amorphous phase is converted to the secondary amorphous phase with time or upon. This secondary amorphous phase product is a pseudo steady state intermediate which will eventually be dissolved by the alkaline solution, re-precipitate and crystallise via nucleation into its equivalent zeolite product with a similar Si:Al ratio. It can be said that the evolution from the primary phase via the secondary phase into the final zeolite phase is also an evolution of order as the long range of the atoms in the matrix is tightened at each step.

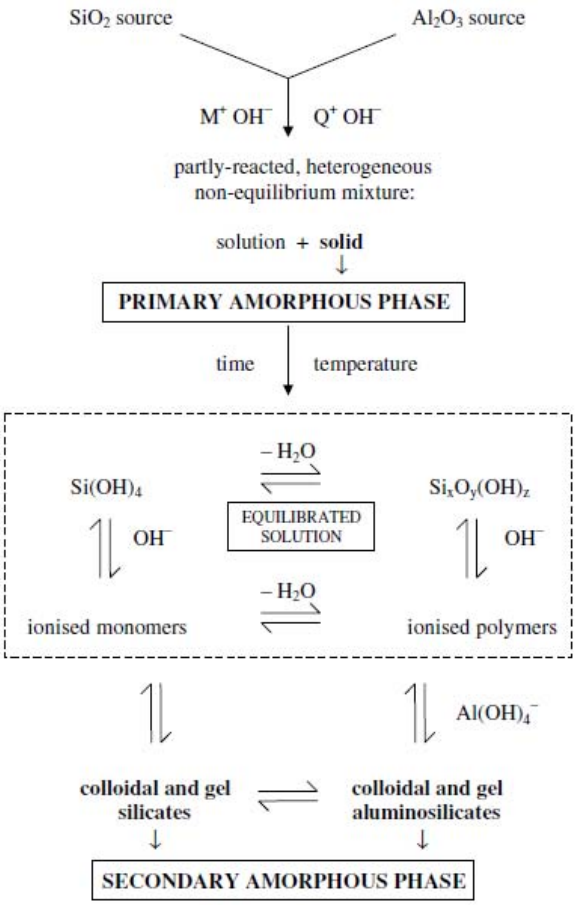

Figure 2.2: Equilibrium of starting material to the formation of the partly ordered secondary amorphous phase (Cundy & Cox 2005).

It is mentioned in the extensive literature review of zeolite synthesis by Cundy and Cox (2005) that zeolite research groups believe this secondary amorphous phase contains a short-range order of Al and Si atoms which is similar to the crystalline zeolite which would form with further hydrothermal treatment. Therefore it is believed that the formation of geopolymer is the same process utilised in zeolite synthesis except that minimal liquid content is utilised to cease the reaction at the metastable pre-zeolite secondary amorphous phase which the author believes is commonly known as geopolymer gel.

Provis and van Deventer (2007a, 2007b) conducted modelling and experimental research into the kinetics of geopolymerisation. They predicted the formation process to consist of the dissolution of starting aluminosilicate source material with the alkaline activating solution, followed by the formation of an initial

amorphous gel phases followed by its transformation into the final amorphous gel phase. This concept is not dissimilar to that described for zeolites synthesis prior to the nucleation and crystallisation of zeolites. The proposed reaction sequence of geopolymerisation by Provis and van Deventer (2007b) (Figure 2.3) includes an aluminosilicate 'nuclei' component which suggests the formation of zeolitic phases as the next step.

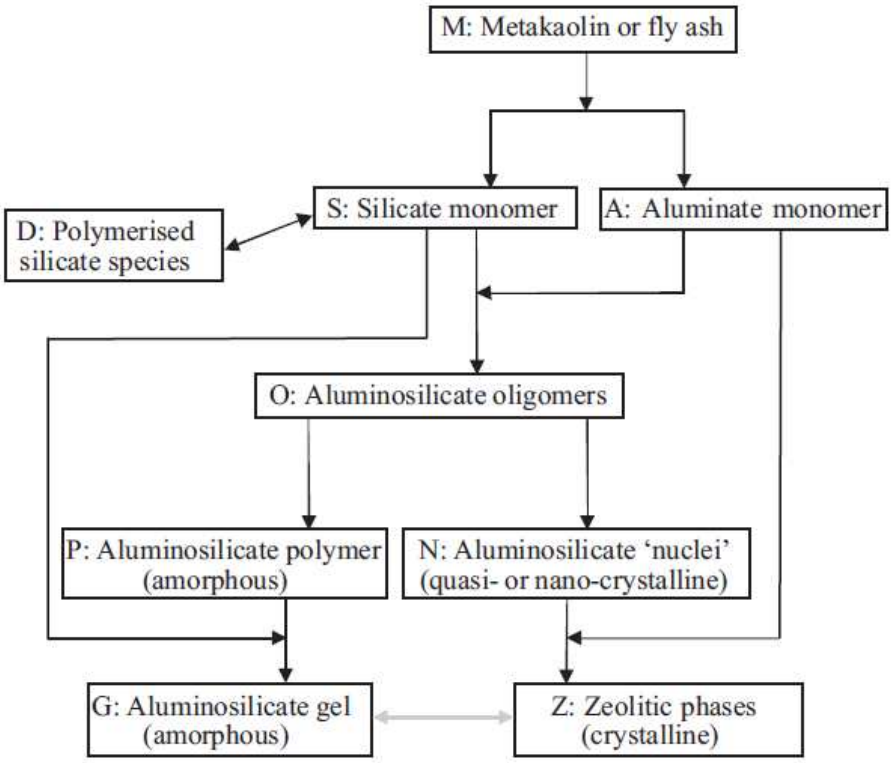

Figure 2.3: Proposed reaction sequence by Provis and van Deventer (2007b).

The exact reaction mechanisms of the dissolution, gel formation, setting and hardening process are still not fully understood due to the complexity of the process. This is in part due to the inherent heterogeneity of fly ash and the multitude of crystalline phases found alongside the amorphous content. The more common analytical techniques used to study bonding and coordination number of the Si, Al and Na atoms (NMR, PDF, XAS, XRD) only provide averaged information about the amorphous starting material, geopolymer gel and crystalline content due to large sample size needed for analysis. TEM and some of the synchrotron based microspectroscopy techniques are starting to provide information at the nanoscale

level albeit very slowly. A significant level of international research is devoted to the understanding of the geopolymer process.

2.2.2 Effect of Different Processing Variables

Synthesis of aluminosilicate inorganic polymers is typically the combination of alkaline activator with an amorphous aluminosilicate feedstock. The main factors that have been identified that influence the properties of aluminosilicate inorganic polymers are:

- Amorphous aluminosilicate content in precursor
- Type of alkaline activator utilised
- Type and fineness of aluminosilicate precursor
- Si:Al:M ratio
- Curing temperature
- Water:solids ratio
- Type and amount of other additives

The amount of amorphous aluminosilicate in the fly ash is of primary interest as it will directly impact the amount of geopolymer that can be formed. Due to the varying quality and composition of coal, the resultant fly ash will undeniably alter over the operating life of the power station. To ensure the synthesis of geopolymer with consistent physical, chemical and mechanical properties, it is necessary to know the amount and content of the amorphous aluminosilicate and to understand how differences in the amount of Al and Si affect the properties of the geopolymer.

Nuclear magnetic resonance (NMR) studies by Barbosa *et al.* (2000) indicate that optimum formation and curing of NaOH activated geopolymer occurs when the sodium content is sufficient to satisfy charge-balance requirements. Excess alkaline salts post geopolymerisation can be transported to the surface with pore water during the curing process and react with CO_2 (carbonation) in air, resulting in efflorescence.

The choice of alkali activator, for example hydroxide or silicate solution has a pronounced effect upon geopolymer properties. The choice of alkali-metal cation affects the extent of dissolution of the aluminosilicate starting material which is required for the formation of the geopolymer framework.

Dissolution studies conducted by Xu and van Deventer (2000) demonstrate that NaOH results in greater dissolution of Al and Si than KOH of the same concentration. It was also noted that the high concentrations of Si in solution was not only due to the higher concentration of Si in the source materials, but also the higher rate of dissolution of Si relative to Al (Xu & van Deventer 2000).

The ionic sizes of alkali-metal cation also affect the dissolution rate. Na^+ and K^+ have the same electric charge however their ionic sizes are different with Na^+ being smaller than K^+. NaOH solution exhibits a higher dissolution rate with aluminosilicate source materials as the smaller Na^+ cation is the favoured ion-pair reaction with smaller silicate oligomers (Xu & van Deventer 2000). This is due to cation-anion pair interaction becoming less significant as the cation size increases. However, it must be noted that KOH based geopolymers produced higher compressive strength results even though there is a higher extent of dissolution with NaOH. Xu and van Deventer (2000) believe that this occurs due to all lengths of silicate oligomers found in alkaline solutions of Al and Si ions are capable of forming Al-O-Si complexes. It is believed that $Al(OH)_4^-$ does not readily combine with small highly charged silicate oligomers leading to the theory that the more long-chain silicate oligomers that exist, the more readily the geopolymer precursor gel forms. The larger ionic size of K^+ favours the formation of larger silicate oligomers which in turn prefers to bind with $Al(OH)_4^-$. This produces a greater quantity of gel precursor which results in better setting and compressive strength. Kriven and Bell (2004) state that variation of alkali choice maybe utilised as a means of tailoring pore size. Their studies indicated that mean and median pore size consistently decreased as concentration of KOH increased. Electron microscopy of geopolymer showed that pore morphology is non-uniform with a wide distribution of sizes.

NaOH plus sodium silicate have been found to produce the fastest setting time and promotes the collapse of both micropores and mesopores, thus increasing

density and strength (Jiang 1997). Chemical stability of fly ash is relatively low due to the high rate of leaching that occurs (Jiang 1997). The ratio of the activation solution to the fly ash has significant effect on both ultimate strength and strength development of the polymers. With higher ratio of fly ash to alkaline solution, a higher strength paste is produced (Xie *et al.* 2001, Bakharev 2005). One of the reasons proposed for the higher strength development with higher solids to liquid ratio was that it prevented formation of zeolites. Si:M ratio is also important and must be optimised to obtain the best strength results. García *et al.* (2006) determined that strongly alkaline solutions are required for dissolution of fly ash due to the inherent porosity present in the resultant geopolymer which is believed to be the cause of the strength reduction in pure and composite fly ash pastes. Rees *et al.* (2004) state that the presence of silicates in the activating solution causes the variation of exposed geopolymer surfaces. This alters dissolution and precipitation reactions as the amount of soluble silica in the system has an effect on gel microstructure. García *et al.* (2006) noted that fly ash pastes activated with NaOH only, did not reach acceptable strengths which is believed to be partly due to the resultant low Si:Al ratio.

The composition of the aluminosilicate inorganic polymer can be manipulated by altering the activating solution to achieve Si:Al, M:Al and Si:M values to attain specific physical properties. Rowles and O'Connor (2003) compared compressive strength results of metakaolin based geopolymer with different Si:Al:M ratios to determine the effect upon microstructure. For low and medium strength samples, heterogeneity was prevalent, with the presence of large grains reminiscent of metakaolin precursor. This clearly indicates incomplete dissolution of the metakaolin. High strength samples still showed a 'grain' structure however they were more homogeneous. This microstructural heterogeneity was explained by Rowles and O'Connor (2003) to be dependent upon the Si:Al:Na ratio. In the reaction process, the amounts of OH^- and Na^+ are coupled indicating that a sufficient amount of NaOH is required in the activating solution. With insufficient amounts of NaOH solution, there would be insufficient OH^- to completely dissolve Si^{4+} and Al^{3+} from the aluminosilicate starting material. However, excess NaOH was found to weaken the structure of the geopolymer.

Rowles (2004) states that due to the Loewenstein avoidance principle, a low Si content will reduce geopolymer compressive strength. When a single O bridge links two tetrahedra, Al can occupy the centre of only one. When there is low Si content, the reaction cannot produce large enough polymer networks to promote high structural integrity. However, with a very high Si content, compressive strength is decreased as there is insufficient OH^- (from the alkaline solution) to fully dissolve the Al^{3+} ions (Rowles & O'Connor 2003) leading to an increase in the content of undissolved precursor material. This was confirmed by Fletcher *et al.* (2004) who conducted a similar study to Rowles and O'Connor (2003) with the exception that only the Si:Al ratio was altered.

Lee and van Deventer (2004) confirmed the importance of the Si:Al:M ratio and demonstrated that a silicate solution can be used to obtain an optimal Si content. In experiments involving the observation of the interface between natural siliceous aggregates and geopolymers they noticed that when the Si content in the activating solution was low, compressive strength of the geopolymer was low regardless of alkaline concentration. With an optimal Si:Al:M ratio obtained using soluble silicate the aggregate and binder interface contact area was greater leading to strong interfacial bonding. With low Si:Al, the interface between aggregate and geopolymer binder was found to be very porous.

Dent Glasser and Harvey (1984) conducted studies on gelation of potassium aluminosilicate solution to create zeolites. As the formation of geopolymers is believed to be the precursor to the formation of zeolites, the science underpinning zeolite formation is considered to be compatible with geopolymer formation. The authors determined that gelation times are dependent upon alkali and silica concentration. With low silica concentration, gelation time increased with excess alkali present, whilst for high silica concentration gelation increased with less excess alkali present. Other alkali cations (sodium, caesium and tetramethylammonium) were substituted for potassium and were found to have a noticeable effect on solution behaviour. Sodium based systems tended to increase reaction time with increasing alkali regardless of the silica content. The sodium based system also improves reaction times compared to potassium based systems. Caesium based systems had longer gelation times than the potassium solutions, especially for high silica content

solutions. Tetramethylammonium based systems are complicated by formation of crystalline aluminosilicate compounds from high silica:high alkali solution.

Dissolution studies (Weng *et al.* 2005) have revealed that the composition of the geopolymer matrix will be different from that estimated from the composition of the metakaolin precursor material. This is because only partial dissolution of the starting material will occur due to the shielding effect of agglomerated particles, inability of some phases to dissolve into solution, limited surface area of the starting material and insufficient concentration of the alkaline activating solution. Weng *et al.* (2005) noted an increased dissolution rate with an increase in surface area of the metakaolin by grinding.

Xu and van Deventer (2000) found, as expected, that the amount of Al and Si material utilised from a starting material is dependent upon the particle size. With finer particles sizes (< 0.5 μm) there is a higher level of dissolution. However, there will always be some unreacted aluminosilicate material that will remain present as fine filler in the microstructure. Weng *et al.* (2005) noticed that geopolymer created without milling of precursor metakaolin was heterogeneous with areas consisting of aggregated particles and geopolymer matrix areas consisting of a more homogeneous microstructure. Morphological change due to milling resulted in a more homogeneous matrix with progressively smaller areas of precursor material. This change in surface area of the precursor material resulted in more dissolution and acceleration of setting rate (Xu & van Deventer 2000).

Curing temperature and time are important factors that influence the final compressive strength of the aluminosilicate inorganic polymers. van Jaarsveld *et al.* (2002) reported that initial curing at temperatures higher than room temperature and in excess of 2 hours improves compressive strength values of metakaolin based geopolymer systems. However, for extended curing times in excess of 24 hours in a sealed container there is a decrease of compressive strength which was attributed to the requirement of structural water within the material to reduce cracking and maintain structural integrity (Khalil & Merz 1994, van Jaarsveld 2002). Even in a sealed environment, water will be liberated and travel to the surface of the geopolymer via capillary action, leading to the reduction in structural water. It was

concluded that an optimal curing time was between 12 to 24 hours. Bakharev (2005) as well as Hardjito and Rangan (2005) reported that prior to curing a pre-curing period at room temperature is beneficial for strength development. Bakharev (2005) also states that fly ash geopolymer synthesised using NaOH activator had more stable strength properties than those formed using sodium silicate solution. Although this observation has merit, it cannot be assumed that NaOH is comparable with $NaSiO_3$ as the Si:Al ratio will be altered. However, this does draw attention to the importance of the pH of the activating solution for dissolution of the amorphous content. De Silva and Sagoe-Crenstil (2007) conducted an extended curing experiment with metakaolin based geopolymer at 40 °C for up to 7 months using low water content. It was found that the conversion from amorphous gel to a related zeolite can occur at a low temperature. This reinforces earlier statements that geopolymer gel is the precursor material to zeolite formation. A range of curing times has been cited in the literature and the best compressive strength quoted in the literature was cured for 24 hours (Palomo *et al.* 1998). Collins and Sanjayan (2001) state that curing samples in air resulted in lower compressive strength when compared with samples cured in sealed containers. This can be attributed to the loss of water from the system via evaporation, leading to incomplete geopolymerisation and formation of surface cracks. The loss of water by evaporation caused surface cracks (average size 0.01 mm) that occur within the first 3 days. The formation of the 0.01 mm cracks reached maximum density at 7 days. This was then followed by crack growth with widths expanding to 0.3 mm. Air exposed samples also had high water sorptivity, which is associated with the continuous microcracking and capillary network.

The effect of water upon the formation of geopolymer is not well understood. It is necessary to provide sufficient water to facilitate mixing and provide a mechanism for ionic transport however, the effect of excess water dilutes the alkaline solution or leaches the more soluble components and transports them away from the reaction zone (Barbosa *et al.* 2000). Dent Glasser and Kataoka (1981) conducted a dissolution experiment in which amorphous silica gel was dissolved in sodium hydroxide solution at different pH levels. As expected the outcome showed that the pH of the alkaline solution determines the amount of silica gel that can be dissolved. As the silica gel dissolves the pH of the solution decreases until it reached the point

where the dissolution of silica gel stops. This reinforces the understanding that pH of the alkaline solution is intimately tied to the amount of water required in the synthesis of geopolymer. By allowing enough water to ensure a high pH of the alkaline activator solution (to allow for the predetermined Si:Al:M ratio), maximum consumption of the amorphous aluminosilicate feedstock should be achieved. This amount should be enough to allow for complete wetting of the feedstock material, sufficient workability for placement and prevent efflorescence post production.

van Jaarsveld *et al.* (2002) states that the H_2O:SiO_2 molar ratio is critical in the synthesis of aluminosilicate inorganic polymers. Water has an active role in the dissolution and polycondensation of zeolite and polymeric precursor species. H_2O:M ratio is also important, as smaller alkali metal cations are more capable of properly ordering water molecules compared to the larger cations. Although water addition increases workability, too much will lead to a deterioration of compressive strength as ratio of water to polymer solids by mass increases and dilutes the alkaline solution (Hardjito *et al.* 2004).

The quality of the starting materials directly influences the quality of the geopolymer. The presence of impurities will either alter the microstructure and properties of the resultant polymer or act as an aggregate. For instance, when CaO is present in the starting material as lime it may strengthen the geopolymer by forming amorphous Ca-Al-Si gel (Xu & van Deventer 2002) and/or react rapidly, reducing setting time and possibly 'flash setting' the material (Nugteren *et al.* 2009). The presence of lime would promote a heterogeneous mix of two cementitious binders possibly reducing some of the beneficial properties of geopolymer. However the negative effects can be offset by lower setting times and/or ambient setting of the combined material.

Xu and van Deventer (2002) conducted a study of the geopolymerisation of multiple starting materials using a mixture of kaolinite, fly ash and albite. It was found that the fast reaction rate of fly ash and albite aided in the reaction rate of the kaolinite, which has a lower reactivity and thus allows for sufficient time to allow interaction with the gel phase. However, their highest result for compressive strength was 24.4 MPa which is low when compared to compressive strength values that can

be achieved by a single starting material geopolymers such as 86 MPa using metakaolin (Subaer 2004).

The introduction of aggregate has been found to decrease strength however the loss is dependent upon the amount of aggregate and the types introduced to the mixture. This was demonstrated when Lee and van Deventer (2004) created mortars and concrete, where the mortars had greater strength compared to the concrete. Subaer (2004) found that inclusion of fine aggregate in excess of 30 wt.% resulted in lower compressive strength.

Lee and van Deventer (2002a, 2002b, 2002c) investigated the effect of doping geopolymer mortar with various salts. The setting and rheological characteristics were compared with a control sample. Doping was conducted by dissolving or suspending the salt in water prior to addition to the fly ash and alkaline silicate solution mixture. Mg salts were determined to have very little effect on setting whilst Ca salts shortened setting time. The measurement of yield stress however showed that Mg salts increased early paste strength more than Ca salts. K salts were proposed for extending setting time, in which K_2HPO_4 demonstrated the largest change (Nugteren *et al.* 2009). The authors recommended the study of long-term stability of the cements due to salt doping.

Barbosa *et al.* (2000) measured the viscosity of geopolymer mixes to determine the polymerisation mechanism. Changes in viscosity during geopolymerisation were found to be similar to the relationship between melt viscosity and molecular weight of a polymer. At the early stage of reaction, the growing units act in a similar manner to a dilute solution in the unreacted mixture. As time progresses the polymer concentration increase and the units move closer together to overlap. This then initiates a rapid increase in the number of polymer linkages and average molecular weight. This can be compared to the ‘gel effect’ which occurs during radical polymerisation.

Goretta *et al.* (2004) undertook preliminary studies of the durability of class C fly ash based aluminosilicate inorganic polymers using a solid-particle erosion slinger-type apparatus. The aluminosilicate inorganic polymers utilised by the

Goretta group were activated by sodium silicate solution with average compressive strength of 35 MPa. Al_2O_3 abrasives of 390 μm were used at angles of 30, 60 and 90 degrees with velocities of 50, 70 and 100 m/s. Results of the abrasive testing indicated that the polymer behaved as a classically brittle material. Elastic-plastic indentation events led to the formation of brittle lateral cracks resulting from the loss of material. Erosion rates were proportional to the erodent velocity; however erosion at 30 degrees led to anomalously high erosion rates that were independent of velocity. This was believed to be due to material loss by propagation of both lateral and radial cracks and presence of microcracks and aggregates in the matrix. It was determined that for all velocities, the extent of chipping was controlled by microcracks in the matrix.

2.3 Conclusion

Current research into the field of geopolymers is occurring at a rapid rate with an emphasis on understanding the geopolymerisation process and the chemistry of the final material. However insufficient research has been conducted on the beneficiation of fly ash and how it can effect geopolymer production and properties. Beneficiation can be seen as a means of addressing current obstacles such as the amount of unreactive material left as filler material in geopolymer, consistency of mixes and full utilisation of all the reactive content in the feedstock. This thesis aims to address changes that occur to the geopolymer through the beneficiation of an Australian fly ash.

Chapter 3

Experimental Program

3.1 Introduction

This chapter provides a description of the analytical techniques utilised to characterise the chemical and microstructural properties of Collie fly ash as well as the chemical, microstructural and mechanical properties of geopolymer made from modified variants of Collie fly ash. The processing procedures utilised in the beneficiation of the fly ash as well as the production of the geopolymer are also included.

This chapter is subdivided into five sections: (1) Characterisation of Fly Ash, (2) Reactivity of Fly Ash, (3) Beneficiation of Fly Ash, (4) Geopolymer Production and (5) Physical Characterisation of Geopolymer.

3.2 Characterisation of Fly Ash

The fly ash from the Collie power station was retrieved from the electrostatic precipitator collection bags. The fly ash was not classified prior to bagging.

Due to the unknown nature of the fly ash, it was prudent to first determine its physical and chemical properties.

Mineralogical characterisation was conducted by a combination of x-ray and electron microscopy techniques. The analytical techniques utilised were: laser sizing, loss on ignition (LOI), scanning electron microscopy (SEM), surface area analysis (BET), x-ray fluorescence spectroscopy (XRF) and x-ray diffraction (XRD) (laboratory based and synchrotron radiation).

3.2.1 Sampling Procedure

Due to the difference in morphology and range of particle size of the fly ash, it was necessary to split the sample to ensure representative sub-samples were available for analysis.

A riffle splitter (Metal Craft) was utilised to ensure uniform and consistent sampling of fly ash from the bulk supply. The manual riffle splitter was used to sub-divide 20 kg of Collie fly ash into 1 kg allotments.

For the synthesis of geopolymers, fly ash powder was not split. Instead the containers holding the bulk fly ash were vigorously agitated by rolling, shaking and tumbling the buckets to ensure no size settling of the particles. The containers were then left for a couple of hours to allow for the finer airborne particles to settle prior to sampling.

3.2.2 Particle Size

Particle size analysis was used to determine the size range and mean size of the fly ash particles. The method utilised in this project was the laser diffraction method (Jillavenkatesa *et al.* 2001).

Particle size distribution was undertaken by the Commonwealth Scientific and Industrial Research Organisation, Minerals Division (CSIRO Minerals) (http://www.csiro.au/places/Waterford.html).

Fly ash was first de-agglomerated by suspending the fly ash in ethanol and placing it in an ultrasonic bath. The specimens were then introduced into a Malvern MasterSizer (MS2000) which has a measuring range of 0.02 µm to 2000 µm utilising the Mie Scattering measurement principle (Mie 1908).

3.2.3 Loss on Ignition

A standard test method for determining the carbon content and other combustible components of a sample is loss on ignition (LOI). This process involves heating the powdered sample until the organic volatiles (primarily carbon) are burnt off. The mass difference after this ignition process is then taken as the overall carbon content.

A typical x-ray fluorescence spectroscopy procedure was utilised for LOI. One gram of powder (dried overnight at 105 °C) was placed in a pre-ignited alumina crucible (15 cc) before placing it in a muffle furnace (SEM, Serial F544). The crucibles and specimens were heated to 1050 °C and left for 8 hours before being cooled down to room temperature and weighed.

The results were compared to the initial weight and the difference was taken as the amount of combustible material in the fly ash.

3.2.4 Surface Area

A standard method for determining the surface area of a solid is by measuring the physical adsorption of gas molecules on its surface. This is commonly known as BET gas adsorption analysis named after its founders Stephen Brunauer, Paul Emmett and Edward Teller (Brunauer *et al.* 1938, Atkins & De Paula 2006, Klobes *et al*. 2006). The BET adsorption isotherm is typically expressed as:

$$\frac{p}{v(p_0-p)} = \frac{1}{v_m c} + \frac{c-1}{v_m c}\frac{p}{p_0} \qquad (3.1)$$

where:

p = equilibrium pressure of adsorbate

p_0 = saturation pressure of adsorbate

v = total volume of adsorbed gas

v_m = monolayer adsorbed gas quantity

c = BET constant

When $\frac{p}{v(p_0-p)}$ is plotted against $\frac{p}{p_0}$ it should result in a straight line with the y-intercept (I) being $\frac{1}{v_m c}$ and the slope (S) being $\frac{c-1}{v_m c}$. This allows v_m and c to be determined:

$$v_m = \frac{1}{S+I} \qquad (3.2)$$

$$c = 1 + \frac{S}{I} \qquad (3.3)$$

Surface area (S_{BET}) can then be calculated using:

$$S_{BET} = \frac{v_m N s}{V a} \qquad (3.4)$$

where:

N = Avogadro's number

s = adsorption cross section of adsorbing species

V = molar volume of adsorbent gas

a = mass of adsorbent (g)

BET analysis was conducted at the Commonwealth Scientific and Industrial Research Organisation, Minerals Division (CSIRO Minerals) (http://www.csiro.au/places/Waterford.html).

Powders were prepared by degassing at 100 ºC and 100 mTorr for 3 hours prior to analysis. Samples were analysed following ASTM C 1069 in a Micromeritics Tristar 3000 using nitrogen as the adsorbate gas at a temperature of 77.3 K.

3.2.5 X-ray Fluorescence Spectroscopy

X-ray fluorescence spectroscopy (XRF) is a commonly utilised analytical technique for the determination of bulk elemental composition. When a sample is struck by high energy x-rays, emission of characteristic secondary (fluorescent) x-rays will occur (Brouwer 2003). When an atom is struck by radiation with a greater energy than the atom's ionisation potential an inner electron can be removed. Due to the instability of the atom after this occurrence, an electron from an outer shell drops into the empty position in the inner shell releasing a photon with energy equal to the energy difference between the two orbitals involved. This energy is characteristic of the atom enabling unique identification. Use of standards in conjunction with a measure of the intensity of the fluorescent emission allows a quantitative measure of each element in the sample.

XRF analysis was outsourced to Ultra Trace Geoanalytical Laboratories (http://www.ultratrace.com.au).

Powdered samples were crushed and prepared using a glass fusion technique to ensure high accuracy for major elements. The fusion beads were then analysed using a Panalytical MagiX Pro spectrometer, where concentration was derived from a comparison with known standards. Results were reported by Ultra Trace as elemental oxides with no uncertainty values. Uncertainty of the elemental values was taken as the standard deviation of repeated XRF analyses of either three or seven different samplings of Collie fly ash.

3.2.6 X-ray Diffraction

X-ray diffraction is based upon the interactions between x-ray radiation and sample electrons. When x-ray radiation of a specific wavelength and at a specific incident angle interact with a crystalline specimen, constructive interference of the scattered radiation can occur leading to intense peaks (Bragg peaks) (Cullity 1956). This constructive interference is expressed by Bragg's law:

$$n\lambda = 2d\sin\theta \qquad (3.5)$$

where:

n = integer determined by the reflection order

λ = x-ray wavelength

d = interplanar distance

θ = scattering angle.

By using a fixed wavelength the interplanar distances can be determined based upon the scattering angle of the diffracted x-rays. These values can then be compared to those recorded in powder diffraction databases for phase identification purposes.

3.2.6.1 Specimen Preparation

In order to obtain quality diffraction data that is representative of the sample, the powder specimen must be ground to less than 10 µm and packed so grains are randomly orientated.

Powdered specimens for qualitative XRD were prepared by reducing the particle size to less than 10 µm in a McCrone Micronising Mill with sintered alumina media. Two grams of powder were milled with 10 mL of ethanol to minimise sample change due to percussive effects. Samples being prepared for quantitative analysis were spiked with 10 wt.% internal standard material (fluorite or zincite). Milling time was set at 10 minutes.

Laboratory XRD sample holders were loaded by side packing using a thick glass slide to ensure compaction of the powder and to minimise preferred orientation effects. The top of the sample holders would then be screeded to ensure correct sample height and to minimise specimen displacement errors.

Australian Synchrotron Powder Diffraction Beamline powdered samples were packed into 0.5 mm diameter Glas Borokapillaren capillaries. A Dremel 400 series rotary tool (bristle brush attachment) was utilised to encourage dense packing of the powder before the capillaries were sealed by melting the glass. The capillaries

were then mounted at the Australian synchrotron on individual goniometers prior to placement on the multi-sample holder.

3.2.6.2 Laboratory Based XRD

During the course of the project, the initial x-ray diffractometer a Siemens D500, located at Curtin University was replaced by a new instrument, a Bruker D8 Advance.

The Siemens D500 diffraction data utilised for phase identification was collected from 10 ° to 90 ° 2θ with a Cu tube using a potential of 40 kV and tube current of 30 mA. Step size was 0.02 ° 2θ with a scan rate of 0.6 ° 2θ per minute. A graphite monochromator was used to obtain Cu-Kα radiation directed onto a NaI detector. Samples were rotated during data collection.

The Bruker D8 Advance diffraction data for phase identification was collected from 10 ° to 80 ° 2θ with a Cu tube using a potential of 40 kV and a tube current of 40 mA using Cu-Kα radiation. Step size was 0.02 ° 2θ with a scan time of 0.3 seconds per step. The diffraction data was collected with a LynxEye detector. A knife edge collimator was introduced to reduce air scatter and samples were rotated during data collection. A graphite monochromator was not used due to the incompatibility with the LynxEye detector however a Ni filter was used to eliminate k_β peaks. Quantitative data was collected from 10 º to 120 º 2θ with a 0.005 º step size and scan time of 0.3 seconds per step.

The LynxEye detector is comprised of 192 silicon strips enabling 4 ° 2θ to be collected simultaneously. The combination of this collection angle plus a large dynamic range (7×10^6) enables high count rates and short pattern collection times.

3.2.6.3 Synchrotron XRD

The Powder Diffraction Beamline (PDB) located at the Australian Synchrotron (Clayton, Australia) uses a high-accuracy, 3-circle powder goniometer

in conjunction with a Swiss Light Source (Paul Scherrer Institut) Microstrip detector (MYTHEN detector).

The MYTHEN detector is specifically designed for time resolved experiments; using a microstrip detector system comprised of a number of detector modules enabling rapid parallel detection of x-rays and a fast readout time (Schmitt *et al.* 2003). Thus the time required to record a full pattern is reduced from hours using a traditional single or double monochromator detector system to seconds. The trade off for this rapid collection rate is a reduction in resolution and signal to noise ratio.

The MYTHEN detector at the Australian Synchrotron PDB is comprised of 16 parallel detector modules. One module covers a range of approximately 4.8º 2θ with an approximate 2θ gap of 0.2º between adjacent modules. The configuration at the powder diffraction beamline has a single pixel covering approximately 0.00375º 2θ which resulted in a total collection angle of approximately 80º 2θ. Due to the 0.2º 2θ gap between adjacent modules, a second histogram for each sample was collected after moving the detector an arbitrary angle of 0.5º 2θ. The two histograms were summed before processing the diffraction data.

Powder diffraction patterns were then obtained over a range of 10 to 90 ° 2θ using an energy of 20 keV and a focused beam of 2 mm x 0.5 mm. The capillaries were also spun during data collection.

3.2.6.4 Phase Identification and Quantification

EVA 2 (Bruker) automated phase identification software was utilised to analyse Bruker D8 Advanced diffraction patterns as well as diffraction patterns obtained from the Australian Synchrotron. Background was removed using the 'Enhanced' method and Kα2 peaks were stripped. Quality marks of 'Star', 'Computed from structure parameters' and 'Indexed' and the subfiles of 'Inorganic' and 'Minerals' were selected.

EVA 2 search/match provided the following ICSD results for the D8 Advanced data: Hematite (#66756), Maghemite C (#87119), Magnetite (#30860), Mullite (#28544), Quartz (#41412) and Zincite [internal standard] (#34477) (Appendix 1).

EVA 2 search/match provided the following ICSD results for the Australian Synchrotron data: Corundum (#77810), Fluorite [internal standard] (#41413), Hematite (#66756), Maghemite C (#87119), Magnetite (#30860), Mullite (#28544), Quartz (#41412) and Rutile (#109469) (Appendix 1).

The internal standard was changed to fluorite for the PDB samples due to the slightly adhesive nature of zincite which would cause the sample to be trapped on the walls of the capillary and to avoid peak overlap with any phases that could be detected by synchrotron radiation.

TOPAS 4.2 (Bruker) was utilised for Rietveld refinement with D8 Advance and PDB data. Instrument parameters for the D8 Advance and the PDB used in TOPAS are found in Appendix 2.

Laboratory based data utilised the 'CuKa5' emission profile found in the TOPAS folder. PDB data required an emission profile to be developed from a NIST standard (LaB_6) (See Appendix 2).

The ICSD data was transferred to TOPAS 4.2 in the form of CIF files and appropriately modified to ensure compatibility with the TOPAS 4.2 software as according to the software addendum (Appendix 2) prior to saving as STR files. The relevant instrument parameters and x-ray source parameters were transferred to TOPAS 4.2. Depending on the amorphous content, up to two Split Pseudo Voigt (SPV) functions were utilised to model the amorphous background. During the initial modelling the quartz peaks were fitted poorly using only one quartz phase. This was rectified by the inclusion of an additional quartz phase using the same ICSD input to represent secondary quartz that was formed during the coal combustion process (Drzal *et al.* 1983). The parameters refined during Rietveld modelling are presented in Table 3.1.

Table 3.1: Parameters refined for fly ash with 10 wt.% internal standard.

	Global	Standard	Hematite	Maghemite	Mullite	Quartz (Primary)	Quartz (Secondary)
Background	Y	-	-	-	-	-	-
1/X bkg	Y	-	-	-	-	-	-
Sample Displacement	Y	-	-	-	-	-	-
Scale	-	Y	Y	Y	Y	Y	Y
Lattice Parameters (a, b, c)	-	Y	Y	Y	Y	Y	Y
Crystallite Size (Lorentzian)	-	Y	Y	Y	Y	Y	Y
Site Thermals	-	Y	N	N	N	Y	Y

3.2.7 Scanning Electron Microscopy

Scanning electron microscopy is a common imaging technique used to investigate the microstructure and morphology of mineral particles. Areas of different atomic weight can be highlighted in the images and energy dispersive x-ray spectroscopy can be used to determine elemental composition.

3.2.7.1 Sample Preparation

Samples for scanning electron microscopy (SEM) were prepared by one of two methods.

The first method involved using a pin type SEM mount (12 mm diameter) (ProSciTech) with double sided carbon tape on its surface as a sample mount. The sample was placed on the carbon tape. A Dynavac Sputter Coater (Model SC150) was used to gold coat the sample to make the surface electrically conductive. This approach was used when the morphology of fracture surfaces needed to be investigated.

The second method involved the sample being embedded in a resin followed by diamond polishing of the surface to a 1 µm finish. Struers UnoForm moulds (25 mm diameter) with general purpose low viscosity epoxy resin (Fibreglass & Resin Sales Pty Ltd FR-251 were utilised for sample preparation.

Powdered samples were carefully mixed with the epoxy resin to ensure adequate dispersion. The epoxy hardener would then be added (2 parts epoxy resin to 1 part epoxy hardener) and stirred vigorously to ensure full reaction. The mixture was then poured into the UnoForm mould and air bubbles in the mixture removed using a vacuum desiccator. The mixture would be allowed to harden overnight prior to demoulding and surface polishing.

Samples of geopolymer were placed flat at the base of the UnoForm mould and then covered by epoxy resin. Air bubbles were removed using a vacuum desiccator prior to hardening overnight and subsequent surface polishing.

A Struers Pedemat and Planopol-V were used to grind and polish the resin embedded sample surface, respectively. Grinding was done with a 40 µm pad using water as a lubricant followed by diamond polishing down to 1 µm using Struers diamond paste and Struers DP-Blue lubricant.

Samples prepared for solely imaging purposes were coated with gold using a Dynavac Sputter Coater (Model SC150). When both imaging and energy-dispersive x-ray spectroscopy (EDS) was to be conducted, samples were coated with carbon using a Selbys Evaporative Coater or a 2 nm thick coat of platinum/palladium using a Cressington sputter coater (208HR) with accompanying Cressington thickness monitor (mtm20).

3.2.7.2 Image Collection

The scanning electron microscopes utilised for image collection were a Philips XL30, Zeiss EVO 40XVP and Zeiss Neon 40EsB. The XL30 and EVO 40XVP instruments were equipped with a tungsten filament with a maximum EHT

voltage of 30 kV. The Zeiss Neon 40EsB was equipped with a field emission gun with a maximum EHT voltage of 30 kV.

Images were generally taken at an EHT between 10 and 20 kV with spot size selected to optimise resolution. Philips XL30 images were processed by the Philips program XLStretch to ensure that the correct sample dimensions were retrieved.

3.2.7.3 Energy Dispersive X-ray Spectroscopy

Energy dispersive x-ray spectra (EDS) were collected using a Oxford Instruments INCA X-act mounted onto the Zeiss Neon 40EsB. EHT voltage utilised for analysis was 10 kV.

3.2.8 Quantitative Evaluation of Minerals by Scanning Electron Microscope

Additional analysis of the mineralogy of samples was conducted using a QEMSCAN (Intellection) instrument located at CSIRO Minerals Waterford. The QEMSCAN instrument is based on the QEM*SEM, Quantitative Evaluation of Minerals by Scanning Electron Microscope. The QEMSCAN is a Carl Zeiss SEM which has been adapted, with additional software and hardware (4 light-element silicon drift energy dispersive x-ray detectors), to conduct automatic x-ray analysis and provide phase identification of grains. The system has seen wide spread use in the mining industry, to confront mineralogical problems in recoveries and process plant performance (Gottlieb *et al.* 2000).

Samples were prepared by mixing fly ash in a 1:1 ratio with a high purity graphite spacer. The mixture was then resin embedded and polished to a 1 μm finish. Resin embedding and polishing was done by staff at CSIRO Minerals.

QEMSCAN samples were analysed using an EHT of 25 kV, an emission current of 11 μA, specimen current of 5 nA and a working distance of 21 mm.

The elemental ratios used for the determination of phases are provided in Appendix 3.

3.3 Reactivity of Fly Ash

Reactivity of fly ash is dependent upon the type of alkaline activator utilised the pH of the solution and the composition and size distribution of the fly ash. The approach adopted was to place a small amount of fly ash in concentrated sodium hydroxide solution and measure weight change with time. The results obtained from these experiments were combined with XRF, SEM and QEMSCAN to observe changes to morphology and phases during the dissolution process.

3.3.1 Sodium Hydroxide Dissolution

Dissolution involved submerging a small amount of fly ash in a relatively large volume of sodium hydroxide solution. The mixture was agitated by either a magnetic stirring rod or by manually shaking prior to placement in a hot shaker bath. Periodically the residues were removed from the solution, washed, dried and weighed. At each stage a portion of the dried powder was set aside for later analysis using SEM, XRD and QXRD.

Three dissolution experiments were conducted. The first dissolution experiment was treated as a pilot experiment and procedure refined for the second and third dissolution experiments.

3.3.1.1 First Dissolution Experiment

The first dissolution experiment consisted of 5 g of fly ash being submerged in 200 mL of 10 M sodium hydroxide solution (AR grade sodium hydroxide pellets & Type II deionised water) whilst being agitated by a magnetic stirring rod. Dissolution was conducted for various time periods and at two different temperatures (Table 3.2).

Table 3.2: Parameters for first dissolution experiment of unmodified Collie fly ash.

Temperature (ºC)	Time Allocations (min)
22	5, 20, 40, 60, 240, 720, 1140
75	10, 20, 30, 40, 50, 60, 120, 240, 1440

For each dissolution time and temperature the solid residues was removed from the solution by vacuum filtration using 0.2 µm filter paper (PALL Supor®-200 Membrane Filter). The filtered residues were then dried (105 °C to constant weight), weighed and compared against starting mass. To ensure accurate weighing of the residues, the filter papers were weighed prior and post usage. To take into account the mass of the dried NaOH solution on the filter papers, three filter papers were submerged in clean NaOH solution, dried and weighed with the average weight of the dried NaOH subtracted from the residue weight. The residues were also analysed by XRD and SEM/EDS.

3.3.1.2 Second Dissolution Experiment

The second dissolution experiment consisted of 5 g of fly ash being submerged in 200 mL of 14 M sodium hydroxide solution (Tech grade sodium hydroxide pearls & Type II deionised water) whilst being agitated by a magnetic stirring rod.

The changes in conditions between the first and second dissolution experiment were:

- Increase in NaOH concentration from 10 to 14 M.
- The temperature was fixed at 75 °C.
- The original fly ash and sieved fly ash (< 45 µm) were put through the dissolution process.
- A NaOH replacement step was introduced as a means of minimising formation of geopolymer and zeolites.

The first dissolution experiment provided conditions conducive to the formation of zeolite (abundance of NaOH solution and elevated temperature). In fact it was expected that geopolymer gel would eventually precipitate out of solution and then crystallise into zeolites. It was noticed in XRD patterns from the first dissolution experiment that geopolymer and zeolite formation occurred as early as 30 minutes at 10 M. Therefore to counter the formation of geopolymer and zeolite, the replacement of NaOH solution at 15 minute intervals was implemented.

For the second dissolution experiment the solid residues were separated from the solution by vacuum filtration using 0.2 µm filter paper (PALL Supor®-200 Membrane Filter). The solid residues were then washed using deionised water and placed back into their respective conical flasks for further dissolution using fresh NaOH solution. This process was conducted at 15 minute intervals until 1 hour total dissolution time has passed. In addition to the careful weighing procedure adopted for dissolution experiment 1 the values of the filter papers utilised in NaOH replacement were included in the final weight calculations as there is expected to be a slight sample loss from each NaOH replacement step.

Dissolution was conducted for various time periods at 75 °C (Table 3.3).

Table 3.3: Parameters for the second dissolution experiment.

Sample	Time Allocations (min)
Unmodified Fly Ash	10, 20, 30, 40, 50, 60, 70, 80, 90, 120, 240, 1440
< 45 µm Fly Ash	10, 20, 30, 40, 50, 60, 70, 80, 90, 120, 240, 1440

The residues from the experiment were prepared and analysed using the same procedure adopted in the first dissolution experiment.

3.3.1.3 Third Dissolution Experiment

The third dissolution experiment consisted of 2 g of fly ash being submerged in 80 mL of 14 M sodium hydroxide solution (Sigma Aldrich AR grade sodium

hydroxide pellets) in a Nalgene Oak Ridge Style centrifuge tube and agitated in a shaker hot bath (Julabo SW22).

The changes in steps between the second and third dissolution experiment were:

- Use of hot shaker bath instead of magnetic agitation.
- Use of a centrifuge to extract fine solids from the vacuum filtered NaOH solution.
- Inclusion of a sieved and milled fly ash powder with the original fly ash. The new fly ash consisted of sieved fly ash that was attrition milled for 30 minutes with a 25:1 ball to powder ratio using 5 mm diameter yttria stabilised zirconia milling media.

Magnetic agitation has the disadvantage that the magnetic stirring rod had to be placed in the solution to ensure rigorous mixing. At the end of each step the stirring rod had to be cleaned to ensure all undissolved sample is weighed. Unfortunately to fully remove all of the iron oxide attracted to the magnetic stirring rod proved to be very difficult leading to incorrect quantification of the iron oxide content. By using a hot shaker bath to agitate the sample in solution there will be a slight reduction in the energy introduced into the system from agitation however there will be no loss of iron oxide particles and temperature control was improved. To ensure that the fly ash particles remain in suspension, the centrifuge tubes were manually shaken prior to placement in the hot shaker bath and again at 15 minute intervals.

NaOH replacement was conducted at 15 minute intervals using the same process as described in Section 3.3.1.2, however the filtered solutions were centrifuged after collection to separate fine particulates for analysis with SEM and XRD. NaOH replacement was continued up to the 1.5 hours.

Dissolution was conducted for various time periods at 75 °C (Table 3.4).

Table 3.4: Parameters for the third dissolution experiment.

Sample	Time Allocations (min)
Unmodified Fly Ash	15, 30, 45, 60, 90,
< 45 µm Milled Fly Ash	15, 30, 45, 60, 90

The residues from the experiment were prepared and analysed using the same procedure conducted in the first and second dissolution experiment. The very fine solids found in the solution were separated using a centrifuge (Kokusan H-103N Series). The separated fine solids were washed with water, dried (105 °C to constant weight) and analysed using SEM and XRD.

3.4 Beneficiation of Fly Ash

The heterogeneous nature of fly ash can have a negative impact on the geopolymerisation process. The abundance of secondary phases provides a barrier and/or absorbs the liquid alkaline activator preventing it from effectively interacting with the amorphous aluminosilicate content of the fly ash.

Removal of these non-reactive secondary phases (carbon, quartz, mullite and iron oxides) by sieving should enable the alkali to be more effective in dissolving the reactive amorphous aluminosilicate material, leading to a higher degree of geopolymerisation. Carbon particles provide an additional disadvantage due to the ability to absorb liquids thereby reducing the overall concentration of activating solution. If the surface area of the sieved fly ash is increased by grinding, a further increase in dissolution can be expected, leading to even further and more rapid geopolymerisation.

3.4.1 Size Fraction

Particle size was controlled using two methods: sieving and milling. It was determined by SEM imaging that a large fraction of secondary phases, primarily

carbon and quartz, could be removed with sieving. Milling was also identified as a means of increasing the reactivity of fly ash during the geopolymerisation process.

3.4.1.1 Sieving

Two Endecott sieves (75 µm and 45 µm) were used to separate the fly ash into > 45 µm, < 75 µm ≥ 45 µm and < 45 µm fractions. Initially a mechanical sieve shaker was employed to conduct 1 hour sieve shakes. Due to the slow throughput of the mechanical sieve shaker (DuraLab), manual sieving using a brush was utilised to separate the particle size fractions. To ensure that the brushes did not add contaminants to the powder; individual brushes were bought, thoroughly cleaned and reserved for only one section of the sieving process.

3.4.1.2 Milling

Both ball milling and attrition milling were trialled. For ball milling a steel canister (custom made) was used with steel balls (12.5 mm diameter) in air. For attrition milling a Szegvari Attritor System was utilised with a Teflon canister and yttria stabilised zirconia milling media (5 mm diameter).

Ball milling was conducted using a variety of ball to powder ratios and times until an optimal regime was determined. Due to the hardness of the quartz in the fly ash, contamination of the milled fly ash occurred with steel from the canister and milling media.

Attrition milling was used with a ball to powder ratio of 25:1 for 30 minutes. Ethanol was utilised as the liquid medium and a water jacket was used to maintain a constant temperature.

3.4.2 Magnetic Separation

A wet magnetic separation method was adopted after trialling both dry and wet magnetic separation methods.

The wet magnetic separation consisted of suspending the fly ash powder in a large volume of Milli-Q water. This mixture was then agitated prior to having the magnetic content removed by the use of a magnetic paddle. Both magnetic and non-magnetic content after separation were dried overnight at 105 ºC prior to analysis using SEM and XRD.

The magnetic paddle was constructed using an array of neodymium rare earth magnets (10 mm x 2 mm) encased in thin plastic (Figure 3.1A). A teflon sleeve was made to cover the paddle to ensure ease of collection (Figure 3.1B and 3.1C).

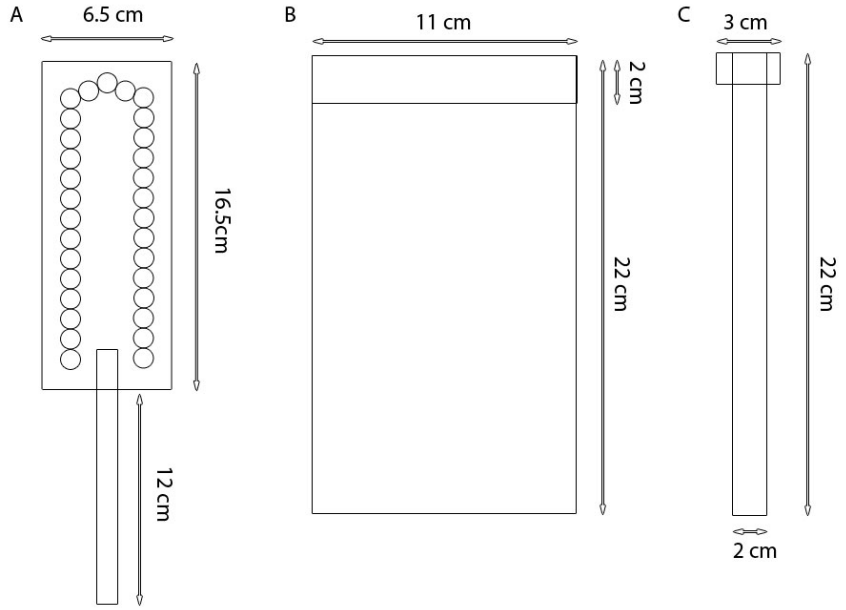

Figure 3.1: Diagram of magnetic paddle and teflon sleeve. The magnetic paddle (A) has an array of neodymium rare earth magnets (circles) placed between two thin plastic sheets. (B) and (C) show the front and side view of the thin teflon sleeve. The ridge is to ensure that the slurry does not come into contact with the paddle.

3.4.3 Carbon Separation

Two methods were used to remove carbon from the fly ash, flotation and carbon burn off.

Flotation involved taking a 250 ml beaker filled with ethanol and sprinkling a known amount of fly ash onto the surface of the ethanol. The heavier particles would

be allowed to sink to the bottom whilst the material floating on the surface of the ethanol was removed via vacuum suction, dried and weighed. Analysis of the material was conducted by SEM.

Carbon burn off was conducted using a muffle furnace (SEM, Serial F544). The fly ash was dried for 8 hours at 105 C° and weighed prior to placing in the muffle furnace at a temperature of 1050 ℃ for a period of 8 hours. Afterwards, the fly ash was removed from the muffle furnace and left to cool to a temperature between 20 ℃ and 25 °C prior to weighing. Analysis of the material was conducted using SEM and XRD.

3.5 Geopolymer Production

The production of geopolymer is still not a routine process due to lack of consistency and repeatability resulting from heterogeneity of the fly ash feedstock, the inability to accurately predict how much will react and the role of the dispersed secondary phases throughout the matrix.

Currently, it is believed that most researchers assume that the majority of the amorphous aluminosilicate material reacts with the alkaline activating solution. However, researchers such as Fernandez-Jimenez *et al.* (2005) showed how morphology of particles can hinder the geopolymerisation process by denying access to further amorphous aluminosilicate materials by the alkaline activating solution. With this information it can be surmised that the calculated Si:Al:M (where M is the alkaline cation) that researchers use to design mixes will be incorrect. This will then lead to a misbegotten belief that these ‘correct’ mixes are a proper representation of the fly ash geopolymer they have produced.

3.5.1 Production Method

Geopolymer were produced using a combination of fly ash and solutions of sodium silicate and sodium hydroxide.

Fly ash feedstock consisted of as provided fly ash (Collie fly ash, late 2005) and the beneficiated variants.

The sodium silicate solution was D-Grade Sodium Silicate (PQ-D) from PQ Corporation. The component ratio of PQ-D was: Na_2O 14.7 %, SiO_2 29.4 % and H_2O 55.9 % by weight.

The 14 M NaOH solution was synthesised using reagent grade (≥ 98 %) NaOH pellets (Sigma Aldrich) and Milli-Q water.

The masses of the three key components of geopolymer were determined prior to starting using a predetermined Si:Al:Na ratio. Prior to weighing the fly ash feedstock was dried overnight at 105 °C to remove moisture. The PQ-D solution and sodium hydroxide solution were mixed together and manually agitated in a Nalgene bottle. The feedstock would be deposited into an ARE-250 (Thinky) mixing capsule with the alkaline activating solution poured on top of the powder. The mixing regime of the ARE-250 consisted of mixing at 1300 rpm for 5 minutes followed by de-aeration at 2100 rpm for 10 seconds. Following the mixing the geopolymer pastes were poured into polyethylene vials (20 mm diameter by 40 mm height) for compressive strength testing/XRD/SEM analysis. For dilatometry, geopolymer paste was placed in polypropylene syringes with an inner diameter of approximately 4.3 mm. The geopolymer paste was agitated by tapping the side of the vials 20 times using a metal spatula before being capped and placed in a drying oven to cure at 70 °C for 24 hours whilst the syringes were placed straight into the drying oven. After curing samples were cut out of their mould and left at ambient temperature for a 7 day period according to ASTM C 39 prior to analysis.

3.6 Physical Characterisation of Geopolymer

Solid geopolymer samples were measured for density, water absorption, voids, compressive strength, hardness and thermal expansion.

3.6.1 Density, Absorption and Voids

ASTM C 20 was adopted for geopolymer paste samples. The ASTM was modified by the use of small dimension test samples.

Dry weight (D) was measured after heating the sample to 105 ºC. Suspended weight (S) was measured after the sample was immersed in water, boiled for a period of 2 hours and then cooled to room temperature. Saturated weight (W) was measured after the immersed samples were removed from water and lightly blotted dry to remove water droplets on the surface. The measured values were then inserted into the following equations:

$$V = W - S \quad (3.6)$$

$$P = \frac{W-D}{V} \times 100 \quad (3.7)$$

$$A = \frac{W-D}{D} \times 100 \quad (3.8)$$

$$B = \frac{D}{V} \quad (3.9)$$

where:

V = Volume (cm^3)
P = Apparent porosity (%)
A = Water absorption (%)
B = Bulk density (g/cm^3)

3.6.2 Compressive Strength

Compressive strength was conducted using a Lloyds EZ-50 set up in compressive mode and utilising a 50 kN load cell. ASTM C 39 was utilised for the compressive strength test regime. The selected test age was 7 days (with associated tolerance level of ± 6 hours). Samples ends were ground to ensure that they were parallel. The ASTM C 39 methodology was slightly altered to suit the Lloyds EZ-50 machine by including an initial rate of loading of 5 mm/min to the point of 2000 N. This was to smooth the initial stress/strain curve. After 2000 N was reached, the

ASTM C 39 rate of loading was applied at 0.25 MPa/sec (7422 N/min) until the sample failed.

3.6.3 Thermal Expansion

A connecting rod dilatometer (Adamel Lhomargy DI-24) was utilised in the analysis of thermal expansion.

ASTM E 831 was utilised for the thermal expansion test regime. The cylindrical sample dimensions were approximately 4 mm diameter with a length of approximately 10 mm. A preload of 100 mN was applied to ensure that the sensing probe was in contact with the specimen. The heating rate was set to a constant 5 °C/min from room temperature to 900 °C with a cooling rate of 5 °C/min until room temperature. As recommended by the ASTM E 831, samples were made and tested in triplicate.

3.6.4 Rockwell Hardness Test

An Avery Rockwell hardness tester (Figure 3.2) was utilised with the H Rockwell hardness scale.

The Avery was equipped with a flat anvil, a 1/8 inch steel ball indenter and a 60 kgf additional load weights. The sample was placed on a flat anvil and the elevating screw was raised until the sample contacted with the indenter. After initial sample contact with the indenter, the Avery indicator pointers will begin to rotate as the preliminary load is applied via the raising of the elevating screw. Once the indicator pointers are in the positions shown in Figure 3.3 then the raising of the elevating screw will be stopped.

At this point the preload has been set and the additional load can be applied. Once the large pointer on the indicator has come to a stop then the additional load will be removed. Once the large pointer on the indicator has come to rest once again, the reading will be taken.

Figure 3.2: Avery Rockwell hardness tester.

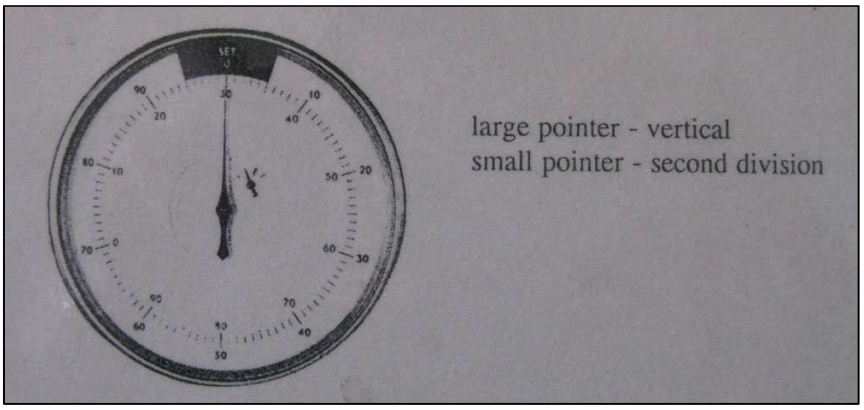

Figure 3.3: Avery Rockwell hardness tester indicator.

Chapter 4

Characterisation of Fly Ash

Note: Chapter 4 is based upon the paper: Chen-Tan N.W., van Riessen A., Ly C.V. & Southam D.C. 2009, 'Determining the reactivity of a fly ash for production of geopolymer', *Journal of the American Ceramic Society*, Vol. 92, pp. 881 – 887

4.1 Introduction

A comprehensive understanding of fly ash is required to determine what variables can be altered in the beneficiation process. Armed with this knowledge it can be predetermined what the expected impact of the beneficiation will have upon the resultant geopolymer produced from the modified feedstock.

Premier Coal (2004) states that "Collie coal does not conform to conventional classifications. It has the physical appearance of black coal but shares chemical properties with high volatile bituminous coals, sub bituminous coals and lignite". Thomas (2005) however classified the Collie coal as a sub-bituminous (black lignite) grade coal. Collie coal contains higher moisture content compared with those extracted from the other states of Australia. It also has a high porosity and larger surface area leading to faster burning.

Only limited information was provided by Fly Ash Australia, suppliers of the fly ash. During the period of collection (2005), Collie power station did not have a classifier as part of their processing line. The fly ash was known to have a high alumina:silicon:iron concentration, thereby aligning it to a Class F fly ash (ASTM C 618). Collie fly ash is also known to have particle size finer than those produced by Eastern States power stations, believed to be due to the high moisture content of the initial coal (Thomas 2005). During processing the water is unable to be compressed during milling thereby creating large particles with 30 % water voids. Upon

introduction to the boiler the water is promptly volatilised causing the particles to break into extremely fine size which is reflected in the size distribution of the resulting fly ash pre-classification (Thomas 2005).

Hardjito and Rangan (2005) utilised Collie fly ash in a detailed study of the synthesis of geopolymer concrete with quartz aggregate of varying sizes. The limitation of the study conducted was that it did not demonstrate an understanding of how the Collie fly ash was reactive and what effect each component of the ash has upon the characteristics of the geopolymer product. The characterisation that Hardjito and Rangan (2005) conducted was limited to the measurement of particle size and bulk elemental analysis provided by XRF. This study also assumed that all the reactive fly ash content had been converted during geopolymerisation.

The two most important fly ash properties required for manufacture of geopolymer are the amount of reactive amorphous aluminosilicate material and the reactivity of this material during production. This information enables the amount and concentration of the alkaline activator required for maximum dissolution of the amorphous aluminosilicate material and formation of geopolymer.

This chapter will describe in detail the characterisation of Collie fly ash and how this information is used to predict the properties of the geopolymer.

4.2 Basic Characterisation

This section presents the general characterisation of Collie fly ash prior to introducing more detailed compositional and crystallographic characterisation.

Collie fly ash as provided in December 2005 has an earthy brown colour with traces of grey and black (Figure 4.1). Preliminary visual identification was conducted using a stereo microscope. Black irregular shaped or rough particles were identified to be carbon particles, black spheres with a shiny lustre were identified to be iron rich glassy particles while white/grey irregularly shaped particles were identified as quartz particles.

Figure 4.1: Collie fly ash.

Figure 4.1 shows the fly ash to be agglomerated fine particles which can be explained by a combination of electrostatic and van der Waals forces (Debrincat *et al*. 2007). When the dry fly ash particles are handled, electrostatic forces initially bring the powder together for adhesion prior to van der Waals forces maintaining the adhesion. This causes fine particles to clump together making it difficult to manufacture geopolymer unless vigorous mixing regimes are utilised. If high shear mixing is not utilised, the probability of a quantity of fly ash not being exposed to the alkaline activating solution is high due to the outside particles of a 'clump' shielding the inner particles. This problem is exacerbated if the fly ash is allowed to get wet and the agglomerates form a paste.

The water content of Collie fly ash stored at ambient temperature was determined by weighing the powder before and after heating at 105 °C for 8 hours. The water content was found to be 0.73 ± 0.02 wt.%. With such low water content, this value can be ignored during the planning of geopolymer ratio mixes.

Particle sizing of Collie fly ash conducted with a Malvern MasterSizer (MS2000) showed that just over 80 % of particles are less than 35 µm in diameter (Figure 4.2).

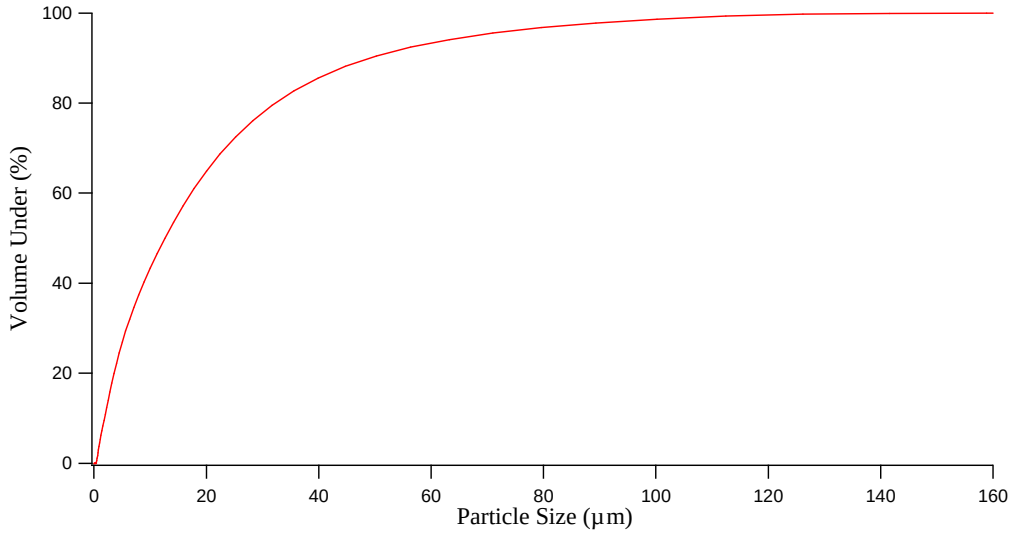

Figure 4.2: Particle size of Collie fly ash.

The carbon content of Collie fly ash (dried overnight at 105 °C to ensure no water content) was determined to be 2.06 ± 0.01 wt.%. High carbon content in fly ash causes a loss of compressive strength (Shi *et al.* 2006) as carbon has a high propensity to adsorb water and additives therefore disturbing the ratio required for hydrothermal polycondensation. Free carbon in geopolymer can lead to black streaks on the surface as the carbon tends to migrate to the surface during curing.

The morphology of Collie fly ash was determined using scanning electron microscopy (SEM) (Figure 4.3). The most common particles are spheres of less than 30 µm in diameter which form the main reactive part of the fly ash. The mineralogy of these spherical particles is discussed in a later section. A number of irregular shaped particles were present as either carbon rods/balls (char), quartz, fused clay or agglomeration of assorted previously mentioned particles.

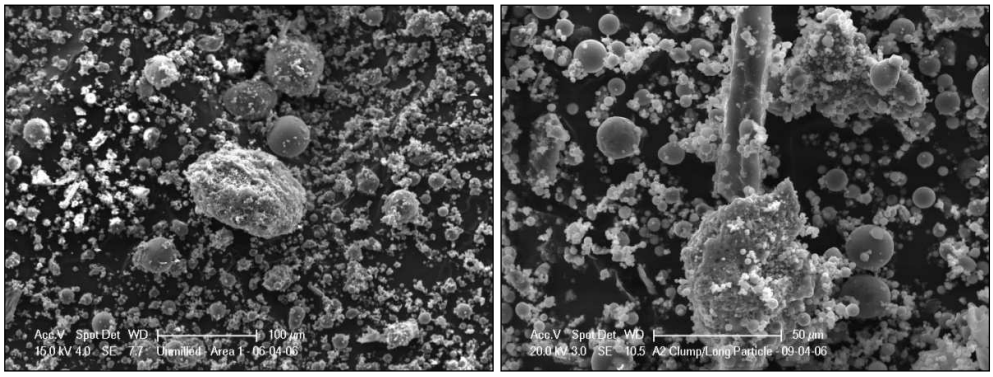

Figure 4.3: Secondary electron images of Collie fly ash at different magnifications (100 µm scale bar on the left image and 50 µm scale bar on the right image). (Philips XL30)

Bulk elemental composition of Collie fly ash was determined using x-ray fluorescence spectroscopy (XRF). The sum of Al_2O_3, Fe_2O_3 and SiO_2 is 90.38 wt.% which is greater than the 70 wt.% required to confirm it as a Class F fly ash (ASTM C 618). It should be noted that the molar Si:Al ratio of the bulk fly ash is 1.88.

Table 4.1: Elemental oxide composition (XRF) of Collie fly ash obtained from the average of 7 analyses. Uncertainties represent 1 standard deviation with rounding to 2 decimal places.

Elemental Oxide	Composition (wt.%)
SiO_2	51.46 ± 0.23
Al_2O_3	23.59 ± 0.21
CaO	1.75 ± 0.01
Fe_2O_3	15.33 ± 0.08
K_2O	0.84 ± 0.01
MgO	1.15 ± 0.01
Na_2O	0.36 ± 0.01
P_2O_5	1.31 ± 0.01
SO_3	0.27 ± 0.01
TiO_2	1.31 ± 0.01
MnO	0.13 ± 0.00

When compared to the currently available product data sheet for classified Collie fly ash (Appendix 4), unclassified 2005 Collie fly ash has comparable fineness (volume under 45 µm) of 88 % (vs 86 %), with a higher LOI value of 2.0 wt.% (vs 0.5 wt.%) and with similar bulk elements with the exception of 2 wt.% more Fe_2O_3 and 3 wt.% less Al_2O_3.

4.3 Mineralogy and Amorphous Content

XRD and XRF were used to determine the mineralogical and elemental composition of fly ash, including the amorphous component and its Si:Al ratio. This information can then be utilised to determine the amount of alkaline silicate solution required for a specific Al:Si:M (where M is the alkaline cation) ratio.

The crystalline content of Collie fly ash was found to be hematite, magnetite, mullite, maghemite C and quartz (Figure 4.4). As no crystalline carbon was identified in the XRD pattern, it is concluded that carbon found with Collie fly ash is amorphous.

The amount of each crystalline phase in Collie fly ash was determined using quantitative XRD (Table 4.2) and uncertainties were determined to be the standard deviation of results from 3 samples. Multiple samples were analysed to ensure a reasonable representation of the composition of the heterogeneous bulk sample.

Due to the heterogeneity of Collie fly ash, the uncertainty is relatively large and much greater than uncertainties based on Rietveld refinement alone. The homogeneity sets the limit of reproducibility of geopolymer production.

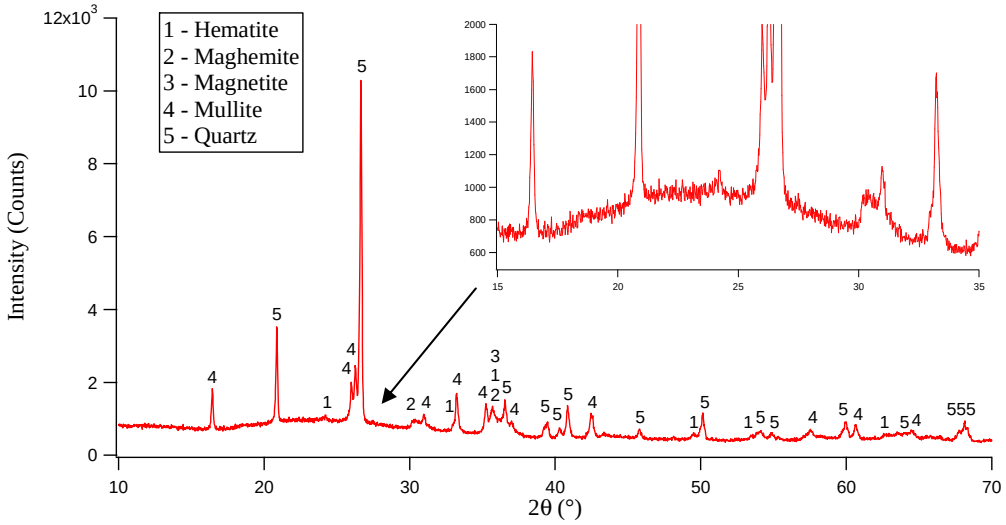

Figure 4.4: XRD pattern of Collie fly ash with peak identification overlaid. The insert shows a portion of the pattern with a vertical scale changed to emphasize the amorphous hump.(Bruker D8 Advance)

Table 4.2: Phase abundance of Collie fly ash obtained by Rietveld refinements with XRD data from 3 samples using TOPAS (Bruker). The uncertainty represents one standard deviation.

Phase	Composition (wt.%)
Amorphous	54.58 ± 1.03
Hematite	1.64 ± 0.03
Maghemite C	3.45 ± 0.10
Magnetite	2.33 ± 0.10
Mullite	16.2 ± 0.15
Quartz	21.81 ± 0.75

The total amorphous component as determined by quantitative XRD is 54.58 ± 1.03 wt.%. By combining XRF and XRD the amorphous Al:Si:O:Fe component is calculated to be 45.1 ± 1.2 wt.% which is 9.5 wt.% less. It is apparent that the quantitative XRD did not include phases containing the following elements C, Ca, K, Mg, Na, P, S, Mn, Ti and trace elements. The majority of these elements are likely to be in the form of minor crystalline phases which are below the detection limit of the laboratory based XRD and thus contribute to the background of the XRD pattern. The elements of Ca, K, Mg, Na, P, S, Mn, Ti and trace elements calculated from XRF values amount to 9.47 wt.% which subtracted from the XRD calculated value leaves a balance of 45.1 ± 1.0 wt.% amorphous material. This is in agreement with the estimated value of 45.1 ± 1.2 wt.% for Al:Si:O:Fe.

The amount of reactive Al and Si can be calculated from the two results by using the overall chemical information provided by XRF (see Section 4.2) and subtracting the Al and Si found within the crystalline phases determined by XRD. The Al and Si concentrations are presented in Table 4.3.

Table 4.3: Al, Si and Fe concentration from overall sample, crystalline phases and amorphous content.

Element	Overall (wt.%)	Crystalline (wt.%)	Amorphous (wt.%)
Al	12.48 ± 0.22	6.38 ± 0.12	6.11 ± 0.12
Si	24.05 ± 0.21	12.13 ± 0.73	11.92 ± 0.73
Fe	10.72 ± 0.05	5.24 ± 0.16	5.48 ± 0.16
Si:Al (mass)	1.93 ± 0.22	1.90 ± 0.43	1.95 ± 0.43
Si:Al (Molar)	1.85 ± 0.22	1.83 ± 0.43	1.88 ± 0.43

Analysis of the XRD data revealed that the detectable crystalline content of the fly ash consisted of hematite (Fe_2O_3), maghemite C ($Fe_{21.16}O_{31.92}$), magnetite (Fe_3O_4), mullite ($Al_{4.644}$ $Si_{1.357}O_{9.68}$) and quartz (SiO_2). Rietveld refinement with XRD data provided phase abundance of the crystalline phases as well as the weight percent amorphous fraction. Of particular note is that the Si:Al molar ratio of 1.83 ± 0.43 for the amorphous component is the same as that of the bulk sample (Si:Al

molar ratio of 1.85 ± 0.22) within levels of uncertainty. It must be noted that those manufacturing geopolymers often only use XRF data of the whole fly ash to determine Si:Al ratio so a formulation can be determined. Due to the importance of the Si:Al ratio, the practice of using only Si and Al values determined by XRF is not recommended. In the case of Collie fly ash, the use of the bulk Si:Al value will provide essentially the correct alkali formulation but the amount would be greater than needed resulting in efflorescence and a likely drop in strength.

The amount of Fe present in the form of hematite, maghemite and magnetite was determined to be 5.24 ± 0.16 wt.% compared with the total Fe of 10.72 ± 0.11 wt.% Fe as determined by XRF. This indicates that there is a substantial fraction of poorly ordered, small crystallite sized or amorphous iron oxide. Determining the role that amorphous Fe has upon the hydrothermal polycondensation reaction is critical for a complete understanding of geopolymers and their properties. If the Fe is present as Fe rich glass its presence may inhibit dissolution, lessening the amount of Si and Al present for geopolymerisation.

Winburn *et al.* (2000) commented that the mineralogy of fly ash was complex due to the chemical composition of solid solution phases as well as the effect of substitution. Mullite is difficult to refine as the level of substitution of Al^{3+} by Fe^{3+} is not known. Gomes and François (2000) conducted a rigorous analysis of mullite extracted from fly ash and also mention the nonstoichiometry of α–quartz and magnetite. Their study determined that mullite formed in fly ash is very heterogeneous due to the fast cooling rate of the process providing unfavourable conditions for crystallisation and homogenisation. It was found that Fe could substitute up to 7.5 wt.% Al followed by Ti with up to 0.6 wt.% substitution of Al. Gomes *et al.* (1999) and Warren and Dudas (1988) determined that magnetite extracted from fly ash had mainly Mg substituted for Fe and infrequent substitution of Ca, Mn and Si. Quartz can contain trace amounts of Fe and Al. Incorrect modelling of mullite XRD patterns can lead to significant differences in the estimated Al available in the amorphous aluminosilicate (Williams & van Riessen 2010). However, due to the trace amounts of Al that can be found within quartz, the value could once again be altered to be still more than what is already calculated or less. The same can be said for Si that can be substituted for Fe in magnetite.

Comprehensive analysis can be conducted to determine the exact degree of substitution however due to the random nature of fly ash (different from batch to batch even when using the same coal stream) it was decided that this level of characterisation was not justifiable. For the purposes of this project the reactive aluminosilicate was determined by XRD/XRF and chemical dissolution and results from the two approaches compared.

Based on the XRF/XRD analysis the amorphous content has 6.11 ± 0.12 wt.% Al and 11.92 ± 0.73 wt.% Si (values are of overall sample mass total). It is these relatively modest amounts that will be converted to geopolymer, although 100 % conversion is unlikely due to accessibility of the Si and Al in conjunction with limited time being available before setting starts. If only 50 % of the available aluminosilicate is dissolved and converted to geopolymer and then used as a binder in concrete, a remarkably small amount of material is responsible for keeping the concrete intact.

Further analysis of Collie ash was conducted via XRD data obtained using synchrotron radiation (Australian Synchrotron, Powder Diffraction Beamline). With superior signal-to-noise compared with laboratory XRD additional phases could be identified. The crystalline phases identified were hematite, maghemite C, magnetite, mullite, quartz and rutile. Corundum was also identified and could arise from the high temperature formation of hematite during the combustion process which expels most of the substituted Al from the structure, which then crystallises as corundum (Cornell & Schwertmann 2003) and from trace contamination arising from the microniser milling media.

Phase abundance from synchrotron based XRD was obtained using Rietveld refinement with results presented in Table 4.4.

Initially data from 3 repeat samples was collected by synchrotron XRD, however due to the small volume of the glass capillary and heterogeneity of fly ash, consistent sampling was not achieved. One dataset had to be discarded due to the large variations in the amorphous component and quartz values. Overall the synchrotron results showed slightly more maghemite C than magnetite when

compared with laboratory based results. This difference is believed to arise from the combination of better resolution and improved signal to noise which enabled the full pattern modelling to more accurately refined. When the values of rutile and corundum are added to the value of the amorphous content, the results are in agreement with those obtained from laboratory quantitative XRD.

QEMSCAN was also utilised in the analysis of the Collie fly ash. Mineralogical data was extracted with different phases being classified according to peak ratios derived from EDS data which could not be directly correlated with XRD data. Nevertheless the weight percent values in Table 4.5 are comparable to those acquired by XRF and quantitative XRD. Of key importance are the results of aluminosilicates (including iron rich aluminosilicates), quartz and iron oxides as they are the three largest fractions of the phases found within the fly ash.

The value determined by QEMSCAN for the combination of aluminosilicates was 61.39 wt.% which is comparable to the sum of mullite and amorphous Al, Si and O of 55.85 ± 1.36 wt.% obtained by combined XRD and XRF. The QEMSCAN value for quartz (18.21 wt.%) is comparable to the quantitative XRD result (21.81 ± 0.75 wt.%). The QEMSCAN value for iron oxide (18.61 wt.%) includes both the crystalline component (7.42 ± 0.22 wt.%) and the amorphous iron oxides (7.91 ± 0.22 wt.%) leaving a difference of 3.28 wt.%. This discrepancy is believed to arise from finely dispersed iron oxide in aluminosilicate (Figure 4.6) that cannot be resolved by the QEMSCAN and has been included in with the “iron-rich aluminosilicate” category. The discrepancy in the values derived from QEMSCAN and XRD/XRF can be in part attributed to the spatial resolution of approximately 1 µm in the QEMSCAN which leads to the over-representation of smaller particles or those adjoining another phase. Overall QEMSCAN has demonstrated itself to be a viable technique for analysis of fly ash that compliments traditional methods such as XRF and XRD.

Table 4.4: Phase abundance of Collie fly ash obtained from Rietveld refinement with synchrotron XRD data of 2 samples of fly ash powder (TOPAS) using an internal standard.

Phase	Composition (wt.%)
Amorphous	56.39 ± 1.00
Corundum	1.31 ± 0.04
Hematite	2.12 ± 0.07
Maghemite C	3.58 ± 0.16
Magnetite	2.26 ± 0.13
Mullite	15.55 ± 0.08
Quartz	18.29 ± 0.65
Rutile	0.50 ± 0.03

Table 4.5: QEMSCAN mineral weight % of Collie fly ash. Uncertainties based on number of points analysed.

Designated Mineral Name	Weight %
Aluminosilicates	45.31 ± 0.20
Iron Rich Aluminosilicates	16.08 ± 0.08
Quartz	18.21 ± 0.09
Rutile	0.76 ± 0.01
Iron Oxides	18.61 ± 0.09
Calcium Silicate	0.13 ± 0.01
All Others	0.91 ± 0.01

Collie fly ash typically consists of spherical particles, irregularly shaped quartz, vitreous particles and carbon. The spherical particles are comprised of amorphous aluminosilicate material with crystalline material encapsulated within the spheres. The crystalline phases that are encapsulated within these spheres are mullite, hematite, maghemite and magnetite. Collie fly ash is mostly comprised of solid spherical particles and some irregularly shaped glass particles (Figure 4.5). Many other fly ashes also have proportion of cenospheres (hollow spherical shells) which are not obvious in Collie fly ash (Fernandez-Jimenez *et al.* 2005). Some of the Collie fly ash spheres with encapsulated crystalline material may contains pores from minute amounts of gas that were trapped during the formation and resultant crystallisation. Irregularly shaped glass particles usually contain large pores in proportion to their size.

Primary quartz particles are present as separate entities to the carbon, irregularly shaped glassy particles and spherical particles. Secondary quartz is also found within the stereotypical fly ash spheres (Figure 4.6). These observations demonstrate the influence that the rapid cooling has on fly ash production, preventing homogenisation of particles and complete crystallisation of phases.

Cross sectioned fly ash spheres examined by SEM generally exhibit mixed phases with the exception of spheres predominately composed of iron oxide (Figure 4.7) or mullite. The amorphous aluminosilicate content of these particles tends to be very low. For the mullite rich spheres it is possible that there was sufficient time for the aluminosilicate material to crystallise into mullite, albeit with small grains. The iron oxide dominated particles are believed to be remnants of iron oxide found within liberated coal.

Particles larger than 45 µm were mostly irregularly shaped carbon, quartz and partly fused clay minerals (Figure 4.8). The majority of fly ash particles greater than 45 µm were found to be solids spheres however a few hollow cenospheres were encountered within this size fraction.

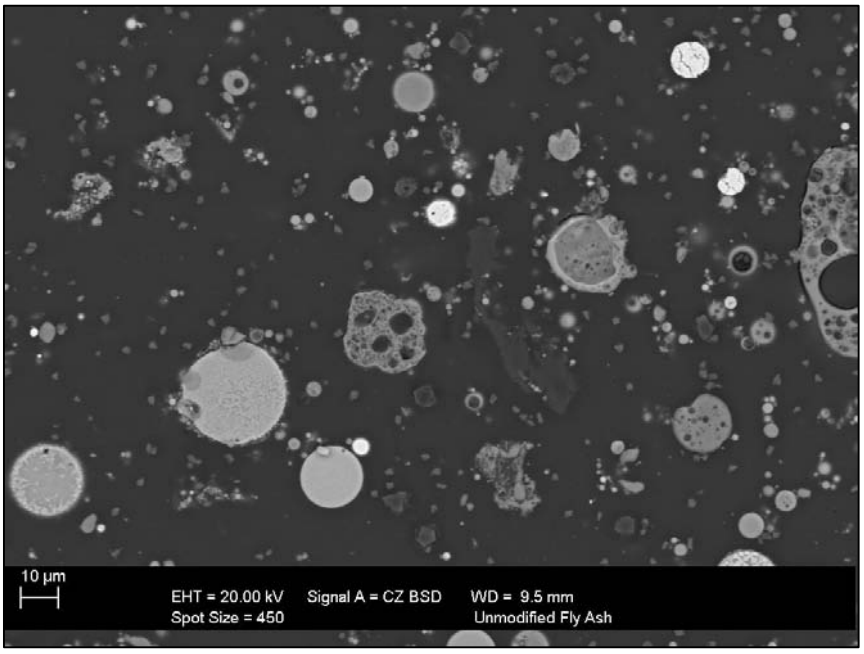

Figure 4.5: Backscattered electron image of a polished cross section of Collie fly ash showing mostly solid spherical particles and some irregularly shaped glass particles. (Zeiss EVO 40XVP)

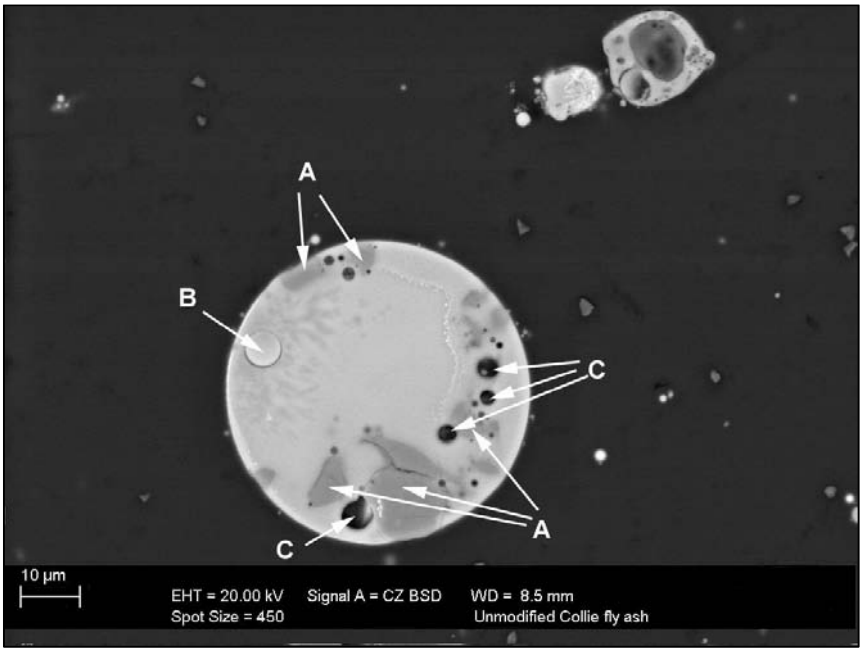

Figure 4.6: Cross section of a spherical fly ash particle consisting of several phases. The bulk of the sphere is comprised of very small iron oxide crystals (lighter area) embedded within the glassy phase (darker area). Additional phases are encapsulated quartz (A), another spherical iron rich fly ash particle (B) and pores (C). (Zeiss EVO 40XVP)

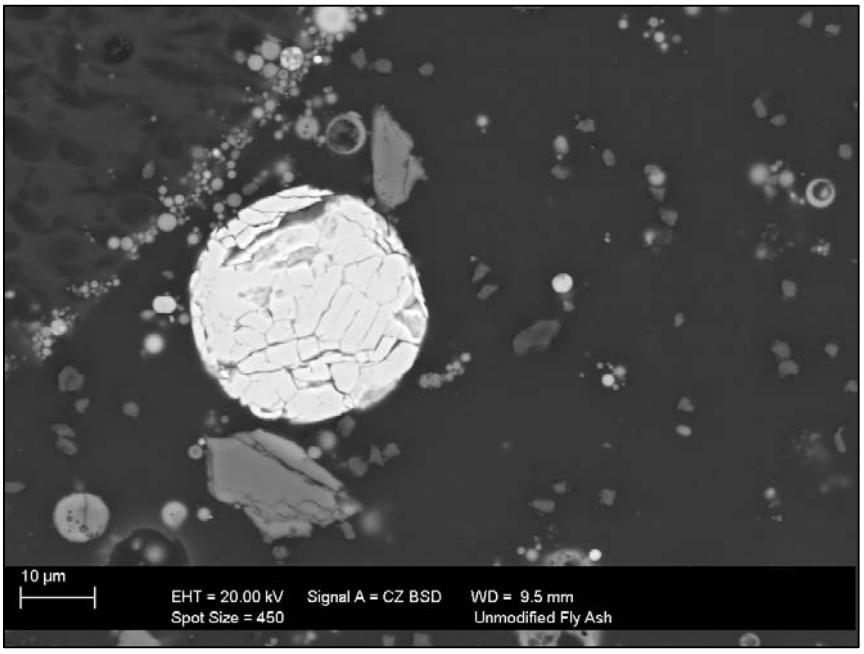

Figure 4.7: Cross section of an iron oxide dominated fly ash sphere with little evidence of glassy aluminosilicate material. (Zeiss EVO 40XVP)

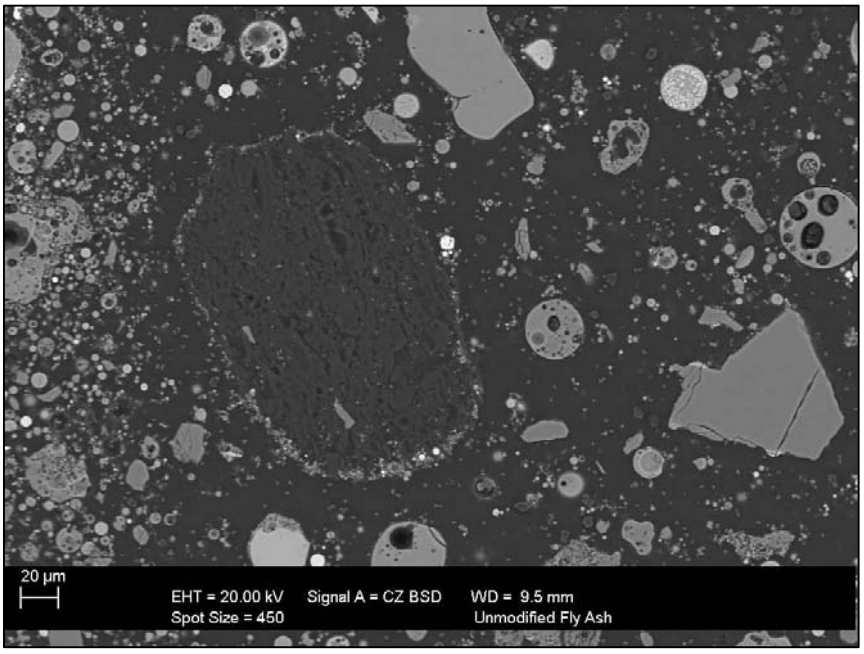

Figure 4.8: Backscattered electron image of a polished cross section of Collie fly ash showing an amorphous carbon particle and the irregularly shaped quartz particles intermixed with spherical fly ash particles. Irregularly shaped glassy particles are found on the left border of the image. (Zeiss EVO 40XVP)

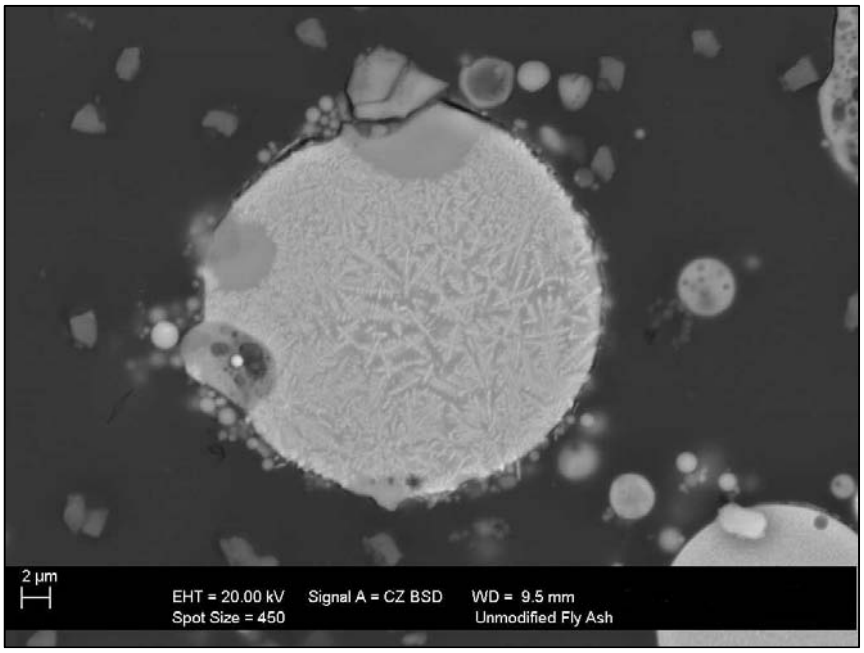

Figure 4.9: Backscattered electron image of a polished cross sectioned fly ash particle comprising of iron oxide particles (hematite and/or maghemite) encapsulated by the reactive amorphous material. (Zeiss EVO 40XVP)

The presence of crystalline material embedded in the amorphous content creates a physical barrier impeding the dissolution process (Figure 4.9).

Fernandez-Jimenez *et al.* (2005) concluded that the dissolution process for hollow fly ash spheres is through attack on a portion of the outer surface and when this penetrates it allows bi-directional alkaline attack (i.e. from both sides of the sphere wall) prior to conversion to geopolymer. The resultant geopolymer then acts as a barrier against further dissolution, protecting the remaining reactive material. The resulting microstructure is a mix of undissolved and partially dissolved fly ash particles bound together by geopolymer. As the majority of Collie fly ash particles are solid spheres of reactive aluminosilicate with embedded hematite, maghemite, magnetite or mullite it is clear that the process defined by Fernandez-Jimenez *et al.* (2005) is not applicable.

QEMSCAN elemental mapping complimented the SEM imaging by displaying particle size and composition (mineralogy) for a large number of particles (Figure 4.10). It can be seen that the majority of spherical particles are comprised of ‘mullite’, ‘high iron mullite’ and iron oxide. As QEMSCAN categorises phases

according to preset elemental ratios it is unable to distinguish crystalline phases from amorphous phases. Because of this the 'mullite' category could be crystalline mullite or amorphous aluminosilicate material and 'high iron mullite' could be crystalline mullite with iron substitution or amorphous iron rich aluminosilicate material. QEMSCAN also highlighted that quartz and rutile phases were found to be comprised of irregularly shaped particles which were generally separated from other phases.

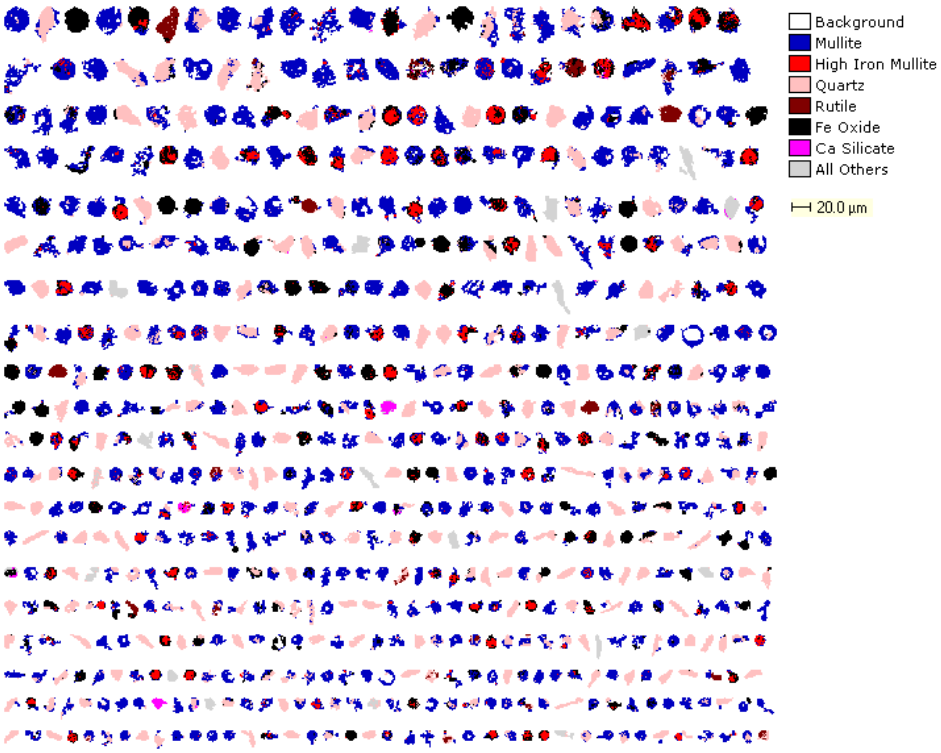

Figure 4.10: A sampling of the morphology and composition of Collie fly ash particles determined by QEMSCAN (CSIRO Minerals Waterford).

4.4 Reactivity

In order to determine the reactivity of Collie fly ash, a series of dissolution experiments were initiated. An important aspect of this work was to ascertain if the amorphous content as determined by XRD was the same as the reactive component determined by dissolution. Dissolution was undertaken by placing a relatively small amount of fly ash in a large volume of alkaline solution and agitating the mixture (details provided in Section 3.3). At set times the undissolved component was weighed and compared with the initial starting mass.

Dissolution was initially trialled at room temperature due to standard mixing being conducted at room temperature. A series of times were chosen ranging from 5 minutes up to 24 hours. The NaOH solution was not refreshed during this experiment and it was expected that there would be formation of geopolymer gel towards the end of the experiment. It was also expected that due to the long periods of time in which the solids would be saturated in NaOH solution, the normally unreactive crystalline phases would also start to dissolve as seen in typical hydrothermal zeolite production. Figure 4.11 displays the results from this initial trial.

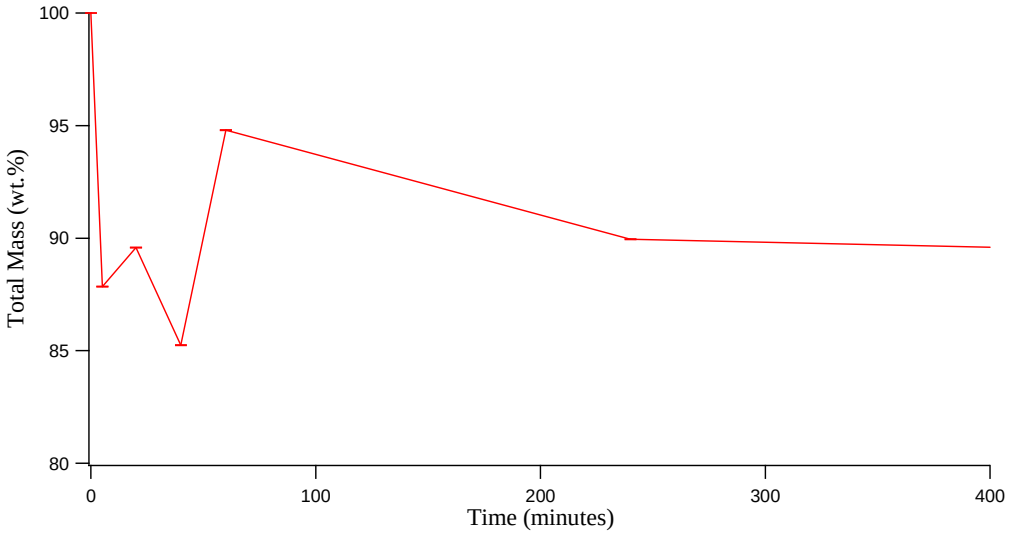

Figure 4.11: Dissolution of Collie fly ash in 10 M NaOH at room temperature. Error bars for total mass are too small to be clearly visible.

As shown in Figure 4.11, a proportion of the amorphous aluminosilicate is readily dissolved by alkaline solution, resulting in approximately 15 wt.% mass loss by 40 minutes. This is followed by a sudden mass gain of approximately 10 wt.% by 60 minutes. The mass gain was ascribed to polycondensation of Al and Si ions into geopolymer gel and precipitating out of solution. A much slower reduction in mass occurs after 60 minutes which was believed to be due to the normally unreactive crystalline materials being slowly dissolved. An additional factor that would aid in the dissolution is the increase in temperature due to the exothermic reaction that would occur if the polycondensation reaction is triggered during the mixing phase.

As room temperature dissolution resulted in little change of the amorphous content, the experiment was repeated at an elevated temperature of 75 °C. This was

justified as the normally exothermic reaction combined with a curing temperature of 75 °C would result in these conditions. The higher dissolution temperature resulted in 38.74 wt.% mass loss compared with 14.75 wt.% mass loss for the ambient temperature dissolution. The maximum mass loss was measured at approximately 60 minutes (Figure 4.12). After 60 minutes there is a mass gain of approximately 15 wt.% before a slow decrease in mass after approximately 2 hours. The mass gain followed by mass loss was again ascribed to the precipitation of geopolymer gel from solution followed by dissolution of the crystalline material.

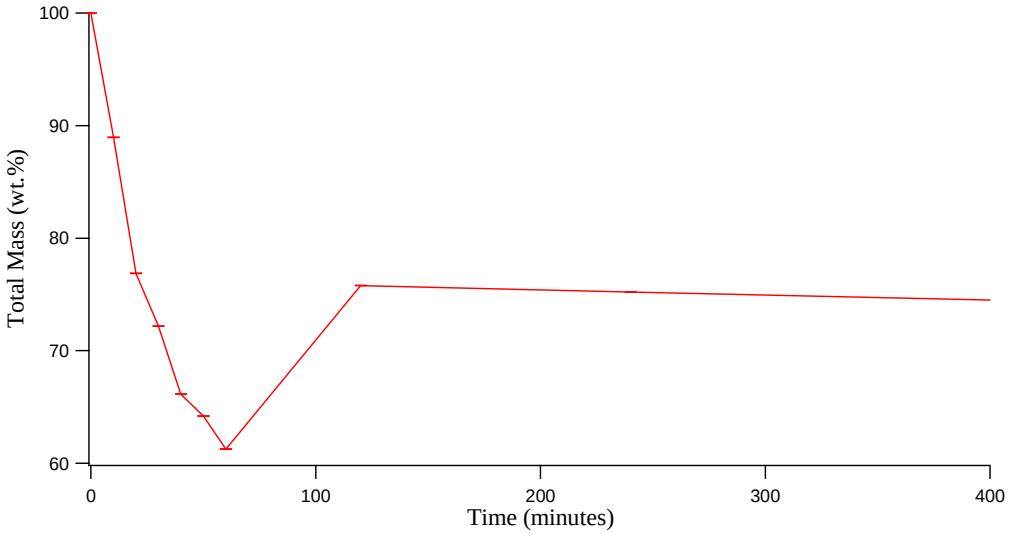

Figure 4.12: Dissolution of Collie fly ash in 10 M NaOH at 75 °C. Error bars for total mass are too small to be visible.

Due to the relatively large ratio of sodium hydroxide solution to fly ash and elevated temperature utilised in this experiment, zeolite was also expected to form. In fact geopolymer gel and zeolite (identified as sodalite) begin to precipitate out of solution after approximately 30 minutes. This precipitation is predominately noticeable after the maximum consumption of the amorphous content (at approximately 1 hour). Due to this, mass loss results will be affected leading to lower measured values.

The change in levels of amorphous material in fly ash with alkaline dissolution was also monitored via XRD. The original Collie fly ash displays a distinct amorphous peak in the XRD pattern at approximately 23 ° 2θ while the fly

ash submerged in NaOH (60 minutes at 75 °C) displays no evidence of an amorphous peak (Figure 4.13).

The gradual formation of geopolymer gel can also be tracked by XRD over time. For extended dissolution periods, the geopolymer gel crystallises into zeolites (sodalite) (Figure 4.14 and Figure 4.15).

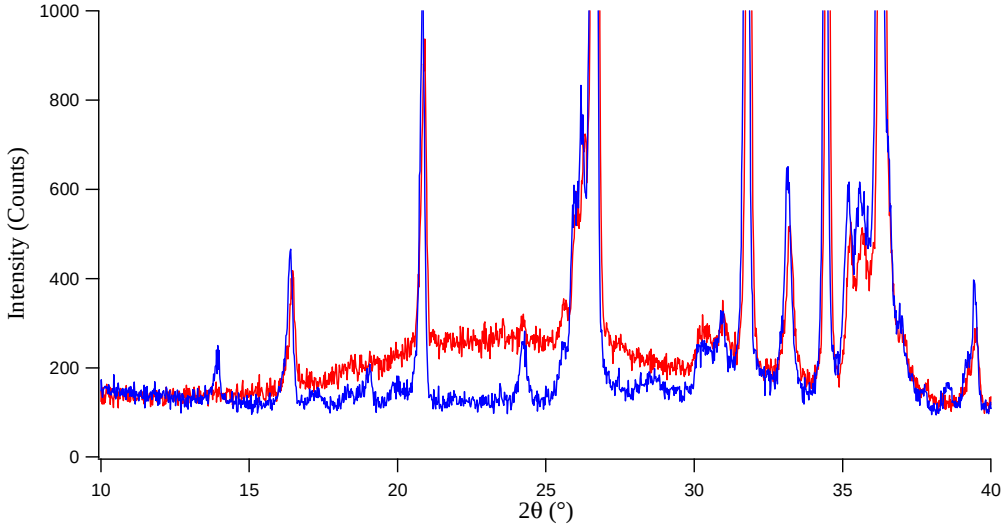

Figure 4.13: Comparison of original Collie fly ash (red) with Collie fly ash that has undergone dissolution for 60 minutes at 75 °C (blue). (Siemens D500)

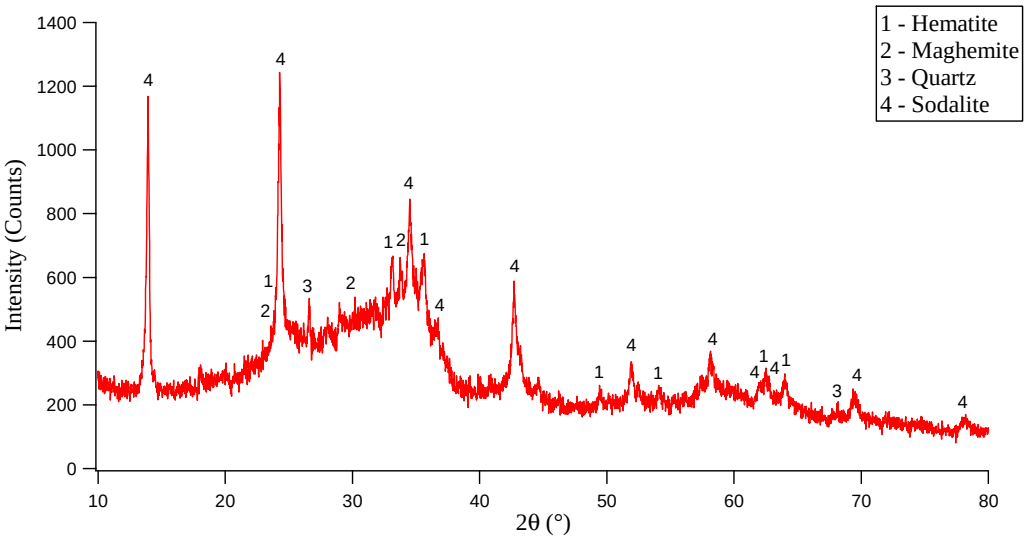

Figure 4.14: XRD pattern of Collie fly ash that has undergone dissolution in 10 M NaOH solution for 24 hours at 75 °C. (Siemens D500)

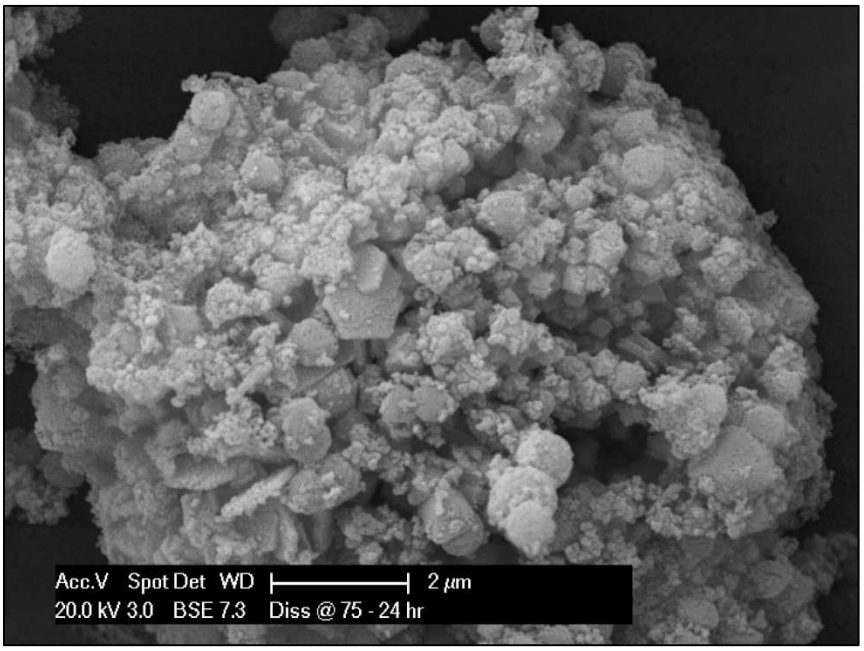

Figure 4.15: Backscattered electron image of zeolite (sodalite) and geopolymer formed after 24 hours of dissolution at 10 M NaOH at 75 °C. (Philips XL30)

The liquid from the dissolution experiment became a dark hue of orange with extended dissolution times. The orange colouration is caused by amorphous Fe being dissolved into solution and forming ferrihydrite. The filtered liquid from the dissolution experiment conducted for 60 minutes and at 75 °C was centrifuged leading to the separation of a dull orange coloured solid residue and a clear solution. The centrifuged solid residue was analysed using XRD and SEM. From the results it was evident that Al, Fe and Si were leached as the precipitate of the filter solution was the crystalline phase of zeolite-X and nano-crystalline 2-line ferrihydrite after a few weeks of settling (Figure 4.16 and Figure 4.17). The formation of 2-line ferrihydrite (Cornell & Schwertmann 2003, Ristić *et al.* 2007) was confirmed by two characteristic broad peaks situated at approximately 35 º and 62 º 2θ. According to Daux *et al.* (1997) the precipitation rate of Fe is higher than Al and Si, suggesting that the ferrihydrite would precipitate prior to the formation of either geopolymer gel phases. The broadness of the first peak suggests that there is additional geopolymer material which has yet to convert to zeolite-X.

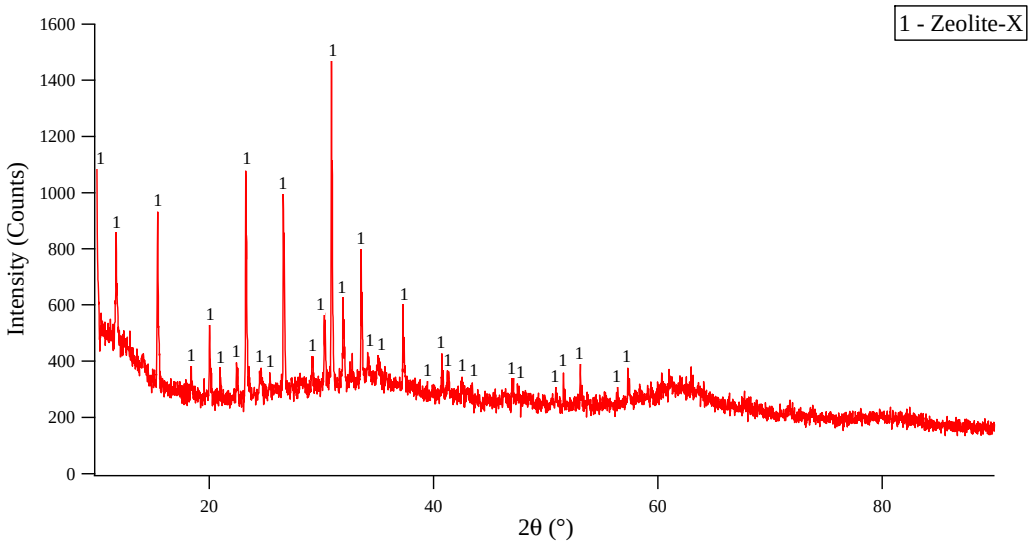

Figure 4.16: XRD pattern of Collie fly ash that has undergone dissolution in 10 M NaOH solution for 24 hours at 75 C. (Bruker D8 Advance).

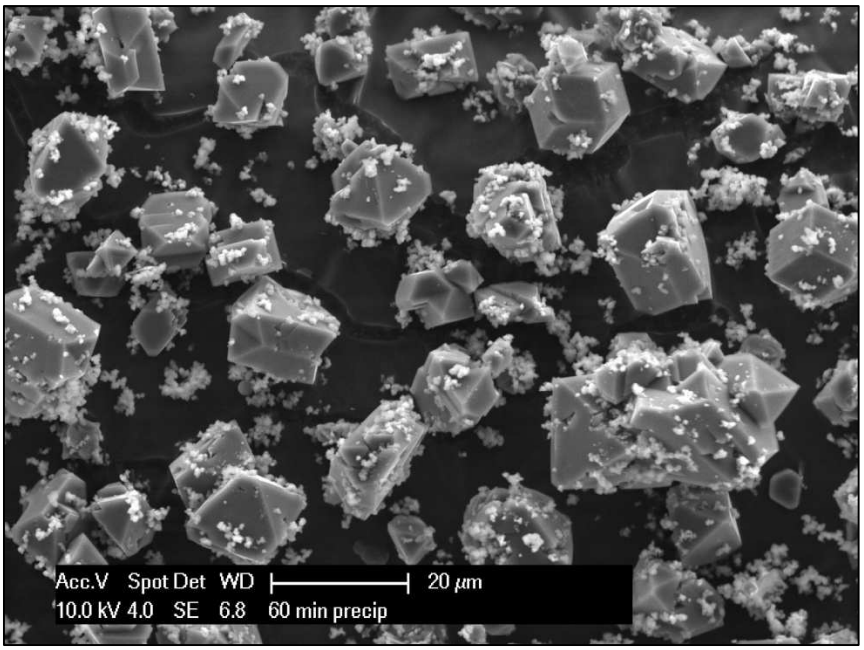

Figure 4.17: Secondary electron image of precipitate from the liquid filtered from dissolution of Collie fly ash for 60 minutes at 10 M NaOH at 75 °C. Image displays crystalline zeolite-X and nano-crystalline ferrihydrite. (Philips XL30)

Figure 4.18 shows that some of the spherical particles are comprised of a core of densely packed crystalline material, such as mullite, which was originally covered by amorphous aluminosilicate.

Due to the densely packed nature of the crystalline content (Figure 4.18 and Figure 4.19), it is likely that a fraction of the amorphous aluminosilicate material will be difficult to access by a limited amount of liquid alkaline activator typically used for production of geopolymer. These constraints will limit the consumption of reactive amorphous aluminosilicate material in typical geopolymer formulations. The Al and Si ions will primarily be provided by the amorphous aluminosilicate material which is present as the outer shell of the spherical fly ash particles.

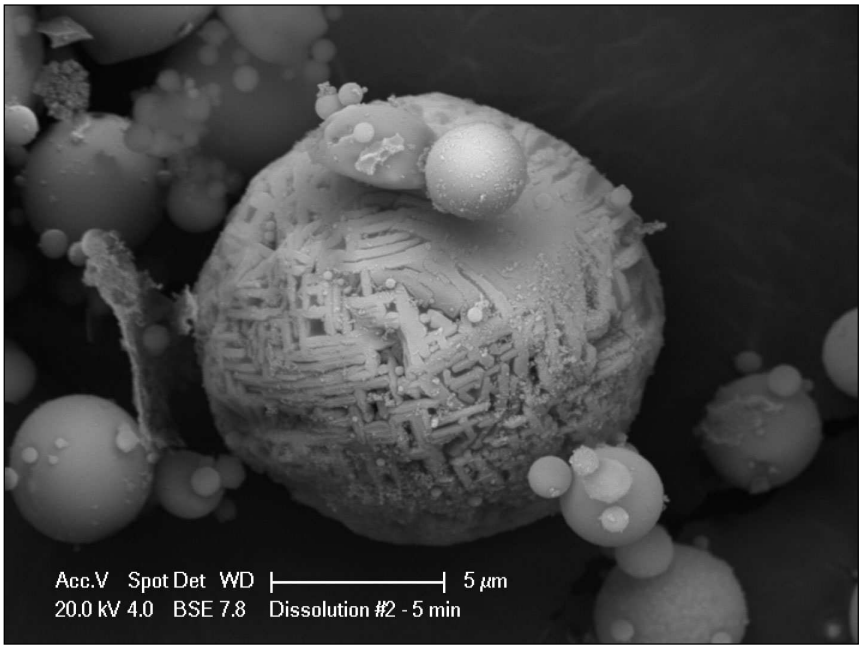

Figure 4.18: Backscattered electron image of a fly ash sphere with surface layer of amorphous aluminosilicate removed by NaOH dissolution revealing encapsulated crystalline mullite. (Philips XL30)

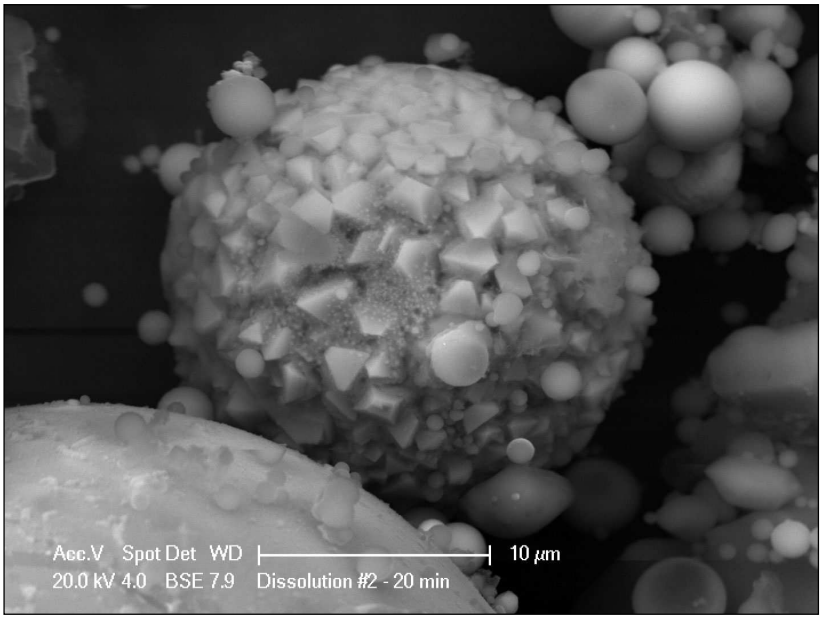

Figure 4.19: Backscattered electron image of a fly ash sphere with surface layer of aluminosilicate amorphous material removed by NaOH dissolution. Shown is the encapsulated crystalline iron oxide (magnetite) and geopolymer which has started depositing in place of the original amorphous material. (Philips XL30)

QEMSCAN analysis of fly ash residue after dissolution show that levels of aluminosilicates and iron rich aluminosilicates have decreased as expected but there is a significant increase in the relative fraction of iron oxides (Table 4.6).

Table 4.6: QEMSCAN results showing mineral fraction of fly ash after various times of dissolution in NaOH.

Mineral Name	Weight % (Original)	Weight % (30 min)	Weight % (1 hr)
Aluminosilicates	45.31 ± 0.20	36.60 ± 0.20	17.36 ± 0.09
Iron Aluminosilicates	16.08 ± 0.08	9.32 ± 0.05	5.40 ± 0.03
Quartz	18.21 ± 0.09	18.53 ± 0.09	22.50 ± 0.10
Rutile	0.76 ± 0.01	0.73 ± 0.01	1.60 ± 0.01
Fe Oxides	18.61 ± 0.09	32.10 ± 0.20	48.20 ± 0.20
Ca Silicates	0.13 ± 0.01	0.49 ± 0.01	0.59 ± 0.01
All Others	0.91 ± 0.01	2.27 ± 0.01	4.41 ± 0.02

The result from this dissolution experiment clearly indicates that more than half of the combined aluminosilicates and iron aluminosilicates have been consumed within the first hour of dissolution. The reduction of the iron aluminosilicates indicates the dissolution of the amorphous Fe by the alkaline solution. The amounts of quartz, rutile and calcium silicate phases show very little change. This would indicate that these three phases are reactive, however at a slower rate. The most significant change is the increase in the proportion of Fe oxides found in the samples as the fly ash is progressively digested. The large amount of Fe is due to sum of the relatively inert crystalline Fe oxides with ferrihydrite formed by the rapid re-precipitation of the amorphous Fe as ferrihydrite while the Al and Si ions were still in solution (Daux *et al.* 1997, Cornell & Schwertmann 2003, van Deventer *et al.* 2007).

The formation of ferrihydrite demonstrates that the amorphous Fe does not play a role in the geopolymerisation process. However it does impinge upon the

dissolution and subsequent geopolymerisation process as the amorphous Fe consumes OH^- from the activating solution. This leads to a drop in pH and therefore the potency of the activating solution. As only a limited amount of activating solution is utilised in synthesising geopolymer, a decrease in pH would have a noticeable impact on reactivity leading to less formation of geopolymer material.

van Deventer *et al.* (2007) suggests that the ferrihydrite could act as nucleation sites for geopolymerisation and resultant zeolite formation. Rees *et al.* (2007) demonstrated that seeds for nucleation do accelerate the formation of geopolymer gel, shortening the induction period (Cundy & Cox 2005, Rees *et al.* 2007) prior to geopolymer gel formation. However, the experiment by Rees *et al.* (2007) was conducted in conditions favouring zeolite formation so the exact impact the ferrihydrite seeds have upon geopolymerisation is not clear.

This concludes the first dissolution experiment. Additional dissolution experiments were conducted for sieved fly ash and sieved and milled fly ash.

4.5 Summary

- Collie fly ash is a Class F fly ash based on low Ca and high Fe content (ASTM 618).
- Fly ash is difficult to characterise due to its heterogeneity being a mixture of crystalline and amorphous components.
- The primary constituents of Collie fly ash are amorphous aluminosilicate, hematite, maghemite C, magnetite, mullite and quartz. Corundum and rutile present in low concentrations were only detectable by synchrotron XRD.
- Amorphous aluminosilicate content is approximately 40 wt.%.
- Amorphous (reactive) Al is approximately 6 wt.%.
- Amorphous (reactive) Si is approximately 12 wt.%.
- Amorphous Fe precipitates as ferrihydrite prior to geopolymer gel formation.
- Formation of ferrihydrite requires OH^- from solution. This leads to the reduction of activating solution potency.
- Ferrihydrite has the potential to act as nucleation sites.

- Unreactive crystalline phases (with the exception of quartz and rutile) are generally encapsulated by amorphous aluminosilicate in spheres therefore restricting the penetration of alkaline activator solution. This limits the reactivity of the overall amorphous content.

Chapter 5

Beneficiation of Fly Ash

5.1 Introduction

The reactivity of fly ash for the synthesis of geopolymer is dependent upon the accessibility of the vitreous content by the alkaline activating solution. The role of the fly ash beneficiation is to enhance the accessibility to the reactive component of the ash.

Beneficiation of the fly ash was conducted in three stages. The first stage involved the removal of extraneous quartz and carbon by sieving. The second stage was to increase surface area of individual particles by milling the sieved ash. The third stage was the removal of the magnetic component from the sieved and milled fraction. With the removal of extraneous material in conjunction with increasing surface area, the activating solution has a greater opportunity to access the amorphous aluminosilicate leading to a greater degree of geopolymerisation. It should be noted that on a commercial scale electrostatic separation, cyclone classification and flotation are available for separation of particles according to size and density (http://www.mineraltechnologies.com.au).

Previous studies by Willis (2003) indicated that milling increased the reactivity of the vitreous content in the fly ash. However, Willis did not investigate the impact that increased reactivity would have upon the Si:Al:M (where M is the alkaline cation) ratio due to the increased rate of reaction. Willis also improved the homogeneity of his samples by centrifuging the feedstock and activating solution prior to curing. Centrifuging was anticipated to lead to segregation of the crystalline particles and geopolymer paste leading to a dense homogeneous matrix. As centrifuging is expensive and not commonly employed in industry it was decided that this technique would not be adopted in this study.

The sieving process removes large quartz and carbon particles from the fly ash leading to increased reactivity as there is less filler material to hinder the aluminosilicate inorganic polymerisation process via physical blocking of the alkaline solution during the mixing process. In addition, carbon particles are either partially or fully activated and have the ability to attract water and cement additives leaving insufficient quantities for geopolymerisation. The removal of the coarse material also improves homogeneity of the final material improving their suitability for specialist applications such as fire resistant and acid resistant coatings. The removed phases could also generate an additional revenue stream, such as activated carbon for gas filtration.

Beneficiating the fly ash is anticipated to lead to geopolymers with superior physical properties. However, beneficiation introduces a number of additional costs such as monetary, carbon emission and man power. These costs generally determine the probability of the process being adopted by industry. Thus if a beneficiation process bring small benefit at a large cost then it will not be implemented.

5.2 Removal of Unreactive Phases

XRD analysis of Collie fly ash (Chapter 4) showed the main crystalline phases to be hematite, maghemite, magnetite, mullite and quartz. These phases are not dissolved by the alkali during geopolymerisation and are classified as unreactive. Amorphous carbon particles are unreactive components of fly ash however amorphous iron associated with the amorphous content can be dissolved by the OH^- of the solution and reform as ferrihydrite. As the amorphous iron is dissolved alongside the aluminium and silicon by the activating solution, it impacts upon the kinetics of the dissolution and gel formation process by reducing the pH of the solution (van Deventer *et al.* 2007). The ferrihydrite does not directly contribute to the geopolymerisation process but may act as nucleation sites for the formation of geopolymer and zeolites (Cundy & Cox 2005, Rees *et al.* 2007).

Particles greater than 50 µm in diameter are generally quartz, carbon (of varying morphologies) and irregular shaped particles derived from fused clay particles. If sample preparation is poor, the spheres can agglomerate into clusters in

excess of 50 µm. Agglomeration prevents full utilisation of vitreous content due to shielding of the inner particles by the outer layer of particles. Agglomeration can be minimised by the use of high shear mixing in conjunction with adequate wetting when the feedstock is combined with the alkaline activating solution.

Immersion of the fly ash in NaOH solution resulted in dissolution of the outer layer of amorphous material leaving residual mullite and iron oxides (Figure 5.1). This indicates that the removal of mullite and iron oxides would require the fly ash to be ground prior to applying a secondary process of particle size or magnetic separation.

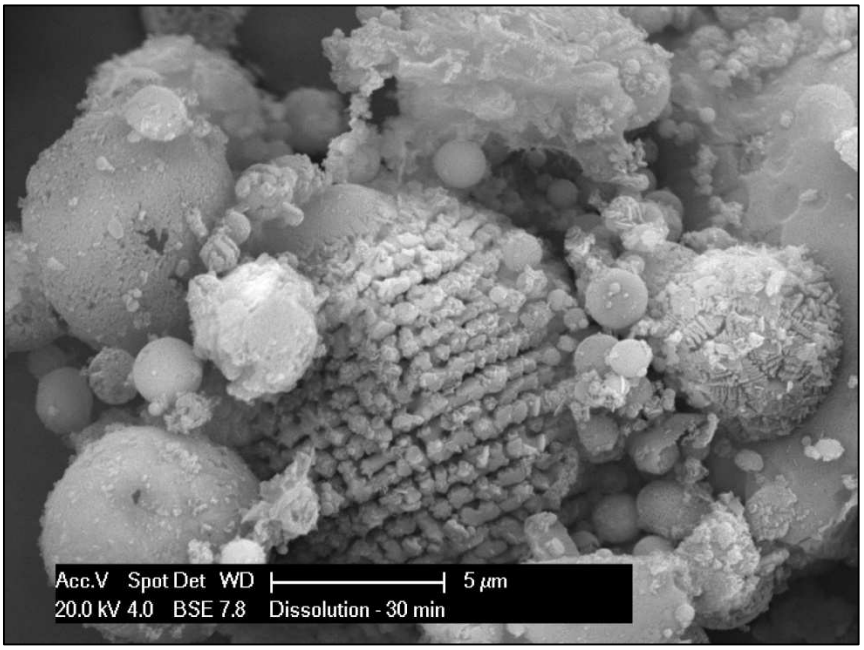

Figure 5.1: Backscattered electron image showing fly ash sphere remnants after immersion in NaOH solution (10 M). (Philips XL30)

Even with fine grinding the removal of embedded mullite and iron oxides is likely to result in considerable loss of the amorphous material. This loss of feedstock during processing must be balanced against potential improvement of overall physical and mechanical properties of the final product. It should be noted that phases removed during beneficiation can be reclaimed and used as by-products in their own right. For instance crystalline iron oxides (7.42 wt.%), mullite (16 wt.%), quartz (21.81 wt.%) and carbon all have intrinsic value.

Though there are methods for the removal of a majority of the crystalline phases, the removal of the very fine mullite is impossible without the direct dissolution of the encapsulating amorphous content. Since the amorphous material is the cornerstone of geopolymerisation, the removal of mullite is less important compared to the preservation of the amorphous material.

5.2.1 Flotation

Flotation is a technique utilised frequently in mineral processing for separating phases of different density. Flotation was trialled as a method for the removal of amorphous carbon from the bulk fly ash as SEM imaging shows carbon is present as discrete particles.

5.2.1.1 Flotation using Distilled Water

Flotation consisted of slowly adding fly ash to distilled water. Amorphous carbon with some cenospheres (Figure 5.2) was successfully separated from the rest of the fly ash. This float represented 0.60 ± 0.06 wt.% of the total sample and 23 % of the LOI. The lower than expected float is attributed to particle agglomeration preventing the lower density particles from freeing themselves even after agitation in the liquid. Therefore when the fly ash sample is introduced to the liquid medium, a majority of the lighter particles will be dragged to the bottom by the weight of the heavier particles which are intermixed with them.

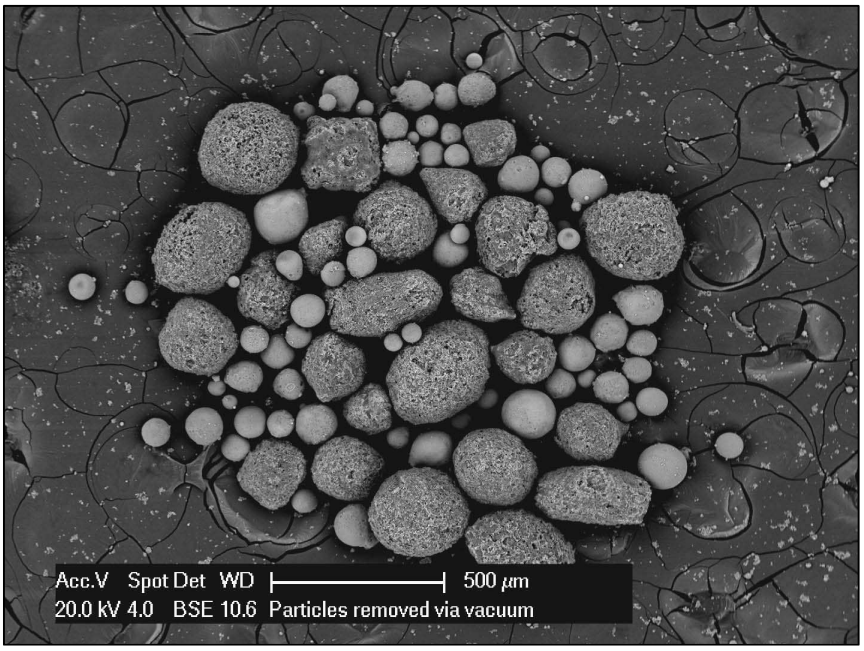

Figure 5.2: Backscattered electron image of particles removed from the surface of de-ionised water. The dark larger particles are carbon with the remaining particles being cenospheres. (Philips XL30)

5.2.1.2 Froth Flotation

Froth flotation was also trialled. Diesel was selected as the surfactant for the amorphous carbon with methyl isobutyl carbinol used as the frothing agent. Within minutes of adding the diesel to the fly ash a noticeable reflective black scum appeared on the surface. Scooping away the scum from the surface also resulted in collection of a moderate amount of fly ash spheres. This lead to a removal of 27.03 ± 0.01 wt.% of the sample as float which is significantly larger than the 2.06 ± 0.07 wt.% obtained by LOI. The large amount of fly ash spheres removed was confirmed by SEM imaging of the float (Figure 5.3). For this trial it was not possible to determine the true froth contents due to the inclusion of fly ash spheres. It is conceivable that froth flotation could be an effective and efficient method for the removal and recovery of the carbon particles found within fly ash. However, during the timeframe of this project there wasn't a flotation cell with a precise screeding procedure available for the removal of the true froth content. This limitation prevented further investigation of both the froth float and residue. The effect of diesel and methyl isobutyl carbinol frothing agent on geopolymerisation also needs to be determined. Though the quantities utilised for generation of froth and as a

surfactant are minor, a thin surface coating may have a significant impact upon the geopolymerisation process.

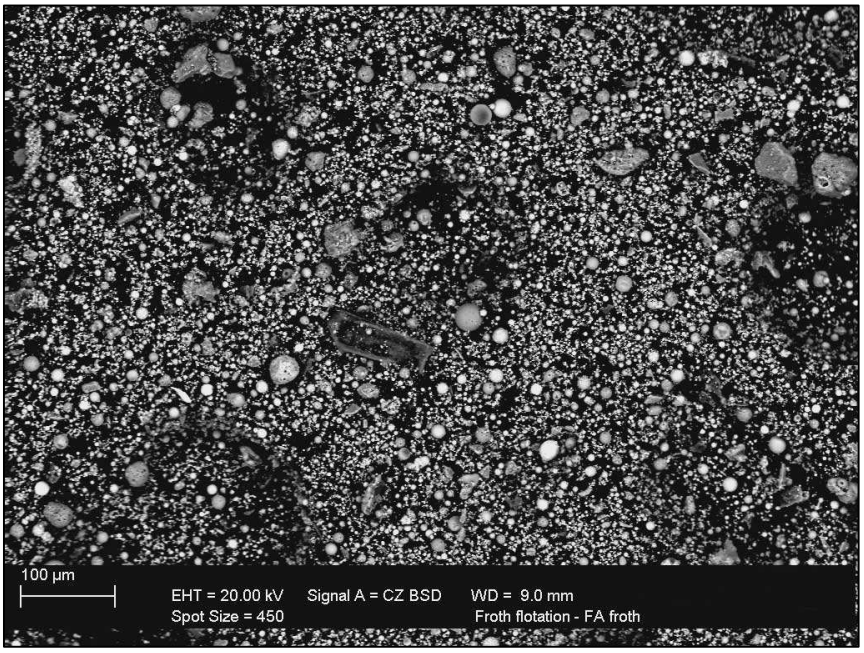

Figure 5.3: Backscattered electron image of surface particles removed by froth flotation. Large amounts of fly ash spheres and quartz are present. (Zeiss EVO 40XVP)

5.2.2 Sieving

Sieving for particle size separation is a simple and inexpensive process. When scaled up for industrial application, other forms of particle sizing such as cyclonic separation could be utilised (Jones *et al.* 2006) or for finer fractions (3 – 5 µm) a centrifugal zigzag classifier (example at http://www.hosokawa.co.uk/zigzaglab.php) can be used.

In this project, Endecotts laboratory test sieves were utilised as a method of dry separation. By using a combination of 75 µm and 45 µm mesh sieves, three size fractions were obtained, namely > 75 µm (coarse), ≤ 75 µm ≥ 45 µm (medium) and < 45 µm (fine).

The mass fraction of each size range given in Table 5.1 shows the majority of fly ash is below 45 µm in size. Laser particle sizing was utilised as a complimentary

analysis technique to the mass fraction separation by sieving. XRD was conducted to determine the phases present in each size fraction with SEM imaging used as a cross check. It was anticipated that the larger particles would primarily consist of carbon and quartz particles as shown in Figure 5.2.

Table 5.1: Size fractions of Collie fly ash after sieving. Uncertainties are one standard deviation of 3 analyses.

Size Fraction	Mass (wt.%)
Coarse (> 75µm)	7.22 ± 0.05
Medium (≤ 75 ≥ 45 µm)	8.24 ± 0.05
Fine (< 45µm)	84.05 ± 2.19

The fine fly ash was further sized and compared with unmodified fly ash using a Malvern MS2000 (CSIRO Minerals, Waterford) to determine the size distribution. Results (Figure 5.4) showed that more than 95% of the sample was below 45 µm. Particles greater than 45 µm in the sieved fraction are believed to be rod like particles which are able to pass through the sieve.

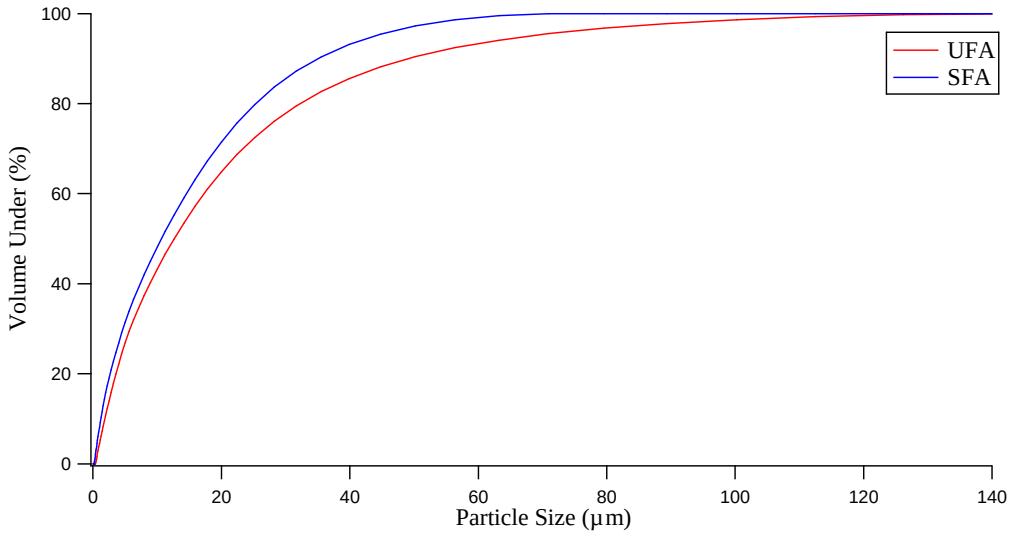

Figure 5.4: Comparison of laser particle sizing of Collie fly ash (UFA) and fine fly ash (SFA).

Visual inspection (Figure 5.5) of the different size fractions shows clear differences in colour ascribed to differences in composition. It can be seen that for

the coarse and medium fractions, the majority of the particles are quartz due to the grey colouration and the coarse/grainy texture. Large black carbon particles can be seen in the coarse fraction. With the removal of a moderate amount of quartz and carbon, the visual difference between the unmodified fly ash and fine fly ash is the contrast between a darker hue of brown (unmodified fly ash) to the lighter hue of brown (fine fly ash).

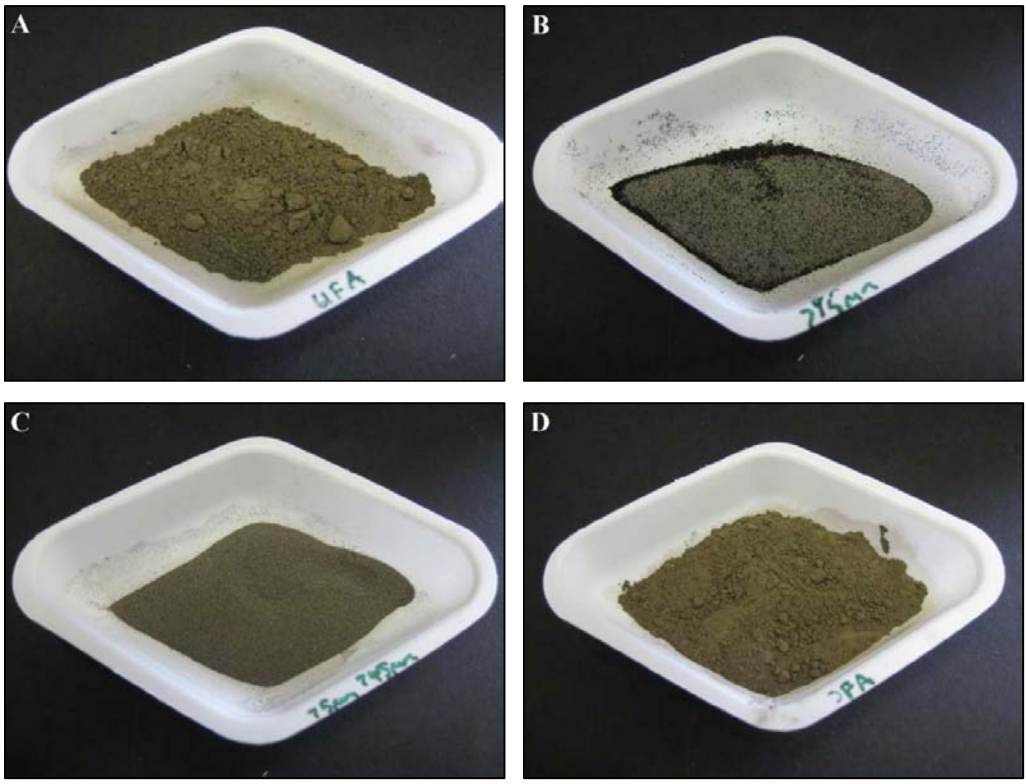

Figure 5.5: Images of (A) unmodified fly ash (B) coarse fly ash (C) medium fly ash (D) fine fly ash.

Loss on ignition values for the different size fractions (Table 5.2) gives an indication of the distribution of activated carbon and the efficiency of the sieving process.

Table 5.2: Loss on ignition values (1050 ºC) of different size fractions of Collie fly ash. Uncertainties are one standard deviation of 5 samples.

Size Fraction	LOI (wt.%)	Overall Contribution (wt.%)
Coarse	5.59 ± 1.35	0.40 ± 0.10
Medium	1.36 ± 0.31	0.11 ± 0.03
Fine	1.71 ± 0.03	1.45 ± 0.03

The LOI results show that sieving is only capable of removing approximately 25 % of the total carbon content (2.06 ± 0.07 wt.%) found in Collie fly ash. Contrary to expectations the fine fly ash contains more than 70 wt.% of the carbon, clearly indicating that the majority of unburned carbon particles are very small (Figure 5.6).

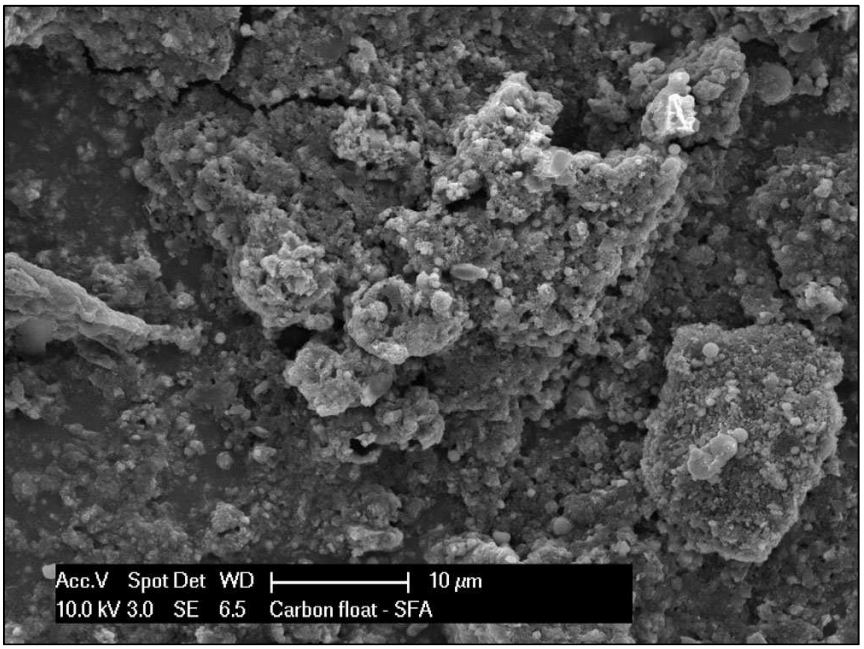

Figure 5.6: Secondary electron image of floated carbon particles from fine fly ash. Particles appear to be clumps of agglomerated carbon. (Philips XL30)

The following section will consist of a commentary of SEM images and XRD patterns of the three size fractions (coarse, medium and fine). This will be followed by a comparison of phase composition of these three fractions by quantitative XRD.

The XRD pattern of the coarse fly ash (Figure 5.7) shows a relatively low amorphous hump, a portion of which arises from the amorphous carbon content (5.6

wt.%). Quartz peaks dominate the pattern with small amounts of hematite, maghemite, magnetite and mullite.

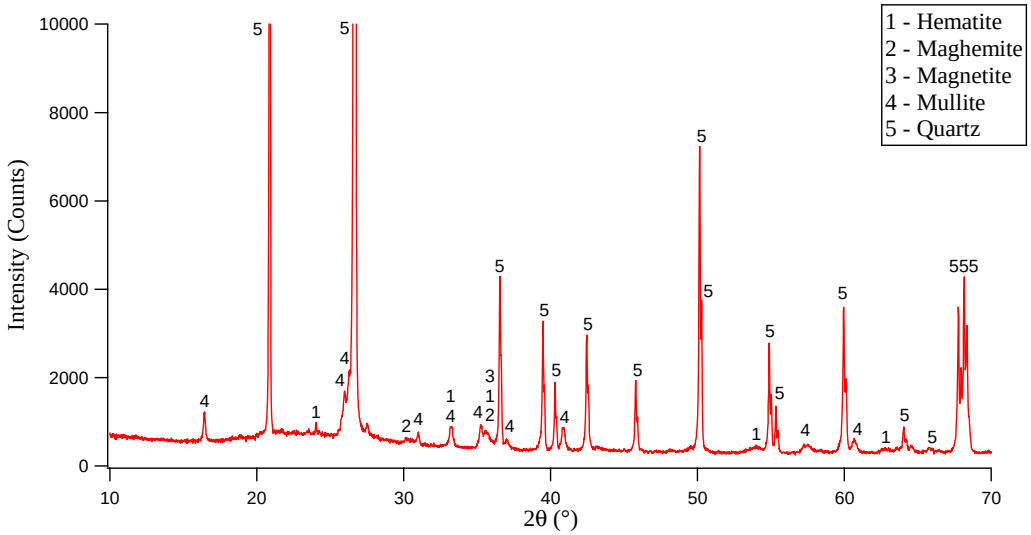

Figure 5.7: XRD pattern of coarse fly ash. (Bruker D8 Advance)

Instances of large fly ash spheres with many irregular shaped particles are apparent in the coarse fraction (Figure 5.8). The fly ash spheres contain only meagre amount of amorphous material binding the crystalline phases together as seen in a cross sectioned view of the coarse particles (Figure 5.9).

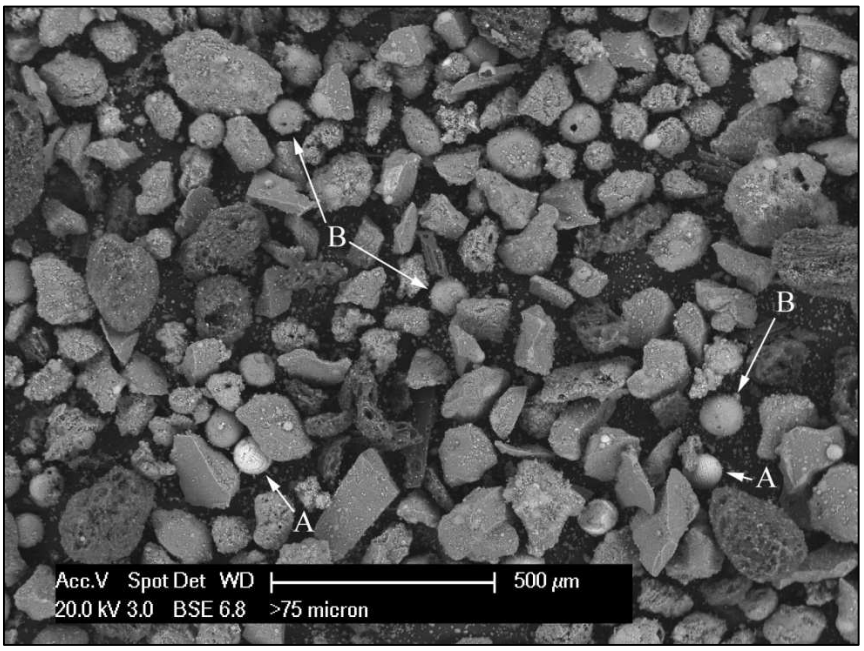

Figure 5.8: A backscattered electron image of coarse fly ash where (A) are fly ash spheres with iron oxide encapsulated and (B) are fly ash spheres with mullite and quartz encapsulated. (Philips XL30)

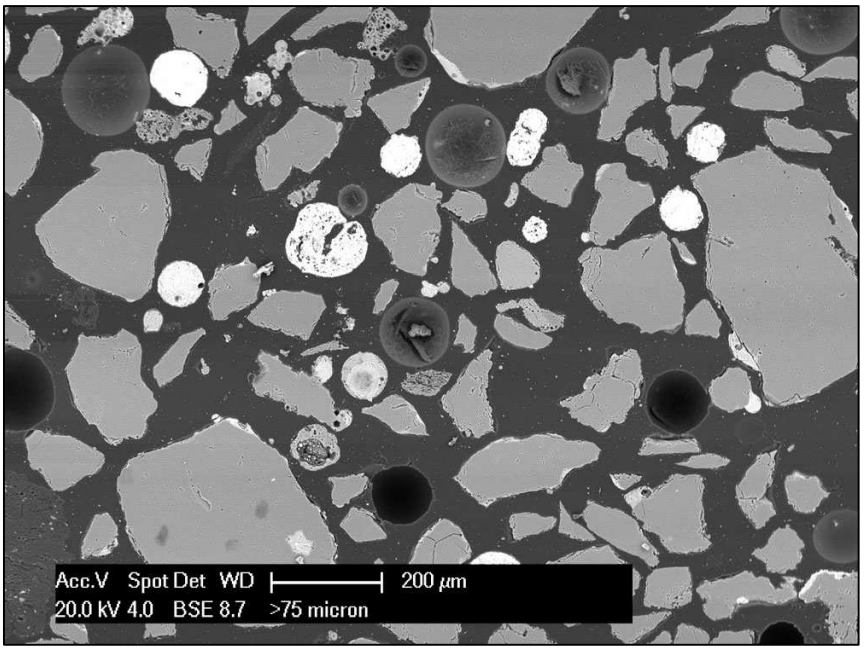

Figure 5.9: A backscattered electron image of cross sectioned coarse fly ash showing the larger quartz particles intermingled with spherical and irregular fly ash particles primarily consisting of iron oxide and mullite crystals. (Philips XL30)

The irregularly shaped particles seen in Figure 5.10 were observed to trap smaller spherical fly ash particles on their coarse surfaces (Figure 5.10). The smaller particles are classical fly ash spheres consisting of crystalline phases (iron oxides, mullite and quartz) encapsulated by amorphous material. Figure 5.10 gives an indication at the large amount of these smaller spheres that may be trapped by the irregularly shaped particles.

Amorphous carbon particles are visually prolific in the coarse fly ash (Figure 5.5B). When viewed using a SEM, the irregular shaped porous carbon particles can be observed to have a range of dimensions (Figure 5.11). The porous nature of the amorphous carbon particles has the potential to adsorb liquids resulting in a need for higher liquids:solids to produce a workable slurry. In addition the presence of carbon is known to result in a decrease in compressive strength (Shi *et al.* 2006).

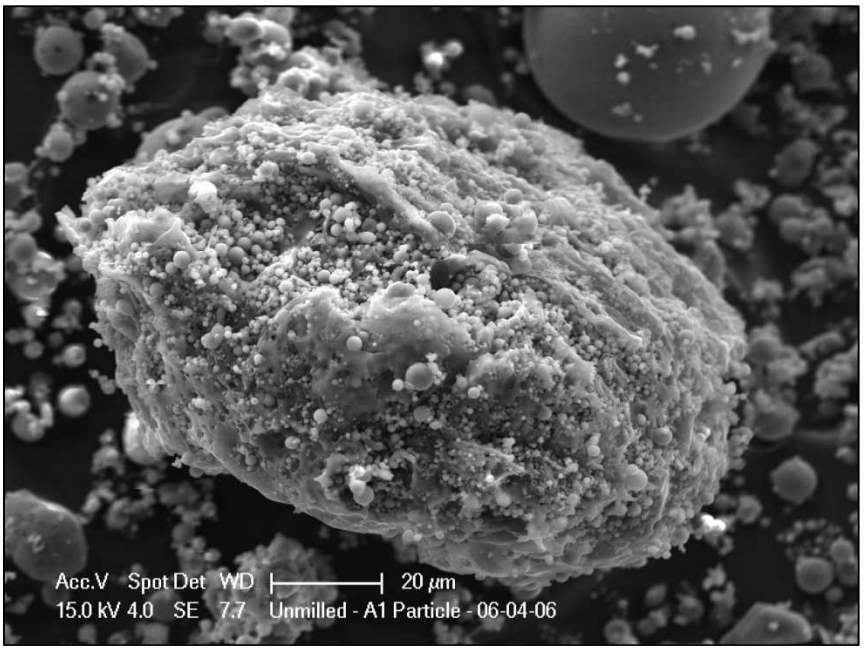

Figure 5.10: A secondary electron image of an irregular shaped particle with smaller fly ash spheres trapped or fused upon its rough surface. (Philips XL30)

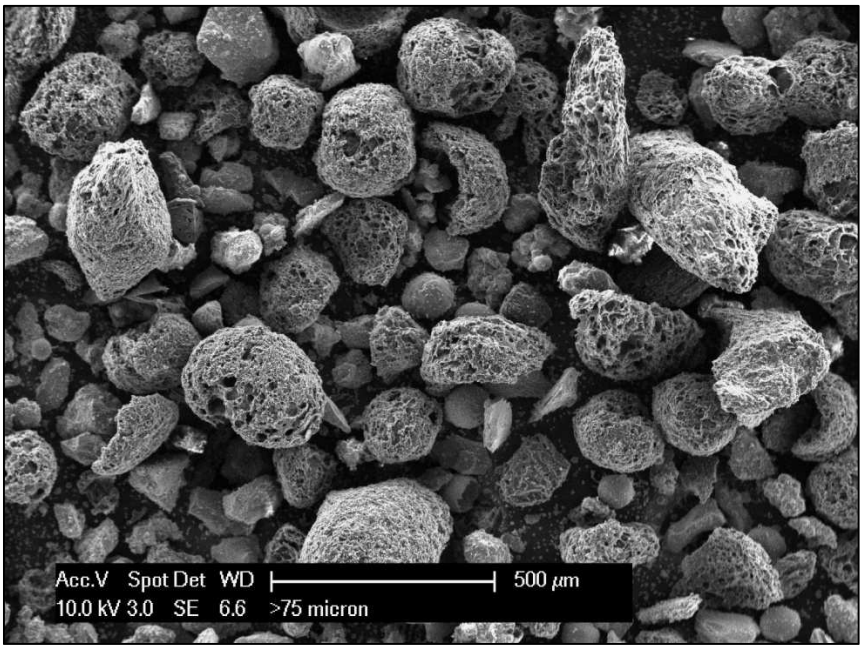

Figure 5.11: A secondary electron image of coarse fly ash showing porous carbon particles with a variety of sizes and shapes. (Philips XL30)

In medium fly ash, the primary phase is quartz along with hematite, maghemite, magnetite and mullite. There is a moderate amount of amorphous material visible in this size fraction as depicted by the characteristic diffuse hump at approximately 15 ° to 30 ° 2θ (Figure 5.12).

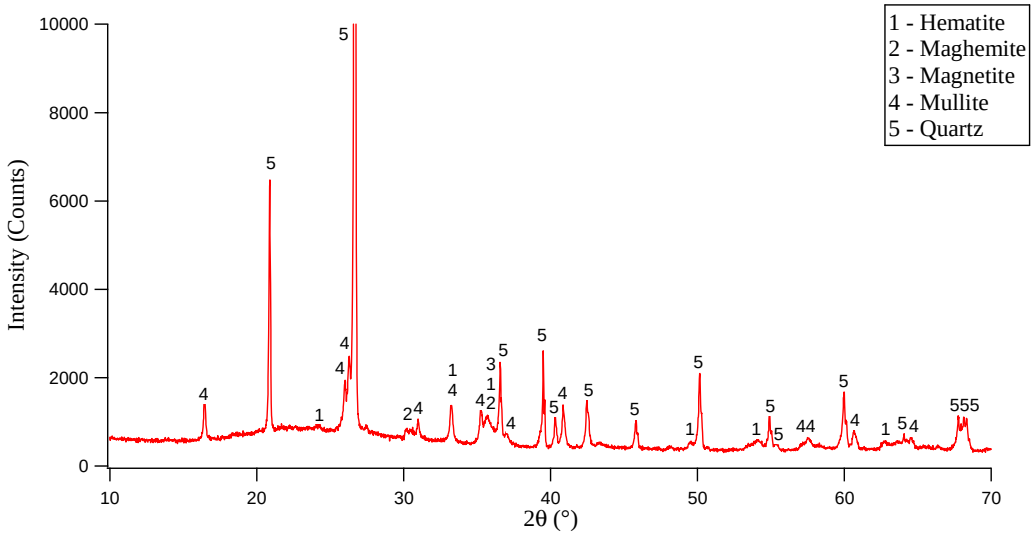

Figure 5.12: XRD pattern of medium fly ash. (Bruker D8 Advance)

Amorphous carbon particles were identified using SEM imaging (Figure 5.13). These particles were seen to be in two distinct forms, rod-like particles or irregular shaped particles versus predominantly irregular particles found in the coarse fly ash. The particle morphologies observed suggests that they are fragments of larger particles.

Fine fly ash contains hematite, maghemite, magnetite, mullite and quartz (Figure 5.14). The majority of amorphous material present in Collie fly ash is found within this size fraction.

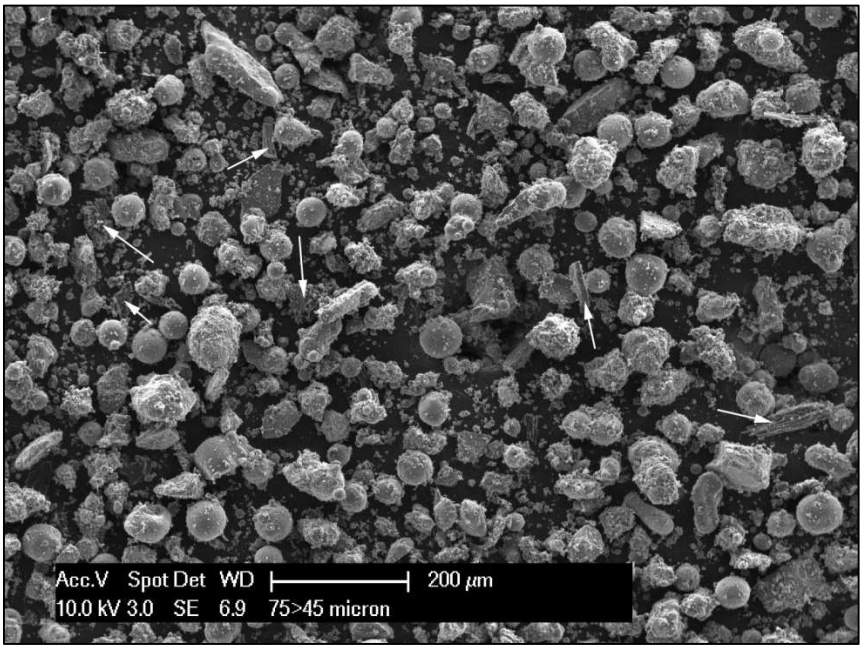

Figure 5.13: A secondary electron image of the medium fraction where arrows indicate carbon particles. (Philips XL30)

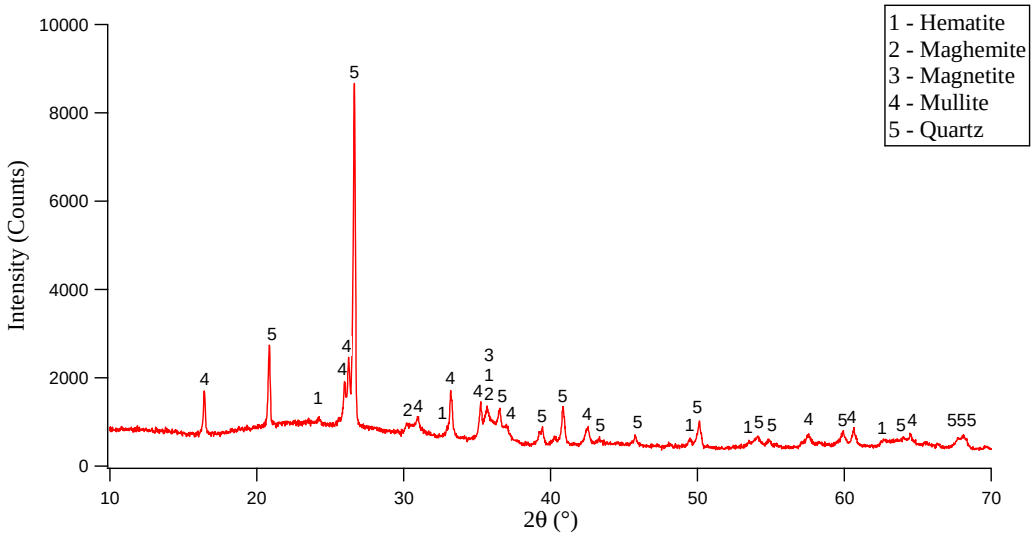

Figure 5.14: XRD pattern of fine fly ash. (Bruker D8 Advance)

Rietveld refinement with XRD data was utilised to determine the abundance of the phases found within the three size fractions (Table 5.3).

Table 5.3: Quantitative XRD phase analysis of the different size ranges of Collie fly ash.

Phase	Coarse fraction (wt.%)	Medium fraction (wt.%)	Fine fraction (wt.%)
Amorphous	13.00 ± 3.96	30.61 ± 1.25	58.63 ± 0.79
Hematite	0.61 ± 0.01	1.89 ± 0.06	1.82 ± 0.06
Maghemite	1.67 ± 0.03	3.97 ± 0.10	3.68 ± 0.12
Magnetite	1.42 ± 0.12	3.95 ± 0.03	2.33 ± 0.04
Mullite	9.38 ± 0.27	18.24 ± 0.33	17.15 ± 0.30
Quartz (Primary)	39.75 ± 2.21	25.13 ± 0.86	7.27 ± 0.22
Quartz (Secondary)	34.20 ± 1.36	16.21 ± 0.72	9.11 ± 0.52

The values shown in Table 5.3 in conjunction with LOI results (Table 5.2) agree with SEM imaging and qualitative XRD observations. Observations showed:

1. Activated carbon existed primarily as an isolated phase
2. Quartz in coarse and medium sized range of fly ash was predominantly isolated from other phases
3. Quartz in fine size range was typically found encapsulated with other phases in conjunction with amorphous aluminosilicate
4. The majority of fly ash spheres were < 75 µm.
5. The majority of amorphous aluminosilicate exists in the fine fraction (< 45 µm)

In order to accurately fit the quartz peaks using Rietveld refinement, two quartz phases were included in the refinement process. One quartz profile was utilised to represent the original quartz (primary quartz) present with the coal. The other quartz profile represented quartz which formed during the combustion process which has the tendency to contain Al, Fe, Na or Ti substitution for Si. During the coal combustion, pulverised coal passes briefly through the high temperature zone. Kaolin present in the coal undergoes dehydroxlation to metakaolin (400 – 600 ºC) and recrystallisation to a defect alumina silica spinel with free silica (~ 950 ºC). Further calcination causes the spinel to transform to mullite with further release of crystalline silica (Drzal *et al.* 1983 and Mayoral *et al.* 2001). Due to the brief period in the high temperature zone, incomplete crystallisation occurs leading to the formation of the fly ash spheres with entrapped mullite, iron oxides and quartz.

It can be assumed that a significant proportion of clay in coal converts to metakaolin, which will proceed to the formation of mullite and secondary quartz via:

$$3(Al_2O_3.2SiO_2) \rightarrow 3Al_2O_3.2SiO_2 + 4SiO_2 \quad (5.1)$$

One hypothesis might be that the larger spheres cool more slowly and thus provide better conditions for the conversion of metakaolin to mullite and secondary quartz. In Table 5.3 it is noted that the secondary quartz is present in the coarse fraction at 34.20 wt.% and amorphous content (partly metakaolin) is low. Also the

ratio of mullite to secondary quartz in the above equation is 1:4 which is close to that measured (9.38:34.20). It should be noted that primary quartz can also be encapsulated in the larger spheres (Figure 4.6).

For the fine fraction there is less overall conversion of metakaolin to mullite and secondary quartz. This suggests that rapid cooling may have prevented the formation of additional secondary quartz, leaving the SiO_2 in an amorphous state.

Although time constraints prevented the above hypothesis from being verified, it is clear that this is an important and complex aspect of ash chemistry that deserves further investigation.

Isolated particles of activated carbon and quartz dominated the coarse size fraction. Both primary and secondary quartz were abundant at 39.75 wt.% and 34.20 wt.% respectively. Only a relatively small amount (7.41 wt.%) of amorphous material (Al, Si, Fe oxides) was present in this size fraction along with 5.59 wt.% amorphous carbon. Crystalline iron oxides and mullite were present at 13.08 wt.%. With a low amorphous content compared to the iron oxides/mullite material, fly ash particles of coarse size are primarily inert crystalline material and not suitable as a source material for geopolymerisation.

In the medium size range the most abundant phase is quartz at 41.34 wt.% followed by amorphous material at 29.25 wt.%, iron oxides/mullite at 28.05 wt.% and activated carbon at 1.36 wt.%. Quartz is still predominantly found as isolated particles while smaller secondary quartz is found within amorphous material with other crystalline phases. Primary quartz was marginally more abundant at 25.13 wt.% compared with secondary quartz at 16.21 wt.%. The medium size range has 240 % more amorphous material than the coarse size range which is a dramatic improvement for geopolymerisation.

Amorphous material is the most abundant phase in the fine size range at 56.92 wt.%. Secondary quartz is now the dominant quartz phase at 9.11 wt.% with primary quartz at 7.27 wt.%. The combined weight of crystalline iron oxides/mullite was a substantial 24.98 wt.% which leads to an amorphous material to iron

oxides/mullite ratio of 2.3. This indicates a trend where smaller fly ash particles contain a larger concentration of amorphous material, possibly due the smaller fly ash particles being cooled too rapidly for crystallisation into iron oxides or mullite.

A comparison of unmodified Collie fly ash to fine fly ash (Table 5.4) shows sieving has removed 25 % quartz. The dominant quartz phase has shifted from being primary quartz to secondary quartz as the overall particle size has decreased. The removal of the larger particles slightly increased the overall amorphous content.

Comparison of XRF data for unmodified Collie fly ash and the fine Collie fly ash (Table 5.5) confirms the decrease of SiO_2 via the removal of large primary quartz particles leaving the small secondary quartz embedded in fly ash spheres. There is a subsequent marginal increase of the other elemental oxide phases to balance the decrease in SiO_2. Although there is a 5 % decrease in quartz (XRD), the 3 % decrease in SiO_2 content determined by XRF indicates the level of Si found in the amorphous material.

By combining results from XRF and XRD the elemental weight percentage of the amorphous was calculated (Table 5.6). The amorphous Si:Al molar ratio was marginally reduced by sieving. What is clearly evident is that sieving removes some amorphous carbon but essentially has little impact on the amorphous Al:Si: Fe. This is a desirable outcome if the beneficiation process is to be efficient.

Table 5.4: Comparison of QXRD and LOI (carbon) values for unmodified fly ash and fine fly ash.

Phase	Unmodified Fly Ash (wt.%)	Fine Fly Ash (wt.%)
Amorphous	54.58 ± 1.03	58.63 ± 0.79
Hematite	1.64 ± 0.03	1.82 ± 0.06
Maghemite	3.45 ± 0.10	3.68 ± 0.12
Magnetite	2.33 ± 0.10	2.33 ± 0.04
Mullite	16.2 ± 0.15	17.15 ± 0.30
Quartz (Primary)	12.16 ± 0.71	7.27 ± 0.22
Quartz (Secondary)	9.65 ± 0.33	9.11 ± 0.52
Carbon	2.06 ± 0.01	1.71 ± 0.03

Table 5.5: Comparison of elemental oxide composition (XRF) for unmodified fly ash and fine fly ash.

Elemental Oxide	Unmodified (wt.%)	Fine (wt.%)
SiO_2	51.46 ± 0.23	48.23 ± 0.06
Al_2O_3	23.59 ± 0.21	25.43 ± 0.06
CaO	1.75 ± 0.01	1.89 ± 0.01
Fe_2O_3	15.33 ± 0.08	16.00 ± 0.01
K_2O	0.84 ± 0.01	0.84 ± 0.01
MgO	1.15 ± 0.01	1.32 ± 0.01
Na_2O	0.36 ± 0.01	0.44 ± 0.01
P_2O_5	1.32 ± 0.01	1.41 ± 0.01
SO_3	0.27 ± 0.01	0.34 ± 0.01
TiO_2	1.31 ± 0.01	1.37 ± 0.01

Table 5.6: Comparison of Al, Fe and Si in amorphous content for unmodified fly ash and fine fly ash.

Element	Unmodified (wt.%)	Fine (wt.%)
Al	6.11 ± 0.06	6.71 ± 0.12
Si	11.92 ± 0.37	12.83 ± 0.18
Fe	5.48 ± 0.16	5.66 ± 0.13
Si:Al (Molar)	1.88	1.84

The reactivity of the fly ash is also dependent on the surface area of the particles with a larger surface area leading to a higher rate of reaction. The surface area determined by BET analysis of unmodified fly ash is 9.83 ± 0.21 m^2/g which is higher than the value for fine fly ash of 7.84 ± 0.16 m^2/g. This result is believed to be due to the presence of amorphous carbon particles (Figure 5.8) with individually large surface area in the unmodified fly ash.

The dissolution rate was compared between unmodified fly ash and fine fly ash. Figure 5.15 shows that there is minimal change in dissolution rate between the fly ashes until approximately 90 minutes has elapsed. After this the fine fly ash displays increased consumption owing to the smaller sized crystalline phases which are more readily dissolved compared to the large crystalline phases found in unmodified fly ash. It must be understood that during the dissolution experiment the powders are saturated in highly concentrated NaOH solution which does not represent the typical production method for geopolymer where limited alkaline activating solution is utilised.

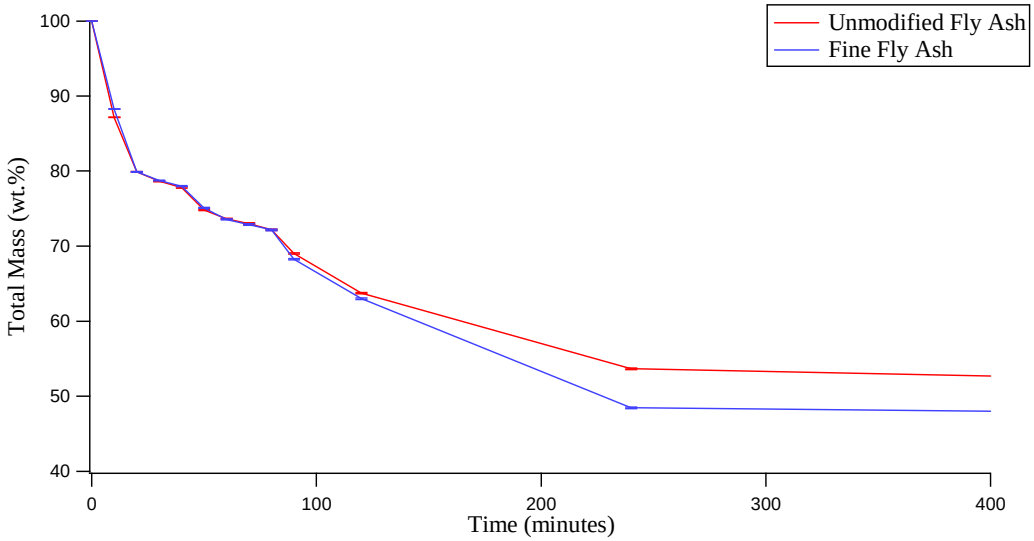

Figure 5.15: Mass loss comparison of dissolution solid residues from unmodified fly ash and fine fly ash. Dissolution was conducted using 14 M NaOH solution at 75 °C.

The results presented above show there are potential benefits in removing particles greater than 45 µm thereby mainly reducing carbon and primary quartz. With the reduction in secondary phases, there will be a higher proportion of reactive material available to the alkaline solution and less filler material to cause heterogeneity of the geopolymer. Removal of carbon content also ensures correct elemental ratios as it won't adsorb part of the alkaline activator solution thereby reducing the overall dissolution potential of the system. This extra effort to beneficiate the fly ash can only be justified for specialised applications such as the manufacture of ceramics and fire resistant products.

5.2.3 Magnetic Separation

It was stated in Section 5.2 that the iron oxide phases are impossible to remove from the vitreous aluminosilicate material without chemical treatment. This is due to the intimate and fine intermingling of all the constituents in the fine fly ash spheres.

Chemical removal of the crystalline iron oxide phases was trialled using the DCB extraction technique (dithionite citrate bicarbonate) utilised in soil science (Singer *et al.* 1995, van Oorschot & Dekkers 1999, Hart *et al.* 2002). This approach lead to removal of approximately 11 wt.% iron oxide observed by inductively coupled plasma mass spectrometry (ICP-MS) of the liquid residue and confirmed by XRD. However the chemical alteration of the overall bulk content was deemed too severe for practical utilisation. Other factors that must be taken into consideration are the additional costs in both carbon credits and monetary value.

The crystalline iron oxide phases of hematite, maghemite and magnetite (Fe = 5.24 wt.%) were identified as components of Collie fly ash from XRD results. However a significant amount of amorphous iron oxide (Fe = 5.48 wt.%) was also identified (Section 4.3). The dissolution experiment described in Section 4.4 confirmed the majority of the crystalline iron oxide being encapsulated by the vitreous content of the fly ash. Hematite is weakly ferromagnetic at room temperature while maghemite and magnetite are ferrimagnetic at room temperature. Therefore it is possible, in principle, to remove these phases using magnetic separation. There is not enough known about the amorphous iron oxide to know in advance if it was magnetic. Dry magnetic separation was initially trialled however it was found to be inadequate due to severe agglomeration. As a result wet magnetic separation was utilised to de-agglomerate the particles before separation.

Wet magnetic separation of unmodified fly ash (UFA) resulted in the removal of 30.37 ± 0.61 wt.% from the bulk material. This is about twice the amount of iron oxide in the fly ash and clearly shows that other phases coexist with the iron oxides and are removed at the same time. Particle sizing indicates that the magnetic iron oxide phases are primarily found in the larger diameter fly ash particles. Visual

inspection of the magnetic material (MAG-UFA) shows it to be a dark brown/gray hue (Figure 5.16 B) whilst the residual non-magnetic materials (NM-UFA) are of a lighter brown hue (Figure 5.16 A).

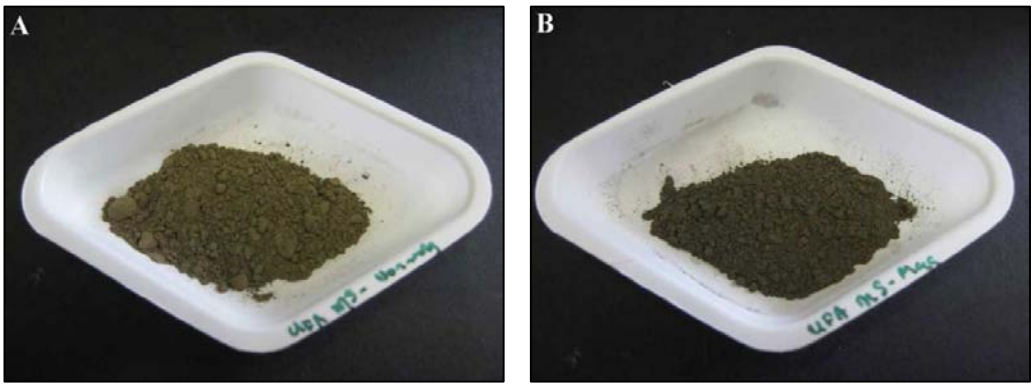

Figure 5.16: Magnetically separated Collie fly ash: (A) NM-UFA and (B) MAG-UFA.

XRF results (Table 5.7) indicate a 36 % reduction in iron oxide is possible through magnetic separation albeit with removal of amorphous material as well. QXRD results (Table 5.8) indicates that the crystalline iron oxide was lowered by 71 %. The residual 9.8 wt.% Fe_2O_3 in NM-UFA is made up of 2.2 wt.% crystalline iron oxide and 7.6 wt.% non-magnetic iron oxide believed to be amorphous or poorly ordered. The residual crystalline iron oxide is believed to be finely dispersed and difficult to remove without extensive processing. A 13 wt.% reduction in SiO_2 with a 2 wt.% reduction in Al_2O_3 was noticed in the magnetic portion of UFA. This indicates that only a small amount of quartz is associated with MAG-SFA.

Table 5.7: Comparison of elemental oxide composition (XRF) for UFA, MAG-UFA and NM-UFA.

Elemental Oxide	UFA (wt.%)	MAG-UFA (wt.%)	NM-UFA (wt.%)
SiO_2	51.46 ± 0.23	38.4 ± 0.05	56.27 ± 0.12
Al_2O_3	23.59 ± 0.21	21.5 ± 0.01	26.30 ± 0.01
CaO	1.75 ± 0.01	2.57 ± 0.01	1.43 ± 0.01
Fe_2O_3	15.33 ± 0.08	33.1 ± 0.01	9.81 ± 0.02
K_2O	0.84 ± 0.01	0.53 ± 0.01	0.99 ± 0.01
MgO	1.15 ± 0.01	1.73 ± 0.01	1.07 ± 0.01
Na_2O	0.36 ± 0.01	0.38 ± 0.01	0.48 ± 0.01
P_2O_5	1.32 ± 0.01	1.92 ± 0.01	1.16 ± 0.01
SO_3	0.27 ± 0.01	0.04 ± 0.01	0.02 ± 0.01
TiO_2	1.31 ± 0.01	1.27 ± 0.01	1.41 ± 0.01

Table 5.8: Comparison of QXRD values for UFA and NM-UFA.

Phase	Unmodified (wt.%)	Non-magnetic (wt.%)
Amorphous	54.58 ± 1.03	53.28 ± 0.51
Hematite	1.64 ± 0.03	0.68 ± 0.04
Maghemite	3.45 ± 0.10	1.10 ± 0.20
Magnetite	2.33 ± 0.10	0.39 ± 0.10
Mullite	16.20 ± 0.15	19.86 ± 0.18
Quartz (Primary)	12.16 ± 0.71	13.57 ± 0.28
Quartz (Secondary)	9.65 ± 0.33	11.12 ± 0.10

A comparison of QXRD results for UFA and NM-UFA show that the amorphous content is unchanged though there is an increase in mullite and quartz and a reduction in crystalline iron oxide. The molar Si:Al ratio of the amorphous content of NM-UFA was determined to be 1.95 which is marginally higher than that of the UFA value of 1.88 (Table 5.9).

Table 5.9: Comparison of Al, Fe and Si in amorphous content for UFA and NM-UFA.

Element	UFA (wt.%)	NM-UFA (wt.%)
Al	6.11 ± 0.06	6.10 ± 0.07
Si	11.92 ± 0.37	12.38 ± 0.11
Fe	5.48 ± 0.16	5.33 ± 0.17
Si:Al (Molar)	1.88	1.95

Figure 5.17 shows the size distribution and morphology for the magnetically removed fraction. Not all particles in Figure 5.17 appear bright which arises when particles are a mixture of iron oxide and other phases of lower atomic number. From Figure 5.18 it is clear that some particles are almost solid iron oxide spheres while others have finely dispersed (dendritic) iron oxide.

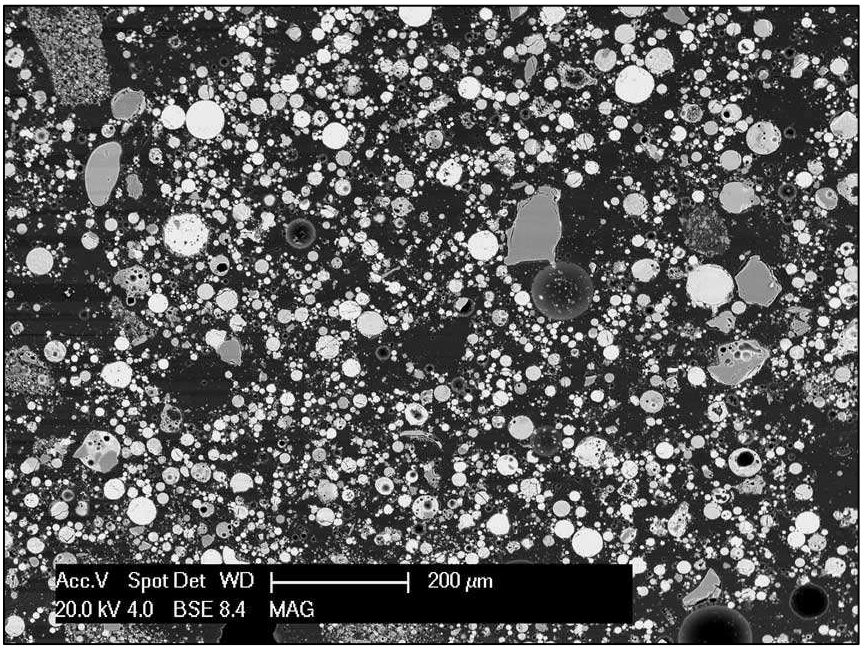

Figure 5.17: A backscattered electron image demonstrating the varying morphology and size of NM-UFA. (Philips XL30)

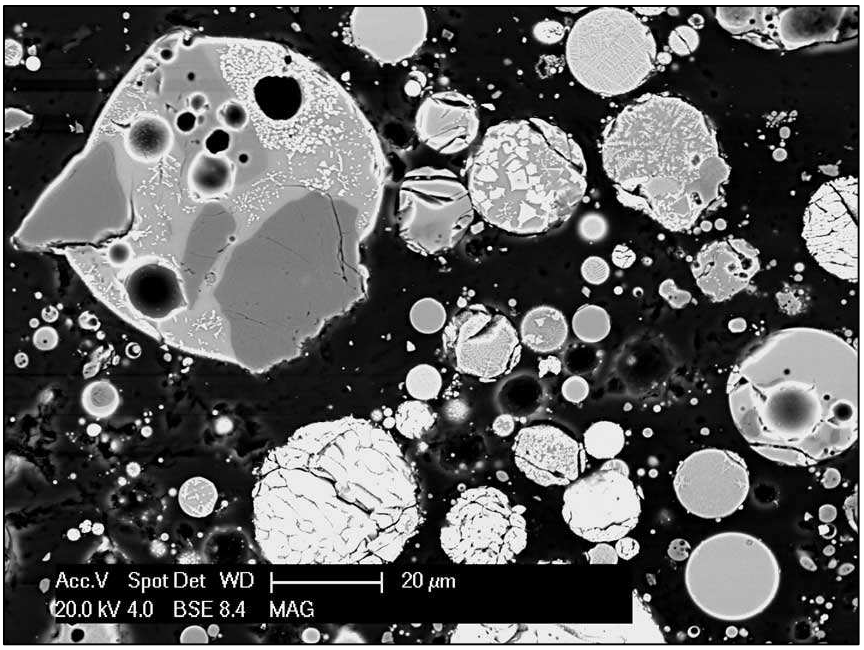

Figure 5.18: A backscattered electron image showing the heterogeneity of the individual magnetic iron rich fly ash particles where bright particles are crystalline iron oxide phases, dark grey particles are quartz and lighter grey areas represent vitreous aluminosilicate material. (Philips XL30)

Removal of particles rich in crystalline iron oxide also resulted in a significant increase in surface area. BET results showed a 34% increase in surface area of NM-UFA (13.14 m^2/g) compared with the unmodified fly ash (9.83 m^2/g). In Section 5.2.2 it was shown that a moderate amount of crystalline iron oxide was found as large particles. With the removal of these larger particles, the smaller particles would be dominant leading to an increase in overall surface area. This suggests that the non-magnetic fly ash would be more reactive during the alkali dissolution process.

Wet magnetic separation of the fine fly ash (SFA) fraction removed 20.39 wt.% from the bulk material. The majority of the magnetic material was composed of larger particles as seen in Figure 5.19. This suggests that iron oxides underwent different cooling regimes according to fly ash particle size. Larger particles will cool at a slower rate allowing more time for the formation of crystalline iron oxides whilst the smaller particles cool at a faster rate thus preventing crystallisation and leaving amorphous iron oxide. Visual inspection of the material was similar to that of Figure 5.16 with the magnetically separated sample (MAG-SFA) being a darker brown/gray hue compared to the residual sample (NM-SFA).

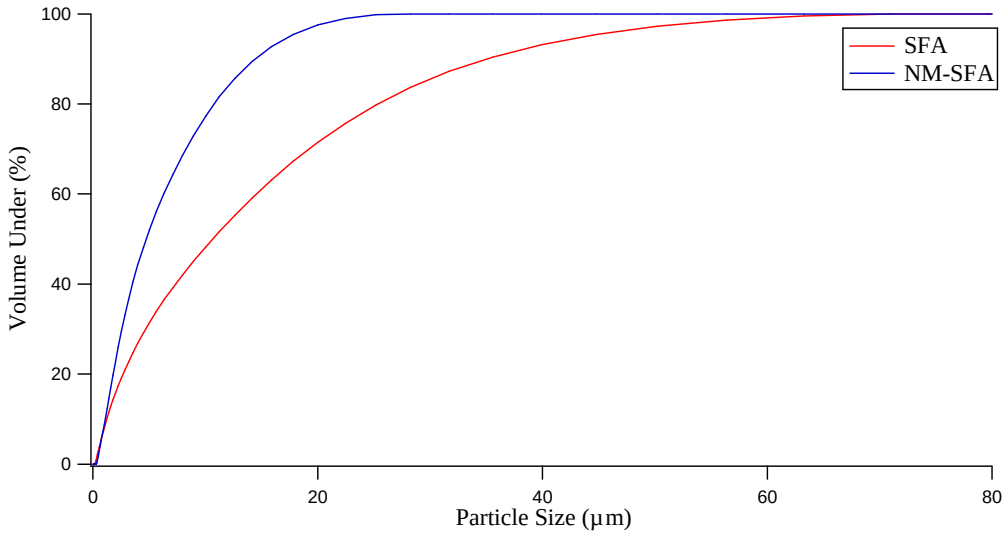

Figure 5.19: Comparison of particle size range of SFA and NM-SFA.

XRF results (Table 5.10) show that a 34 % reduction in iron oxide has been achieved by magnetically separating SFA. The major part of this reduction comes from a 72 % decrease in crystalline iron oxide (Table 5.11). The magnetically removed fraction is similar to the magnetically removed fraction removed from UFA. The amorphous molar Si:Al ratio of NM-SFA was determined to be 1.98, which is slightly higher than the 1.84 measured for SFA. The 10 % reduction in SiO_2 with 3 % reduction in Al_2O_3 indicate that only a small amount of quartz is associated with the magnetic portion of SFA.

Magnetic separation resulted in a 75 % increase in surface area from the SFA value of 7.84 m^2/g to the NM-SFA value of 13.69 m^2/g. This suggests that NM-SFA would be considerably more reactive during the alkali dissolution process due to the removal of the larger particles.

Removal of crystalline iron oxide has shown to be effective and provides the unanticipated benefit of significantly increasing surface area. The combination of analysis techniques demonstrates an acceptable level of crystalline iron oxide removal from Collie fly ash. Though the end result is practically the same level of amorphous material, the crystalline iron oxide phases can be further processed to provide both iron oxide concentrate and zeolite (Dobbins & Burnet 1982).

Table 5.10: Comparison of elemental oxide composition (XRF) for SFA, MAG-SFA and NM-SFA.

Elemental Oxide	SFA (wt.%)	MAG-SFA (wt.%)	NM-SFA(wt.%)
SiO_2	48.23 ± 0.06	38.00 ± 0.05	52.80 ± 0.08
Al_2O_3	25.43 ± 0.06	22.30 ± 0.04	27.20 ± 0.03
CaO	1.89 ± 0.01	2.60 ± 0.01	1.49 ± 0.01
Fe_2O_3	16.00 ± 0.01	29.50 ± 0.01	10.50 ± 0.01
K_2O	0.84 ± 0.01	0.56 ± 0.01	0.96 ± 0.01
MgO	1.32 ± 0.01	1.70 ± 0.01	1.10 ± 0.01
Na_2O	0.44 ± 0.01	0.29 ± 0.01	0.41 ± 0.01
P_2O_5	1.41 ± 0.01	1.93 ± 0.01	1.25 ± 0.01
SO_3	0.34 ± 0.01	0.13 ± 0.01	0.17 ± 0.01
TiO_2	1.37 ± 0.01	1.32 ± 0.01	1.43 ± 0.01

Table 5.11: Comparison of QXRD values for SFA and NM-SFA.

Phase	SFA (wt.%)	NM-SFA (wt.%)
Amorphous	58.63 ± 0.79	57.00 ± 2.11
Hematite	1.82 ± 0.06	0.75 ± 0.06
Maghemite	3.68 ± 0.12	1.00 ± 0.07
Magnetite	2.33 ± 0.04	0.42 ± 0.04
Mullite	17.15 ± 0.30	20.74 ± 0.80
Quartz (Primary)	7.27 ± 0.22	9.70 ± 0.53
Quartz (Secondary)	9.11 ± 0.52	10.38 ± 0.69

5.3 Milling of Fly Ash

Dissolution results from Section 4.4 showed that the consumption of the amorphous content is a time based process. As the majority of fly ash particles are intermixed with amorphous and crystalline content, complete consumption of the reactive amorphous content by the alkaline solution is not likely. Milling of the fly

ash was thus investigated to determine if exposing the internal amorphous content by fracturing fly ash spheres and at the same time increasing particle surface area would improve the total dissolution by the alkali.

Figure 5.20 shows that milling has dramatically reduced particle size when compared with UFA and SFA. Approximately 80 % of milled particles (MFA) are below 10 µm in size showing that the milling process has been successful for improved liberation of the vitreous content. SEM images support the results from the laser sizing (Figure 5.21).

The fractured spheres shown in Figure 5.21 reveals the change in particle shape from primary spherical particles to irregularly shaped fragments. Payá *et al.* (1996) states that changes to particle shape from grinding will detrimentally affect the particle packing factor and workability. However, if the exposure of internal amorphous content increases total dissolution and thus increases geopolymer gel formation, the effect of the irregular shapes will be lessened.

MFA (Figure 5.22) was found to exhibit a considerable increase in agglomeration of the particles when compared with UFA.

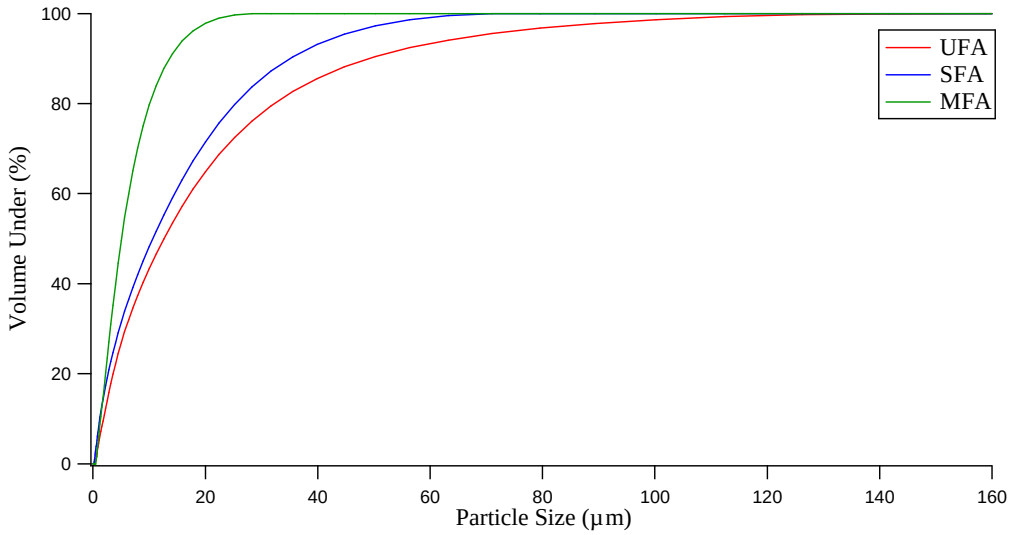

Figure 5.20: Comparison of particle size of UFA, SFA and MFA.

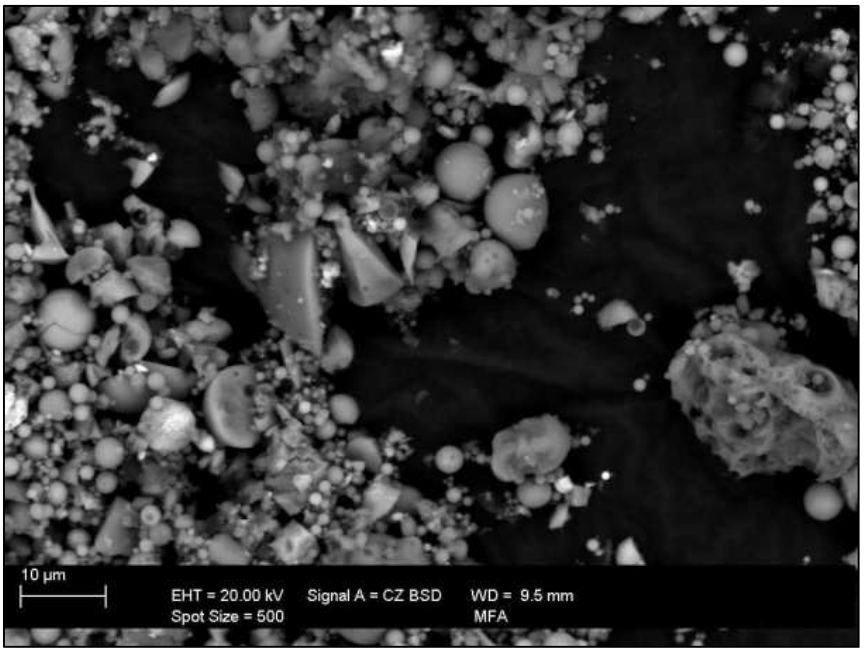

Figure 5.21: Secondary electron images of MFA. (Zeiss EVO)

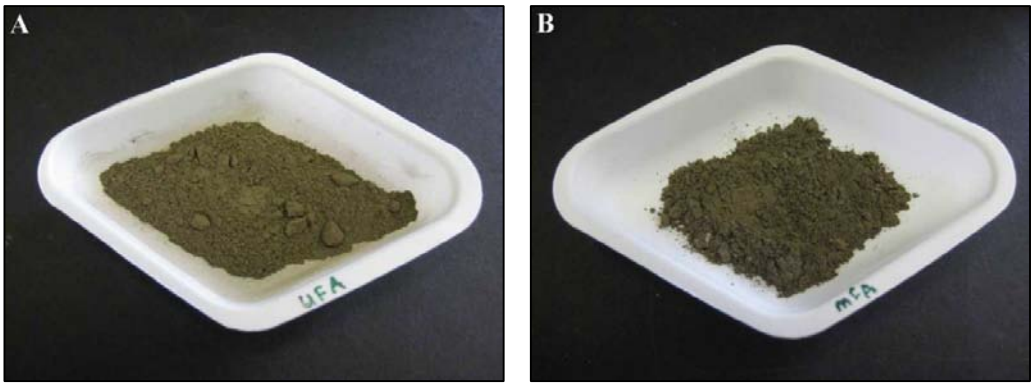

Figure 5.22: Comparison of Collie fly ash: (A) UFA and (B) MFA.

XRF (Table 5.12) in conjunction with QXRD (Table 5.13) shows that milling has resulted in a minor increase in amorphous content relative to unmodified fly ash. MFA has a Si:Al of 1.87 for the amorphous component compared to 1.84 for SFA.

Table 5.12: Comparison of elemental oxide composition (XRF) for UFA and MFA.

Elemental Oxide	UFA (wt.%)	MFA (wt.%)
SiO_2	51.46 ± 0.23	48.03 ± 0.12
Al_2O_3	23.59 ± 0.21	25.47 ± 0.12
CaO	1.75 ± 0.01	1.89 ± 0.01
Fe_2O_3	15.33 ± 0.08	16.00 ± 0.01
K_2O	0.84 ± 0.01	0.84 ± 0.01
MgO	1.15 ± 0.01	1.31 ± 0.01
Na_2O	0.36 ± 0.01	0.45 ± 0.01
P_2O_5	1.32 ± 0.01	1.41 ± 0.01
SO_3	0.27 ± 0.01	0.34 ± 0.01
TiO_2	1.31 ± 0.01	1.36 ± 0.01
MnO	0.13 ± 0.01	0.14 ± 0.01
Others	2.50 ± 0.60	2.76 ± 0.33

Table 5.13: Comparison of QXRD values for UFA and MFA.

Phase	UFA (wt.%)	MFA (wt.%)
Amorphous	54.58 ± 1.03	60.15 ± 0.47
Hematite	1.64 ± 0.03	1.94 ± 0.05
Maghemite	3.45 ± 0.10	3.61 ± 0.17
Magnetite	2.33 ± 0.10	2.37 ± 0.10
Mullite	16.2 ± 0.15	16.81 ± 0.17
Quartz (Primary)	12.16 ± 0.71	7.42 ± 0.22
Quartz (Secondary)	9.65 ± 0.33	7.68 ± 0.17

Even though the results for the MFA thus far are similar to those for the SFA precursor, there is a 36 % increase in surface area from 7.84 ± 0.16 m^2/g to 10.68 ± 0.23 m^2/g with an anticipated concomitant increase in reactivity.

The reactivity of MFA was compared to UFA by a dissolution experiment (Figure 5.23). As anticipated, MFA dissolved considerably quicker than UFA. The mass loss difference between the two samples continued to increase up to 60 minutes. Beyond this point, the rate of dissolution for MFA decreased rapidly suggesting most of the available vitreous aluminosilicate has been consumed.

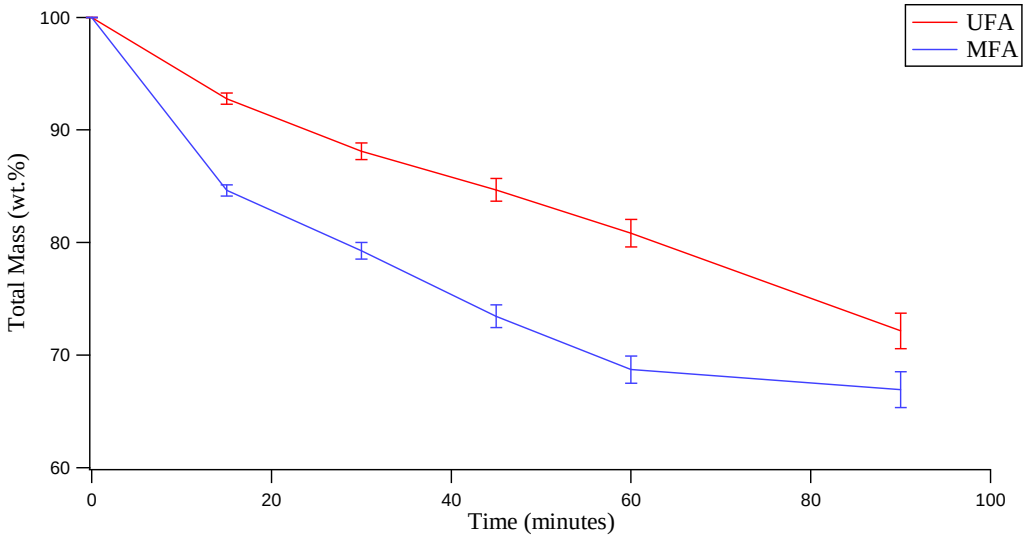

Figure 5.23: Comparison of mass loss for UFA and MFA after dissolution in 14 M NaOH solution at 75 °C.

The significant increase in the rate of dissolution for MFA suggests that products can be manufactured with increased geopolymer binder leading to improved strength and homogeneity.

5.3.1 Magnetic Separation of Sieved and Milled Fly Ash

The approach up until now has been to remove inert phases by sieving and to increase surface area by milling. The final beneficiation step was removal of the magnetic component from MFA. Wet magnetic separation was conducted on MFA leading to enrichment of the proportion of reactive component available for geopolymerisation.

The particle size (Figure 5.24) of the non-magnetic milled fly ash showed that the majority of particles were less than 8 µm, less than the particle size of the MFA. Visual inspection of the fly ash shows again that the magnetic content (MAG-MFA)

tended towards a dark brown/gray hue (Figure 5.25A) while the non-magnetic content (NM-MFA) was a lighter brown hue (Figure 5.25B).

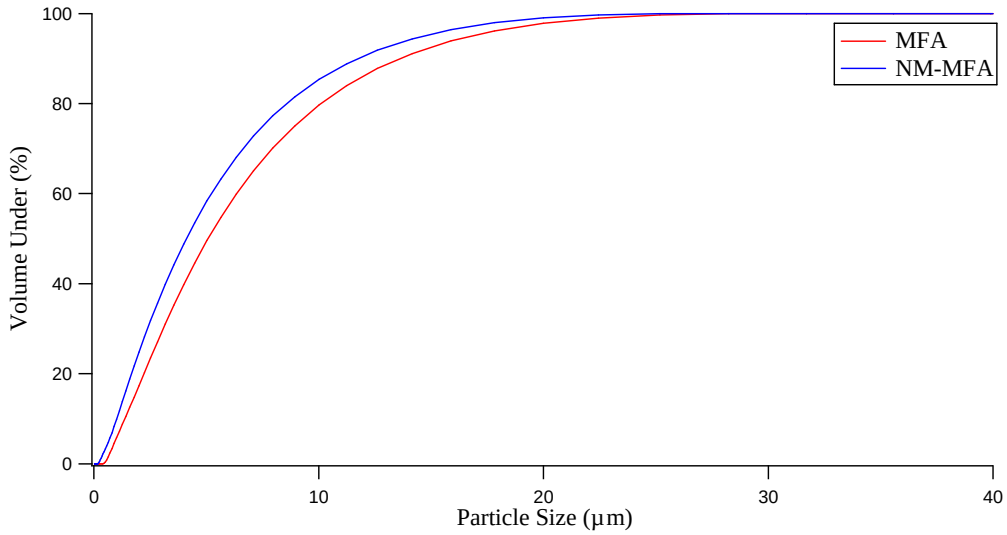

Figure 5.24: Comparison of particle size of MFA and NM-MFA.

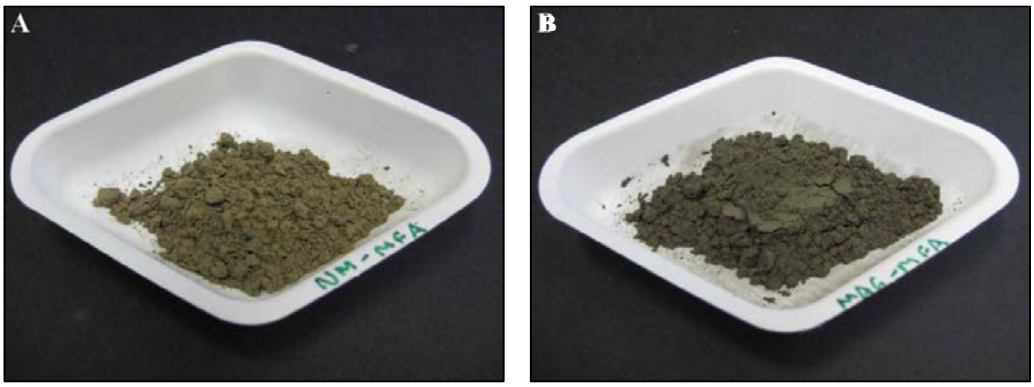

Figure 5.25: Comparison of Collie fly ash: (A) NM-MFA and (B) MAG-MFA.

XRF and QXRD results for MAG-MFA and NM-MFA (Table 5.14 and Table 5.15) show a similar trend to that observed for the magnetic removal of iron oxide from the UFA and SFA. Sixty one percent of crystalline iron oxide was removed from MFA by magnetic separation. The fact that approximately 40 % of the crystalline magnetic material remains in the 'non-magnetic' fraction can be attributed to the inherent weakness of the manual separation method as well as the co-existence of the magnetic and non-magnetic material. NM-MFA amorphous component was found to have a molar Si:Al ratio of 1.96.

Table 5.14: Comparison of elemental oxide composition (XRF) for MFA, MAG-MFA and NM-MFA.

Elemental Oxide	MFA (wt.%)	MAG-MFA (wt.%)	NM-MFA (wt.%)
SiO_2	48.03 ± 0.06	38.40 ± 0.01	53.13 ± 0.06
Al_2O_3	25.47 ± 0.06	21.50 ± 0.01	27.30 ± 0.01
CaO	1.89 ± 0.01	2.57 ± 0.01	1.66 ± 0.01
Fe_2O_3	16.00 ± 0.00	30.20 ± 0.01	11.47 ± 0.06
K_2O	0.84 ± 0.01	0.55 ± 0.01	0.95 ± 0.01
MgO	1.31 ± 0.01	1.69 ± 0.01	1.20 ± 0.01
Na_2O	0.45 ± 0.00	0.37 ± 0.01	0.49 ± 0.01
P_2O_5	1.41 ± 0.01	1.88 ± 0.01	1.32 ± 0.01
SO_3	0.34 ± 0.01	0.04 ± 0.01	0.02 ± 0.01
TiO_2	1.36 ± 0.01	1.30 ± 0.01	1.46 ± 0.01
MnO	0.14 ± 0.01	0.13 ± 0.01	0.13 ± 0.01
Others	2.76 ± 0.21	0.96 ± 0.11	0.87 ± 0.21

Table 5.15: Comparison of QXRD values for MFA and NM-MFA.

Phase	MFA (wt.%)	NM-MFA (wt.%)
Amorphous	60.15 ± 0.47	60.10 ± 0.48
Hematite	1.94 ± 0.05	0.96 ± 0.04
Maghemite	3.61 ± 0.17	1.56 ± 0.22
Magnetite	2.37 ± 0.10	0.59 ± 0.12
Mullite	16.81 ± 0.17	19.01 ± 0.19
Quartz (Primary)	7.42 ± 0.22	9.15 ± 0.17
Quartz (Secondary)	7.68 ± 0.17	8.64 ± 0.27

Removal of the majority of crystalline magnetic component resulted in a 21 % increase of surface area from 10.68 ± 0.23 m^2/g to 12.90 ± 0.22 m^2/g. This suggests that the spheres containing crystalline iron oxides are more resistant to milling.

With the large increase in surface area via milling plus subsequent removal of iron, it is believed that the non-magnetic milled fly ash will provide maximum dissolution when exposed to alkali leading to a higher proportion of geopolymer binder in the paste.

5.4 Summary

Table 5.16: Summary of key properties for Collie and beneficiated fly ash.

	UFA	SFA	MFA	NM-UFA	NM-SFA	NM-MFA
Surface area (m^2/g)	9.83	7.84	10.68	13.14	13.69	12.90
Amorphous content (wt.%)	54.58	58.63	60.15	53.28	57.00	60.10
Amorphous Si:Al (Molar)	1.88	1.84	1.87	1.95	1.98	1.96

- Sieving to < 45 µm size leads to a noticeable reduction in quartz and carbon content.
- Milling shows a significant increase in surface area and potential reactivity of the fly ash.
- Removal of crystalline iron results in a dramatic reduction in particle size and increase in surface area for the non-magnetic fraction.
- The majority of amorphous carbon is present as very fine particles.
- Two quartz phases are present in the fly ash. Primary quartz which is present from the original coal and secondary quartz which is formed during coal combustion.

Chapter 6

Geopolymers from Beneficiated Fly Ash

6.1 Introduction

Geopolymer synthesis is achieved by mixing an alkaline activating solution with a reactive aluminosilicate feedstock. However, this simple process conceals many variables which can cause different reaction rates and reaction products which in turn influence the properties of the geopolymer.

A method of controlling the reaction rate and the subsequent reaction products and therefore properties of the geopolymer is to beneficiate the fly ash feedstock.

This chapter expands on the previous chapter by describing geopolymer made from beneficiated fly ash.

6.2 Comparison of Geopolymer from Unmodified and Beneficiated Fly Ash

In Chapter 5 the beneficiation of Collie fly ash was described. Beneficiation included sieving, milling and magnetic separation resulting in several subsets of Collie fly ash. Geopolymers made from the subsets of ash are expected to exhibit different properties based on starting Si:Al, surface and proportion of reactive component in the fly ash.

6.2.1 Discussion on Variables that can affect Geopolymer Synthesis

As mentioned in the introduction of this chapter there are a wide range of factors which can influence the synthesis of geopolymer. The main factors are listed below:

- The Si:Al of the amorphous portion of the fly ash.
- The amount of reactive aluminosilicate in the fly ash.
- The M:Al of the fly ash.
- Fineness of the fly ash.
- Solids:liquids ratio.
- pH of the alkaline activating solution.
- The amount of Si and Al dissolved from the fly ash by the alkali.
- Mixing energy and time.
- Curing temperature and humidity.

The Si, Al and M (where M is an alkaline cation) content and their ratios to each other is one of the primary parameters that researchers have to take into account for geopolymer production (Subaer 2004, Rowles 2004). Unfortunately the method most researchers have utilised in determining the Si:Al ratio is by XRF which only provides the bulk values and not the reactive amorphous content leading to incorrect formulation determination and subsequent variation in the predicted Si:Al of the geopolymer.

In addition to using bulk XRF for estimating reactive Si:Al in the fly ash a number of laboratories utilise fixed 'recipes' for the synthesis of geopolymer based on previous experience with OPC which is a very well understood material. Unfortunately due to the ever changing fly ash composition, a fixed recipe leads to variable chemical composition and final properties. To maintain consistent geopolymer product quality, rigorous and frequent assessment of the fly ash must be conducted to account for variation in composition.

The heterogeneous nature of fly ash provides a challenge for those designing an experiment to maximise the consumption of the amorphous aluminosilicate content of the feedstock. In addition to optimising the ingredients, the selection of a suitable mixer is required initiating geopolymerisation via collision theory. The collision theory relies upon the reactive components having sufficient energy and close proximity with each other to react and initiate the dissolution process (Atkins & De Paula 2006). If conditions of both the reagents and the process are not optimal, the dissolution and resultant polycondensation reaction will not initiate. Since it is

necessary to surpass the activation energy three key conditions need to be met to ensure the dissolution process is initiated and proceed to polycondensation. Firstly the reactants must make contact. Secondly the concentration of reactants must be high to increase the chances of reaction occurring. Thirdly the temperature of the constituents dictates the frequency of collisions.

The factors influencing the synthesis of geopolymer listed at the beginning of this section takes into account the three key conditions influencing the rate of reaction. Due to the relatively quick reaction time frame of the geopolymerisation process, the opportunity for dissolution of the reactive amorphous aluminosilicates of the fly ash is limited. This leads to a heterogeneous microstructure where the geopolymer gel is intermingled with quartz and carbon as well as unreacted and partially reacted fly ash particles.

The solids:liquids ratio plays an important role in the synthesis of geopolymer. If geopolymerisation is attempted with too high a solid content it will fail due to the lack of contact with the alkaline activating solution leading to lumps of fly ash weakly bound together with geopolymer gel. The limiting factor of low liquid content is generally the workability which will prevent the mixing of the ingredients. However if the liquid content is too high, the excess liquid will cause the mixture viscosity to become very low allowing for segregation of the unreactive content. The impact of excess liquid is also dependent on the component in excess either the water, the NaOH or the $NaSiO_3$.

The pH of the alkaline activating solution is a critical factor in geopolymer synthesis. A high pH (e.g. 14) indicates a high concentration of the required alkaline cation which will increase the chances of feedstock dissolution. If pH is low, the rate of reaction will suffer due to the low concentration of alkaline cations available. This will dissuade dissolution and geopolymerisation processes leaving the mostly unreacted alkaline solution to ultimately lead to efflorescence. If the activating solution is of sufficient quantity, it may have the effect of encouraging the formation of zeolites (dependent upon their inherent chemistry).

The amount of crystalline material present in fly ash will have an impact upon the geopolymer formation. Due to the large variation between fly ashes produced from different areas, the level of crystalline material will influence the rate of dissolution of the reactive content. For fly ashes that are comprised primarily of cenospheres, the level of crystalline material will have very little impact. However the majority of Collie fly ash particles are solid spheres with a large crystalline portion encapsulated by amorphous aluminosilicate material. The large level of dispersed crystalline material within each sphere in conjunction with limited activating solution and time, allows only the surface layer of amorphous content to readily dissolve. As it is believed that the amorphous material is predominantly on the surface (Section 4.4) this may not seem to be a large disadvantage. However this leaves an unknown amount of amorphous content remaining unutilised.

The fineness of the feedstock is directly proportional to the surface area of the particles available for reaction. With a larger surface area there will be greater opportunity for dissolution to occur when the activating solution is added. Milling can be used to further increase surface area and expose more internal content of the fly ash spheres to the alkaline activator.

The mixing regime effects contact area, temperature of the mixture and air entrainment. A more energetic mix regime ensures disaggregation of clumps resulting in a more homogeneous mix. In addition high speed mixing induces more of the reactants to come into contact with each other. An example of a high speed shear mixer is the Thinky ARE-250 planetary mixer which both revolves and rotates in a planetary motion at high speed allowing for effective dispersal, de-aerating and mixing. Due to the high speed mixing (1300 rpm for mixing and 2100 rpm for de-aerating), a large injection of thermal energy via particle friction increases the rate of reaction of the mixture. The Thinky ARE-250 mixer available was limited to a maximum load of 250 g, therefore a Hobart mixer was used when greater quantities were required to be mixed. The Hobart mixer uses a flat beater paddle with a slower mixing speed (60 or 124 rpm) which tends to introduce air into the mixture from the folding motion leading to an increase in porosity unless vibrated out prior to curing and setting. Due to the slow mixing speed there is little energy imparted to the mixture.

The environment in which the material is synthesised must be taken into consideration. Humidity, temperature and airflow will have an effect upon the reaction mechanisms, shrinkage and microscopic flaw formation (e.g. pores or cracks). Many geopolymer samples and products are cured in high humidity to ensure that the bulk material doesn't crack due to rapid water evaporation. As the bulk material has yet to complete the dissolution and polycondensation reactions, the solid particles are both separated and surrounded by a thin film of alkaline solution. If the geopolymer has an area exposed to atmosphere during curing, the resultant drying leads to the removal of water resulting in shrinkage. As the water diffuses to the surface for evaporation, interparticle separation decreases. If surface evaporation occurs at a faster rate than water diffusion from the interior, it can lead to the formation of cracks (Callister 1999). With larger liquids to solids ratio, shrinkage is more extensive. Airflow (based upon current climate conditions) will effect evaporation rate and temperature but can be negated in laboratory conditions and avoided by covering of the exposed surfaces with plastic in commercial applications.

6.2.2 Physical Properties

For this thesis, the Si:Al and Na:Al achieved by previous studies (Rowles 2004, Subaer 2004 and Hardjito & Rangan 2005) were used as a starting point. Then by taking into account the Si:Al of the amorphous component of the Collie fly ash a formulation was developed to give optimum strength while retaining mix workability. The strongest mix of geopolymer paste was achieved with a Si:Al = 2.6, Na:Al = 1.2 and H:Si = 5.0. This produced a compressive strength of 100 ± 4 MPa after 7 days.

A direct comparison of the geopolymer pastes created from the beneficiated fly ash proved to be difficult due to the increased rate of reaction relative to the unmodified fly ash and change of mean particle shape with milling. Essentially each step of the beneficiation process resulted in more amorphous aluminosilicate being available for dissolution due to removal of unreactive phases (sieving and magnetic separation) and exposing more of the fly ash amorphous content by fracturing the spheres (milling). It can be argued that fracturing of the spherical particles does decrease workability by converting them to irregularly shaped particles; however this

is largely offset by the increased amount and rate of reaction created by exposing the internal amorphous content. This leads to an increase in the amount of Si and Al available to form geopolymer. Due to this, there will be differing Si:Al and Na:Al ratios of the pastes, making direct comparisons of pastes from different starting materials difficult. The biggest impact arose from the decrease in workability as the rate of reaction increased. The effect of poor workability necessitated changes to the formulation to increase the liquids:solids ratio to enable mixing to occur.

Samples loaded in compression until failure exhibited a conchoidal fracture pattern typical of brittle amorphous materials. The conchoidal fracture (Figure 6.1) is more pronounced in the pastes synthesised from the more beneficiated feedstock, believed to be due to a greater volume of amorphous geopolymer matrix. All samples, irrespective of feedstock, exhibited excess fragmentation at ultimate failure so that the origin of the cracking could not be identified.

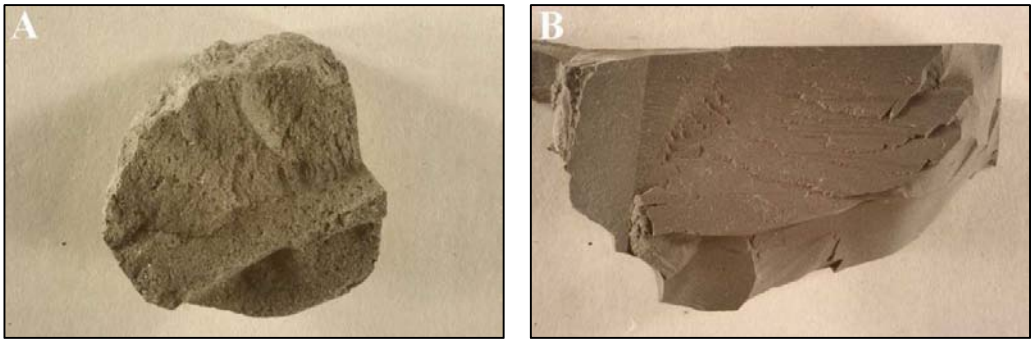

Figure 6.1: Fracture surfaces of (A) UFA geopolymer paste and (B) NM-MFA geopolymer paste.

Samples typically failed according to ASTM C 39 Type 2 fracture pattern with a well defined cone and vertical cracks running through the bulk material or ASTM C 39 Type 3 fracture pattern with columnar vertical cracking through both ends. The milled samples tended towards the Type 3 fracture pattern.

Compressive strength and Young's modulus results were obtained for geopolymer pastes made from beneficiated Collie fly ash samples and compared with the reference paste made from the unmodified Collie fly ash (Table 6.1). The

Rockwell hardness, apparent porosity, water absorption and bulk density of the samples were also measured and are shown in Table 6.2.

Table 6.1: Formulations of geopolymers made from unmodified and beneficiated fly ash with resultant compressive strength and Young's modulus.

Feedstock	Si:Al	Na:Al	H:Si	Solids:Liquids	Compressive Strength (MPa)	Young's Modulus (GPa)
UFA	2.6	1.2	5.0	2.2	100 ± 4	3.10 ± 0.13
NM-UFA	2.6	1.2	5.0	2.3	120 ± 2	3.35 ± 0.08
SFA	2.6	1.2	4.7	2.2	132 ± 7	3.58 ± 0.02
NM-SFA	2.6	1.2	4.9	2.3	125 ± 13	3.30 ± 0.04
MFA	2.5	1.7	6.9	1.6	110 ± 4	3.28 ± 0.05
NM-MFA	2.5	1.7	6.6	1.7	100 ± 10	3.12 ± 0.15

Table 6.2: Rockwell hardness, apparent porosity, water absorption and bulk density of the different geopolymers.

Feedstock	Rockwell Hardness (HRH)	Apparent Porosity (%)	Water Absorption (%)	Bulk Density (g/cm^3)
UFA	79 ± 4	24.7 ± 0.6	13.6 ± 0.3	1.82 ± 0.01
NM-UFA	85 ± 3	27.1 ± 0.9	15.4 ± 0.6	1.77 ± 0.02
SFA	86 ± 4	21.5 ± 1.5	11.2 ± 0.8	1.92 ± 0.02
NM-SFA	88 ± 4	18.3 ± 0. 9	9.8 ± 0.5	1.86 ± 0.01
MFA	72 ± 3	13.2 ± 2.2	7.2 ± 1.3	1.83 ± 0.02
NM-MFA	70 ± 3	11.8 ± 1.4	6.4 ± 0.9	1.84 ± 0.02

The sieved ash (SFA) showed a 32 % increase in strength relative to the unmodified fly ash. The removal of quartz and carbon is believed to be responsible for the increase which is consistent with observations of Shi *et al.* (2006) and Silverstrim *et al.* (1996). Sieving as a means of beneficiation is attractive as it is simple, inexpensive and only requires minor changes in the formulation from that used to make geopolymer from UFA.

The sieved and milled fly ash (MFA) showed a 10 % increase (significant to 1 SD) in strength relative to UFA. However to maintain workability the solids:liquids had to be decreased by 27 % and this led to changes in Si:Al and Na:Al preventing a direct comparison with paste made from UFA. The milling has had a dramatic effect on the reactivity of the amorphous aluminosilicate which was controlled by increasing the liquid content. An alternative approach would have been to add a boron compound to slow the reaction (Nicholson & Fletcher 2005).

Geopolymer made from non-magnetic fly ash (NM-UFA) had 20 % greater compressive strength than geopolymer made from UFA. Thus for the effort of removing crystalline iron oxides (71 %), a strength increase has been achieved with essentially the same Si:Al and Na:Al ratios. Geopolymer made from NM-SFA achieved the same strength within experimental uncertainties as geopolymer made from NM-UFA. Not unexpectedly, geopolymer made from NM-MFA required adjustment of the formulation to achieve workability, resulting in a compressive strength equal to UFA geopolymer.

Porosity did not seem to have as large an effect on compressive strength as expected. Thus changes in compressive strength appear to be influenced more by increased geopolymer gel in conjunction with the removal and/or alteration of secondary phases. Geopolymer pastes (with the exception of NM-UFA) showed a general decrease in porosity with further beneficiation compared to the original UFA material. However compressive strength values did not increase in a predictable linear manner with the decrease in apparent porosity. This indicates the complexity of the geopolymer matrix caused by the complex nature of fly ash.

Figure 6.2 show the rigidity of geopolymer paste due to an almost linear relationship between stress and strain. These curves confirm the brittleness of the geopolymer pastes as there is no evidence of plastic deformation after surpassing the ultimate strength of the material.

The Young's Modulus values (Table 6.1) of the geopolymer samples ranged between 3.10 and 3.58 GPa, matching the rise and fall of compressive strength values. These values are low compared to high strength cement (26 GPa) (Odelson *et*

al. 2007). The stiffness of the pastes showed increases of similar magnitude to the compressive strength results. Samples synthesised from non-magnetic powders show small increases in Young's Modulus. Porosity is known to have a deleterious effect upon the stiffness of a material as they reduce the cross-sectional area and act as stress concentrators. However, MFA and NM-MFA samples shown to have the lowest apparent porosity values displayed lower stiffness compared to samples from less beneficiated feedstock. This suggests that unreactive secondary phases and level of geopolymer formation are a strong influence requiring further investigation to gain a full understanding of this material.

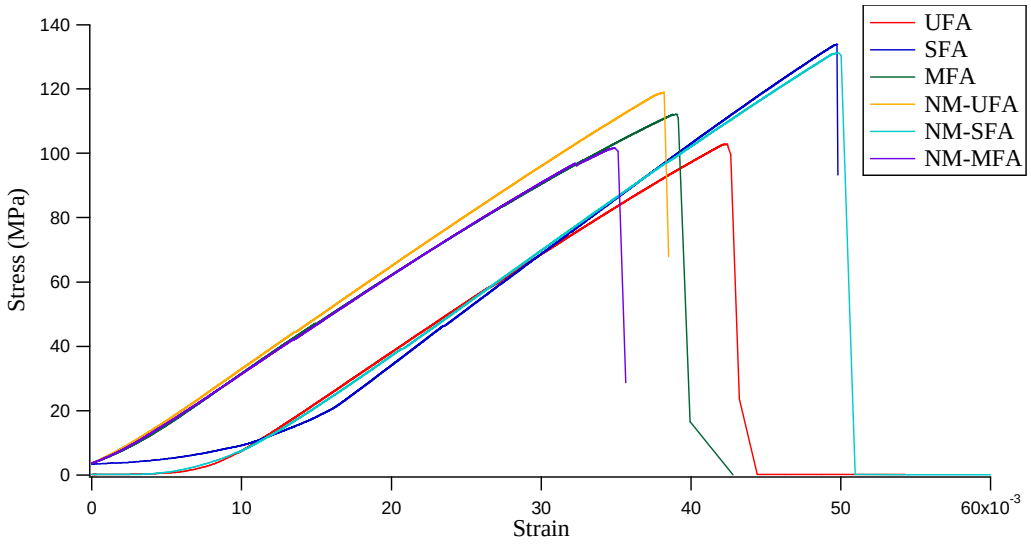

Figure 6.2: Stress-strain curve comparison of geopolymers made from UFA, SFA, MFA, NM-UFA, NM-SFA AND NM-MFA.

The individual bulk density values of the unreactive crystalline phases (Table 6.3) will affect the overall bulk density of the paste. Their influence is dependent upon their concentration within the fly ash in a similar fashion to the addition of aggregate in cement. This suggests that removal of the higher density iron oxide phases would decrease bulk density. Therefore it was expected (before factoring in porosity) that SFA would produce the highest density geopolymer as it contains a higher concentration of denser iron oxide particles and NM-UFA would produce the lowest density geopolymer as the denser iron oxide particles are mostly removed and there will be a larger concentration of low density amorphous carbon. Results showed NM-UFA geopolymer had the lowest density of 1.77 g/cm^3 and SFA geopolymer had the highest density of 1.92 g/cm^3. Predictably SFA and NM-SFA

displayed increased bulk density and decreased porosity when compared to UFA and NM-SFA, confirming the expectation that porosity and removal of dense material influenced bulk density values. However, results for MFA and NM-MFA were similar and showed only a minute increase in bulk density (~ 1%) for a disproportionate decrease of apparent porosity (~ 50 %) compared with UFA. This observation suggests that the milling process resulted in the highest level of dissolution of the fly ash amorphous material of all the subsets of fly ash tested in this category.

Table 6.3: Literature values of hardness and bulk density of crystalline phases (Ralph 2010).

Phase	Hardness (Moh)	Bulk Density (g/cm^3)
Hematite	5 – 6	5.3
Maghemite	6	4.9
Magnetite	5.5 – 6.5	5.2
Mullite	6 – 7	3.2
Quartz	7	2.7

The Rockwell test is a suitable for measuring the hardness of geopolymer as the large ball indentor encompasses a mix of bulk matrix and unreacted secondary phases. Unfortunately, no clear difference in hardness for beneficiated fly ash geopolymers could be discerned when uncertainties are taken into account relative to UFA. However, there is a noticeable difference (~ 20 %) between the sieved (SFA and NM-SFA) and milled (MFA and NM-MFA) samples when compared against each other. The lower hardness of the milled fly ash geopolymers is due to the distinctly different microstructure (see Section 6.2.4) which is less resistant to deformation due to a larger proportion of geopolymer gel compared to large sized secondary phases present in the SFA samples.

The apparent porosity and water absorption values agreed with the prediction of increased beneficiation leading to decreased porosity and water absorption

because of increasing homogeneity of the geopolymer microstructure. The two variables which have the largest influence upon porosity and absorption are the presence of amorphous carbon and size and distribution of pores. Amorphous carbon was shown to consist of either large sponge-like particles or very fine rod-like particles (Sections 4.3 and 5.2). The effect of these large sponge-like carbon particles are very potent creating a large difference between the BET surface area results between UFA and SFA (Section 5.2). Removal of the larger particles would decrease water absorption during geopolymerisation. The change in porosity and its impact on geopolymer microstructure will be further elaborated in Section 6.2.4.

6.2.3 X-Ray Diffraction

A comparison of the XRD patterns of feedstock with their resulting geopolymer paste (Figure 6.3) show little change in crystalline content. However visual inspection of the patterns shows a decrease in amorphous content of the feedstock and the formation of the geopolymer amorphous hump at higher 2θ.

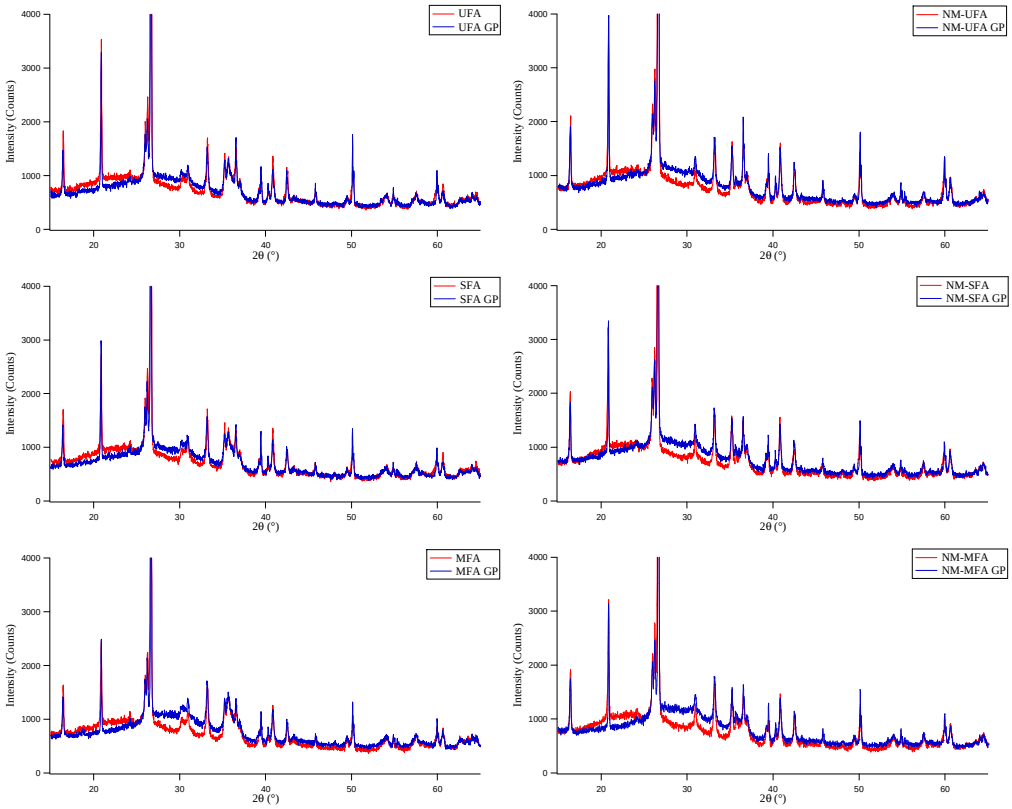

Figure 6.3: XRD patterns of feedstock and corresponding geopolymer paste.

The position of the geopolymer amorphous hump was determined using TOPAS (Bruker) to fit the broad peaks (Table 6.4). The geopolymer amorphous hump (28 – 29 º 2θ) was found to be centred at a position 6 º 2θ higher than that of the feedstock (22 – 23 º 2θ).

Table 6.4: Comparison of amorphous peak position of original and beneficiated fly ash and the geopolymers made from these different feedstocks.

Feedstock	Feedstock Peak Position (º2θ)	Geopolymer Peak Position (º 2θ)
UFA	21.9 ± 0.2	28.2 ± 0.2
NM-UFA	21.9 ± 0.2	27.9 ± 0.2
SFA	22.2 ± 0.2	28.1 ± 0.2
NM-SFA	22.0 ± 0.2	27.8 ± 0.2
MFA	22.7 ± 0.3	28.9 ± 0.2
NM-MFA	22.6 ± 0.3	28.4 ± 0.2

The characteristic geopolymer amorphous peak present in diffraction patterns is a convolution of the contributions from geopolymer and remnants of the unreacted feedstock. The position and width of the geopolymer peak can be used to estimate the level of feedstock consumption. If there is a sizable amount of undissolved feedstock, the peak position would be at a lower 2θ value reflecting the dominance of the feedstock peak. Therefore if total dissolution was to occur, the peak position would be at a higher 2θ value as there would be no contribution from the feedstock peak. This prediction is supported by both milled samples where the higher level of dissolution and corresponding increase in geopolymer binder results in a peak at a higher 2θ. It is worth noting that the approximately 6 º (2θ) shift in amorphous peak position is going from fly ash to geopolymer represents a 20 % decrease in d-spacing.

Table 6.5 displays the HWHM values of both sides of their associated peak positions (Table 6.4), indicating that the amorphous peaks of the feedstocks are asymmetric. The corresponding geopolymer amorphous peaks are clearly more symmetric. It is also evident that the peak width of geopolymers decrease with level

of beneficiation with MFA and NM-MFA having the narrowest peaks. From the results presented, it is apparent that amorphous peak position and width is a good predictor of the level of geopolymerisation. Although this work is in its infancy it clearly suggests that profile analysis of XRD patterns has much more to offer than previously thought.

Table 6.5: Comparison of calculated half width half maximum (HWHM) of original and beneficiated fly ash and the geopolymers made from these different feedstocks.

Feedstock	Feedstock HWHM (Left) (° 2θ)	Feedstock HWHM (Right) (° 2θ)	Geopolymer HWHM (Left) (° 2θ)	Geopolymer HWHM (Right) (° 2θ)
UFA	2.32	11.40	7.84	6.58
NM-UFA	2.42	11.56	7.06	8.00
SFA	2.50	11.12	7.79	6.72
NM-SFA	3.15	11.76	7.45	7.32
MFA	2.92	11.28	5.87	5.66
NM-MFA	2.88	11.17	4.91	6.50

When the geopolymer XRD patterns are plotted together (Figure 6.4), it can be seen that beneficiation by milling and removal of unreactive magnetic iron oxides resulted in increased intensity of the characteristic geopolymer hump. This is due to the proportional increase in amorphous content in the fly ash and the associated increase in total dissolution achieved by increasing the surface area of fly ash particles, leading to the increased level of geopolymer. This is verified by SEM images shown in the next section.

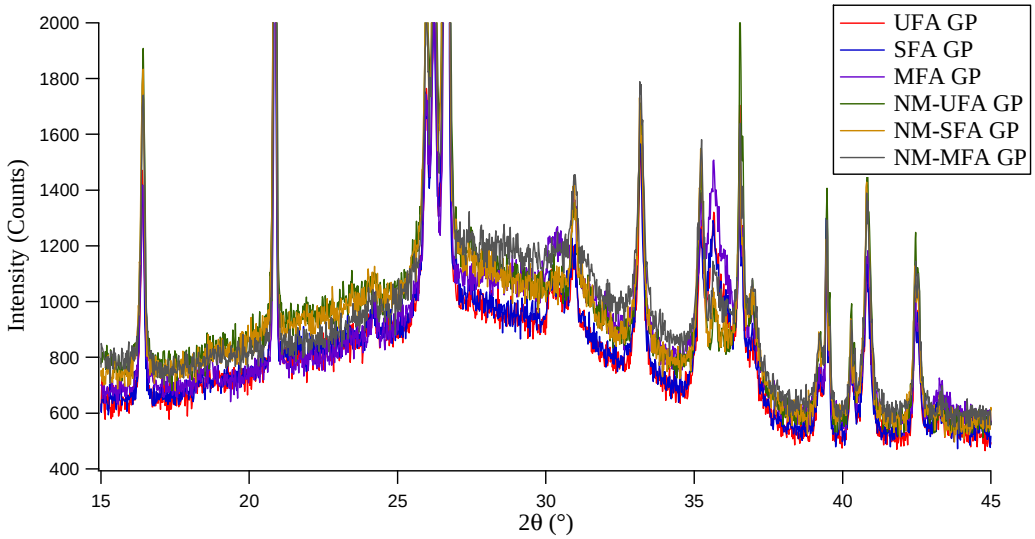

Figure 6.4: Comparison of XRD patterns from geopolymer of different feedstocks showing change in intensity and peak position of the geopolymer amorphous hump.

6.2.4 Microstructure

Measurement of compressive strength, density and porosity provides information about geopolymer performance but does not indicate the level of fly ash dissolution and subsequent geopolymerisation. SEM imaging and EDS were used to directly observe the microstructure and complement physical property measurements. SEM imaging can be used to ascertain matrix homogeneity, porosity, level of fly ash dissolution and crack formation.

Polished cross-sections of geopolymer paste made from UFA viewed using a SEM (Figure 6.5) show a highly heterogeneous microstructure. The microstructure is composed of a geopolymer matrix with dispersed carbon, quartz and unreacted fly ash spheres. The brighter spheres are composed of iron oxide. A number of cracks are present which are believed to occur during the sample preparation process of cutting, grinding, polishing and subsequent dehydration when placed in the SEM vacuum. Cracks can be seen to be pinned or deflected by particles embedded within the geopolymer matrix.

Figure 6.6 is a higher magnification view of the microstructure of paste made from UFA. Crystalline iron oxide appears to play no role in the dissolution and geopolymerisation processes as remanent spheres are left intact in the microstructure.

It is difficult to tell from Figure 6.6 but in most cases the outer layer of amorphous aluminosilicate has been dissolved leaving the iron oxide core. An interesting observation is the variety of ways that the iron oxide exists within the spheres, ranging from an extremely fine dendritic structure to clumps of large blocky pieces.

Geopolymer pastes made from SFA and NM-SFA have a similar microstructure to the pastes made from UFA and NM-UFA. Removal of the large particles has made the pores more noticeable albeit of smaller dimensions (Figure 6.7). The decrease in porosity size and volume has lead to a marginally lower apparent porosity for both SFA and NM-SFA (Table 6.2) and a subsequent increase in bulk density.

Compressive strength results from Table 6.1 demonstrate the role of pores in crack propagation and initiation. Sieved samples showed a large increase in compressive strength (up to 30 MPa) with a reduction in pore size. Pores are intrinsic volume distributed flaws that act as stress raisers in the bulk material due to the geometric discontinuity (Callister 1999, Quinn 2007). With an increase in load there is a proportionate increase in crack initiation from the pores. When the cracks are able to link with each other and propagate through the bulk, then the sample will fracture.

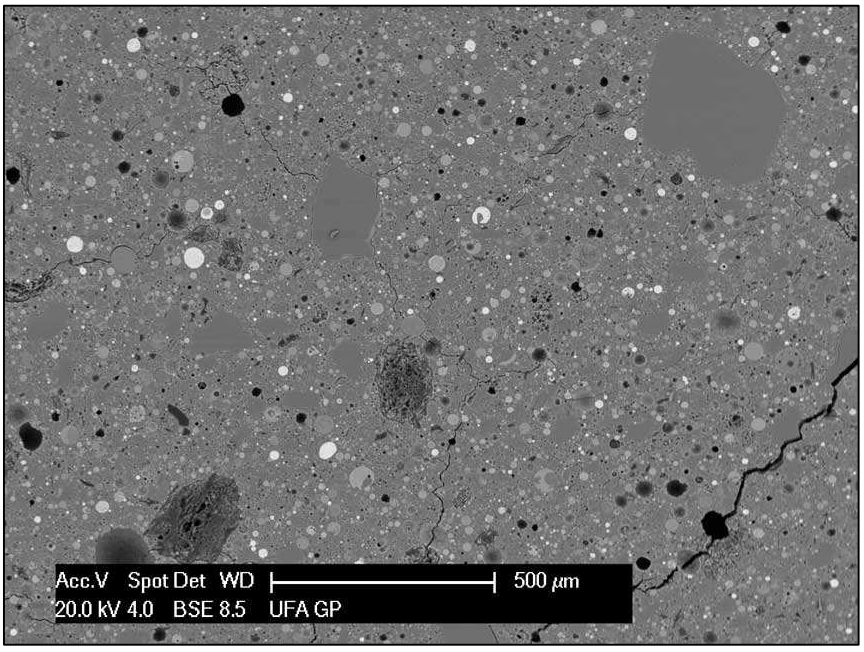

Figure: 6.5: Backscattered electron image of polished geopolymer paste synthesised from UFA. Note the relatively large carbon (very dark grey) and quartz (irregular shaped solid grey) particles along with many unreacted fly ash spheres. (Philips XL30)

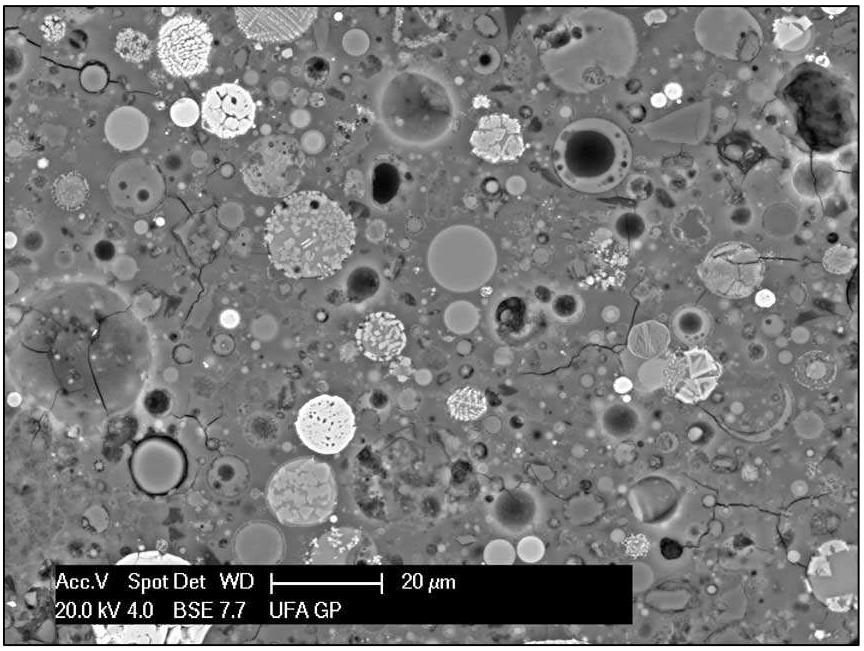

Figure 6.6: Backscattered electron image of polished geopolymer paste synthesised from UFA. (Philips XL30)

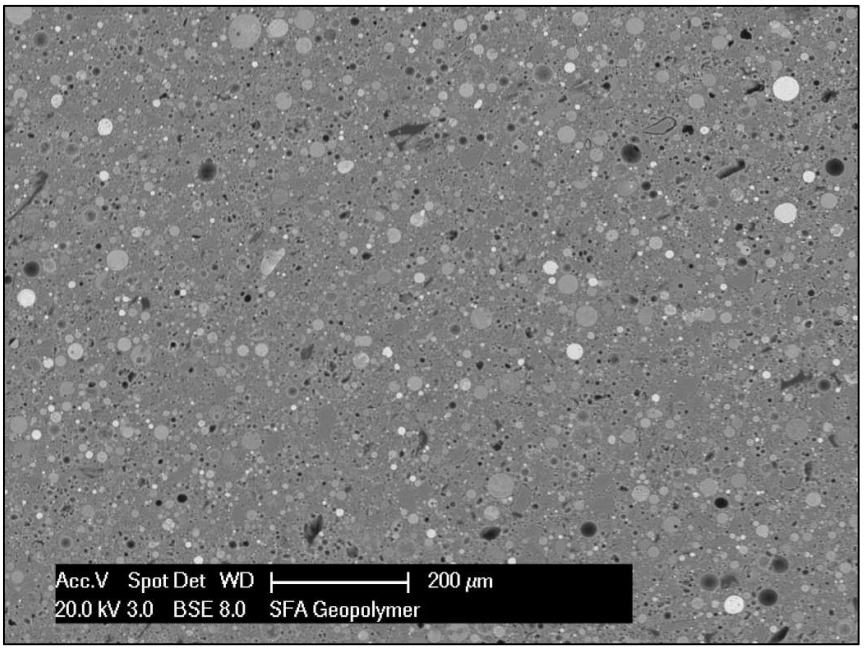

Figure 6.7: Backscattered electron image of polished geopolymer paste synthesised from SFA. (Philips XL30)

Polished cross-sectioned samples synthesised from MFA and NM-MFA still show a heterogeneous microstructure albeit only noticeable at higher magnification (Figure 6.8). The average pore size has decreased which is consistent with apparent porosity values (Table 6.2) however bulk density values for both MFA and NM-MFA are within experimental uncertainty of each other and UFA. The removal of large particles of unreactive phases in conjunction with milling promotes increased total dissolution of fly ash amorphous content leading to larger overall geopolymer content in comparison with the secondary phases. This leads to a material that has lower porosity and increased homogeneity as small secondary phases are able to disperse freely throughout the matrix (Figure 6.9). These attributes allow for consistency between samples and lessen the impact the secondary phases have upon the bulk material. At higher magnification when the matrix detail is more visible (Figure 6.9), it is comparable to those of the previously shown microstructures albeit with more irregularly shaped unreacted particles due to the grinding of the feedstock. Figure 6.9 also shows that the milling procedure adopted has not been efficient in grinding spheres less than about 10 µm. It can be seen in Figure 6.8 that due to the smaller 'natural aggregate', crack pinning and deflection is limited. Therefore when a crack is large enough, it can easily propagate throughout the structure without any hindrance. This leads to the conclusion that beneficiation has an inherent weakness if

geopolymer pastes are utilised as they do not contain adequate crack pinning components to hinder cracking. However, it can be speculated that as beneficiated feedstock leads to a more 'pure' geopolymer matrix, a higher aggregate content can be utilised in geopolymer concretes before it reaches the critical point where a decrease in compressive strength occurs as observed by Subaer (2004). Another inherent weakness introduced by the reduction in particle size of secondary phases in conjunction with increase geopolymer content is the reduced resistance to deformation (hardness). With large hard secondary phases readily available throughout the matrix, they are able to brace against one another to resist external forces. As these secondary phases are reduced in size and abundance, they are unable to provide resistance to deformation thus exhibiting a lower hardness.

The counter argument to the benefit of having unreactive crystalline phases in the matrix is that these phases can also act as microstructural flaws (Quinn 2007). As these inclusions/flaws have different elastic and thermal properties to the geopolymer matrix, they can cause cracking and may detach and pull away creating a void. Regardless, the removal of all unreactive phases is very difficult and thus generating a "pure" geopolymer binder from fly ash is not possible.

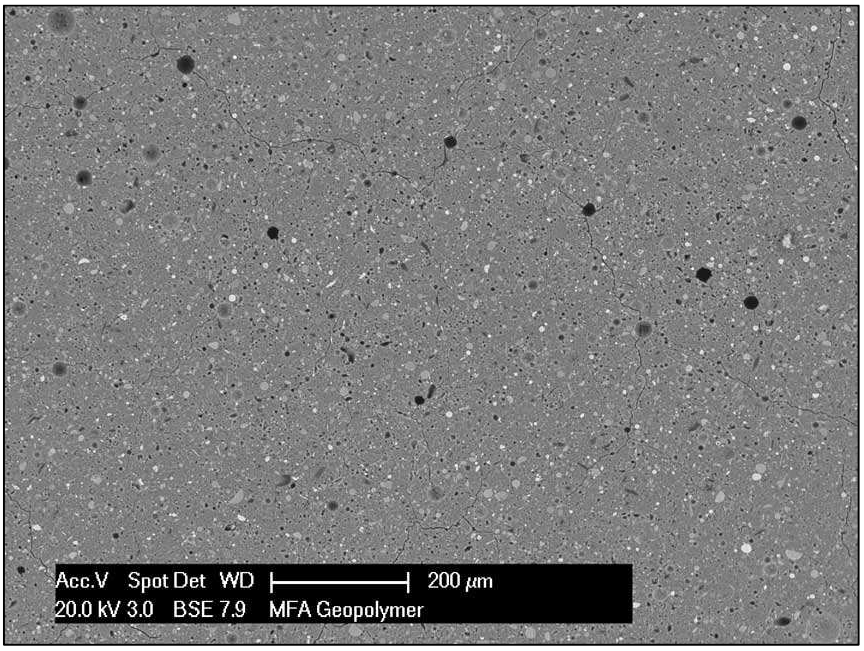

Figure 6.8: Backscattered electron image of polished MFA geopolymer paste. (Philips XL30)

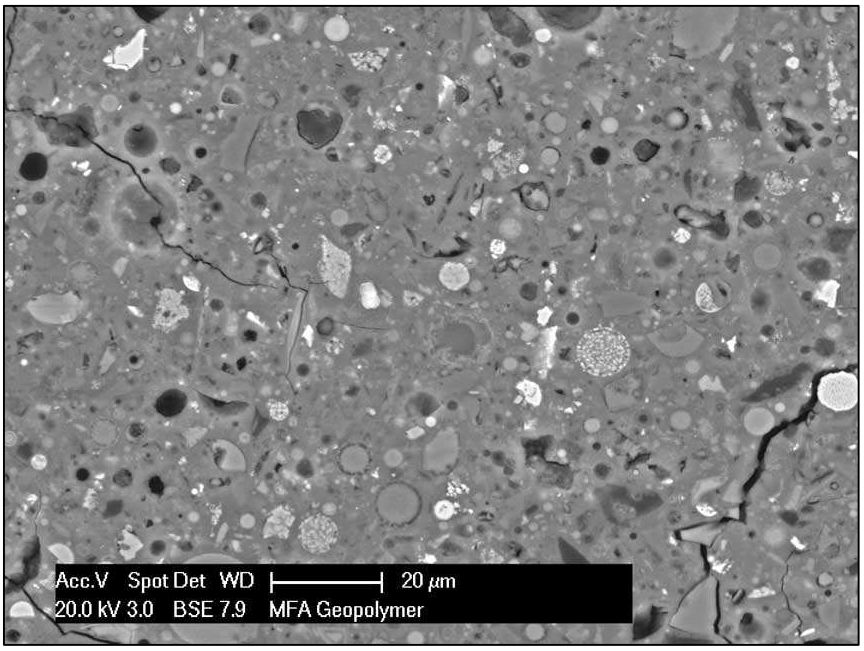

Figure 6.9: Backscattered electron image of polished MFA geopolymer paste. Residual particles are angular due to milling or still intact spheres which are too small to be milled. (Philips XL30)

The interfacial zone between the geopolymer paste and remnant fly ash particles is an important region which impacts on microcrack formation and strength development of the composite material. The fracture surface shown in Figure 6.10 illustrates the noticeable difference between the geopolymer gel, interfacial zone and remnant fly ash particle. The interfacial zone is a material that has a smoother consistency than the geopolymer matrix. It is believed that the interfacial zone is the initial amorphous gel created directly after the dissolution of the reactive amorphous content from the fly ash particle prior to its slow dissolution and subsequent re-precipitation to the secondary amorphous gel of a more ordered nature (Cundy & Cox 2005, Provis & van Deventer 2007a, Provis & van Deventer 2007b). This interface is not seen readily throughout the geopolymer matrix and is only in close proximity to remnants of fly ash spheres.

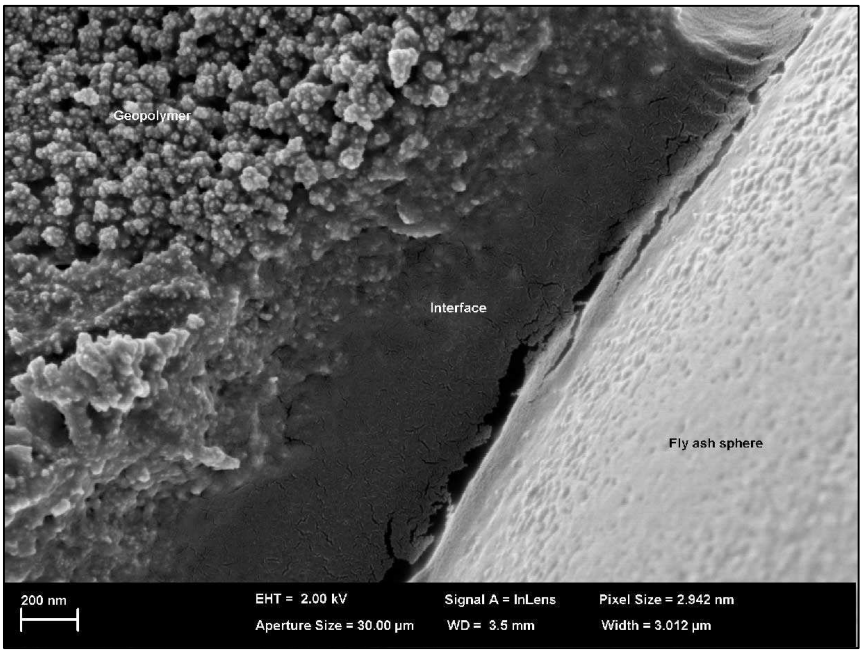

Figure 6.10: Secondary electron image of the fracture surface of UFA geopolymer paste showing geopolymer, interface and remnant fly ash sphere. (Zeiss Neon 40EsB)

Energy dispersive x-ray spectroscopy (EDS) was conducted on UFA geopolymer, interface and remnant fly ash sphere to observe differences in elemental composition (Figure 6.11 and Table 6.6). It must be noted that a fractured surface was utilised for this EDS analysis. Attempts to polish cross sectioned samples usually resulted in pull out of the interfacial zone and/or overlaying the interfacial zone with polishing residue. Therefore EDS results should be treated cautiously due to surface roughness limitations. In addition the interaction volume for a 10 keV electron beam in aluminosilicate is likely to be greater than 1 µm (see scale bar).

The Si:Al ratio was consistent for all three regions. Based on XRF/XRD analysis the aluminosilicate in the fly ash was expected to have a Si:Al of 1.9 which is lower than that measured by EDS. This could be due to preferential dissolution of Al from the fly ash which would increase the Si:Al ratio. The Na:Al of 0.1 or 0.2 in the fly ash could be due to partial interaction of the alkali leaving residual Na behind or Na originally present in the amorphous fly ash material. The Na:Al of 0.4 for the geopolymer is lower than the formulation value of 1.2. It was seen that there was a higher concentration of Fe in the geopolymer section. This is consistent with ferrihydrite precipitating that was precipitated out of solution prior to the formation

of the geopolymer gel. van Deventer *et al.* (2007) proposed that ferrihydrite nano-crystals can act as nucleation sites for the formation of geopolymer gel. Na concentration is shown to increase from the initial geopolymer gel to the secondary gel, however the Na:Al ratio is much lower than anticipated. This could be real or due to the electron beam driving the mobile Na atoms away from the interaction volume.

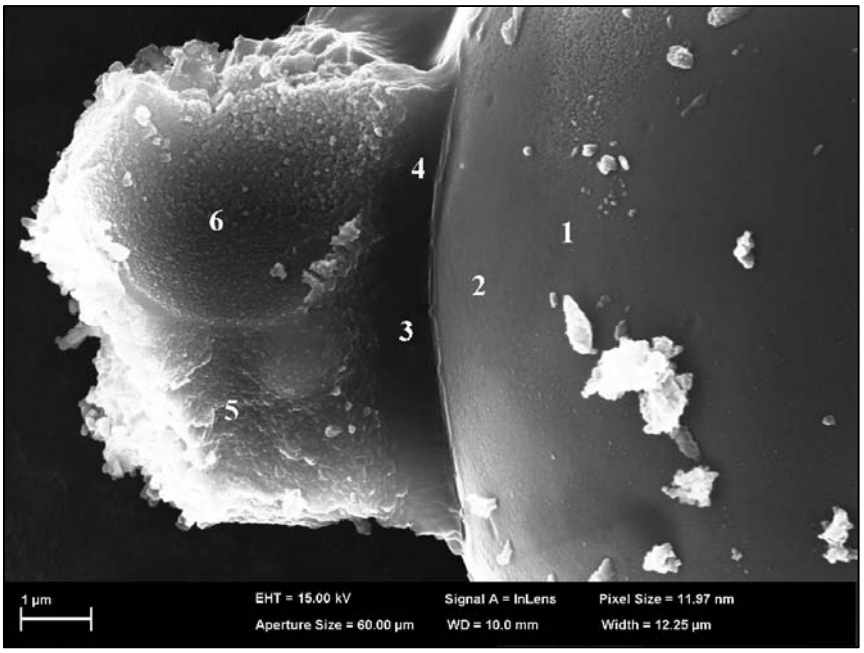

Figure 6.11: Secondary electron image of UFA geopolymer showing geopolymer, interface and remnant fly ash particle. Numbers indicate EDS analysis spots. (Zeiss Neon 40EsB)

Table 6.6: EDS results (atomic %) from 6 different spots on the fly ash sphere, interface and geopolymer. Spectra collected with a 10 keV electron beam.

Number	Label	Si	Al	Na	Fe	Si:Al	Na:Al
1	Fly Ash	29.09	10.98	0.98	1.15	2.6	0.1
2	Fly Ash	27.38	8.71	1.34	1.30	3.1	0.2
3	Interface	29.25	8.74	1.92	2.19	3.3	0.2
4	Interface	28.03	8.86	1.69	1.78	3.2	0.2
5	Geopolymer	30.02	8.82	3.25	2.49	3.4	0.4
6	Geopolymer	19.10	8.03	2.93	2.97	2.4	0.4

When viewed at low magnification the bulk UFA geopolymer matrix is seen to have a rough texture (Figure 6.12) and when viewed at higher magnification there is evidence of extensive subtle interlocking of the individual particles (Figure 6.12). It is seen that geopolymer is not a continuous matrix but an agglomeration of particles interlocked and melded together (Figure 6.13) which is similar to those reported by Kriven *et al.* (2003) in metakaolin based geopolymer. Due to this interlocking nature, micropores and voids are prevalent throughout the geopolymer matrix which is only noticeable at higher magnification.

With further beneficiation there is a noticeable increase in the size of the interlocked geopolymer particles (Figure 6.14, 6.15, 6.16 and 6.17). These larger particles are a result of the continued melding of particles initiated by the increased rate of reaction during both dissolution and the geopolymerisation process. The larger particle size is only achievable with extensive beneficiation of the fly ash.

With the removal of unreactive secondary phases, such as magnetic iron oxide, a more homogeneous matrix is formed. Paste synthesised from NM-MFA showed increase geopolymer particle size (Figure 6.16). This melding can be observed to encompass large volumes of geopolymer material making large plates (Figure 6.17) leading to a more typical ‘glassy’ appearance.

Exposure to air (1 week) of the hardened pastes synthesised from milled (both MFA and NM-MFA) fly ash caused further apparent melding of the exposed microstructure, leading to the formation of rectangular prisms as observed in Figure 6.18. This phenomenon does not occur in the non-milled samples leading to the impression that the material is metastable and continues to evolve with time. The prisms seemingly orientate themselves in clusters. When viewed at higher magnification, the material gives the impression of partial melting and resultant flowing to bind to its nearest neighbours (Figure 6.19).

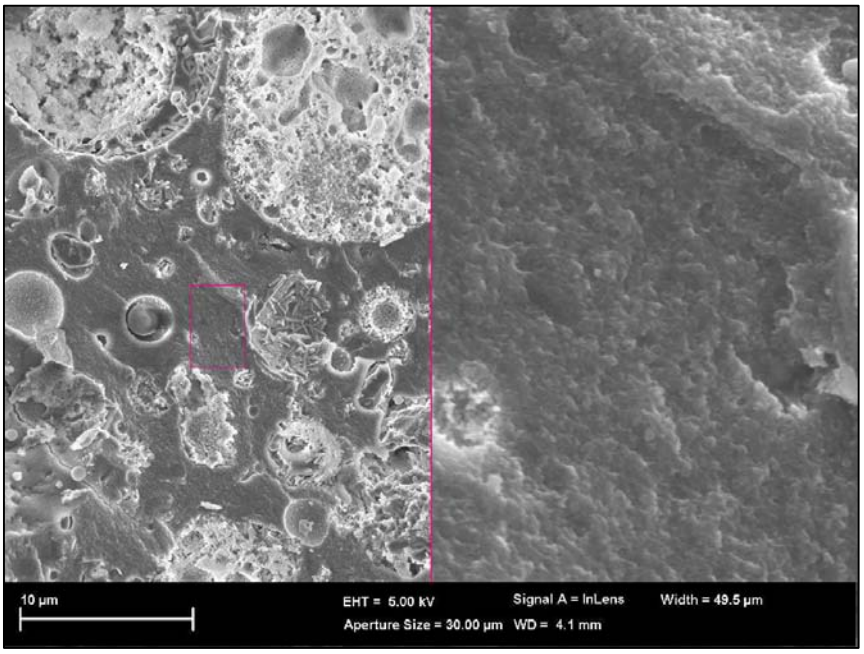

Figure 6.12: Secondary electron image of a UFA geopolymer paste. The left image is a low magnification view with the right image showing the magnified features of the geopolymer matrix from the boxed area in the left image. (Zeiss Neon 40EsB)

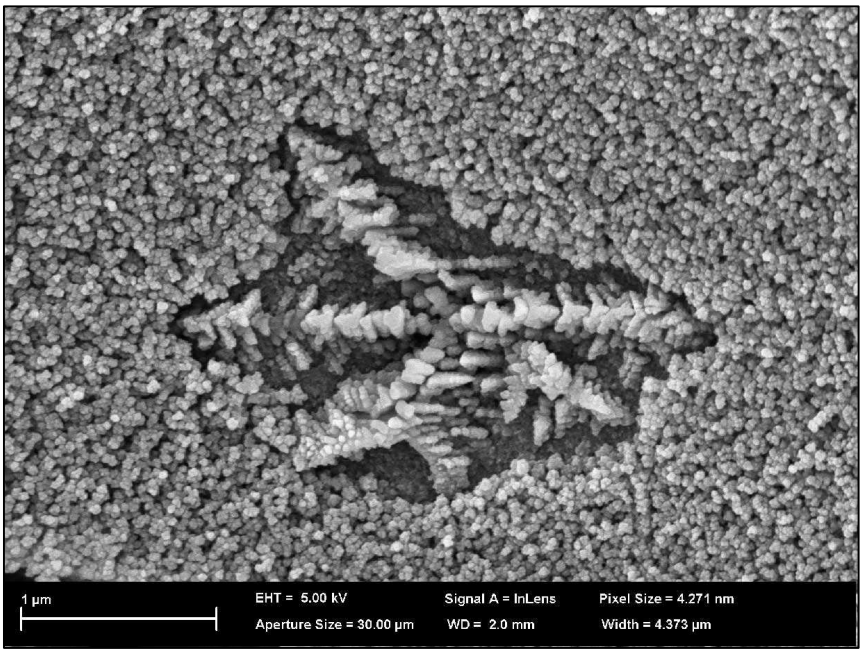

Figure 6.13: Secondary electron image of a UFA geopolymer paste. The central feature is dendritic iron oxide surrounded by geopolymer particles. (Zeiss Neon 40EsB)

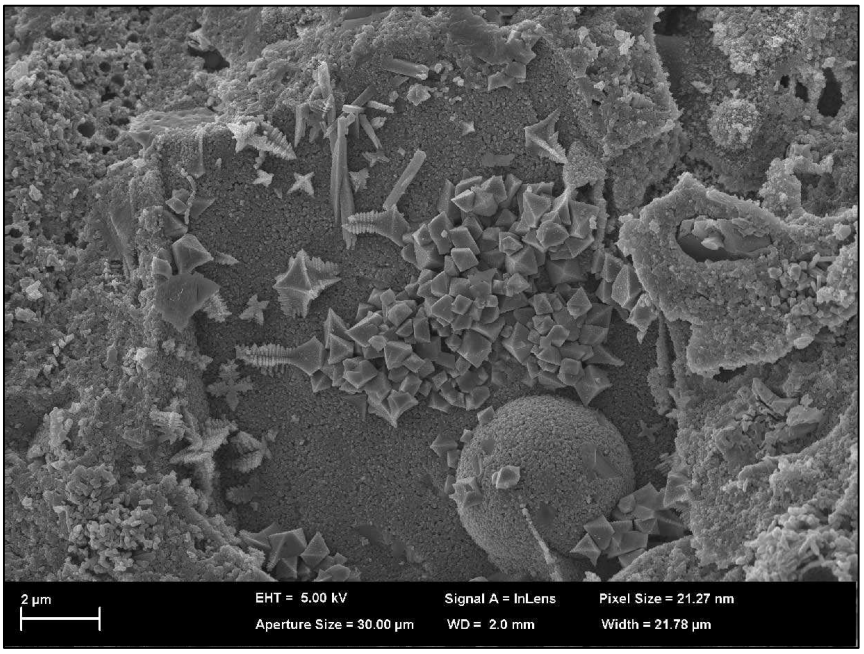

Figure 6.14: Secondary electron image of a hardened paste synthesised from MFA. The dendritic and octahedral iron oxides can be seen in the centre of the image surrounded by interlocked and fused geopolymer material. (Zeiss Neon 40EsB)

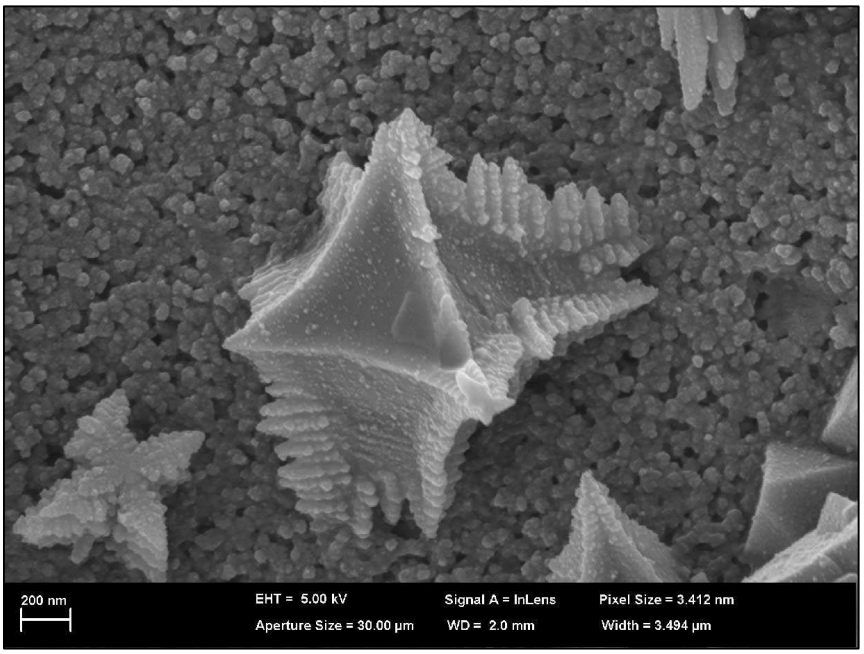

Figure 6.15: Secondary electron image of paste synthesised from MFA. The dendritic iron oxide 'podium' can be seen in the centre of the image surrounded by interlocked and fused geopolymer material. (Zeiss Neon 40EsB)

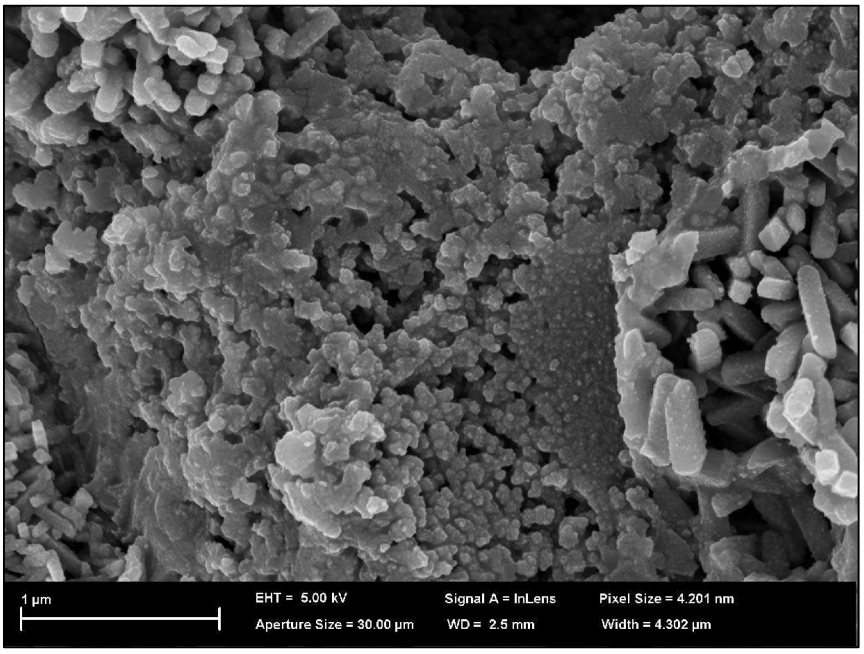

Figure 6.16: Secondary electron image of a NM-MFA geopolymer paste. Mullite crystals can be seen at the top left, bottom left and right sides of the image. Interlocked and melded geopolymer material is present in the centre of the image. (Zeiss Neon 40EsB)

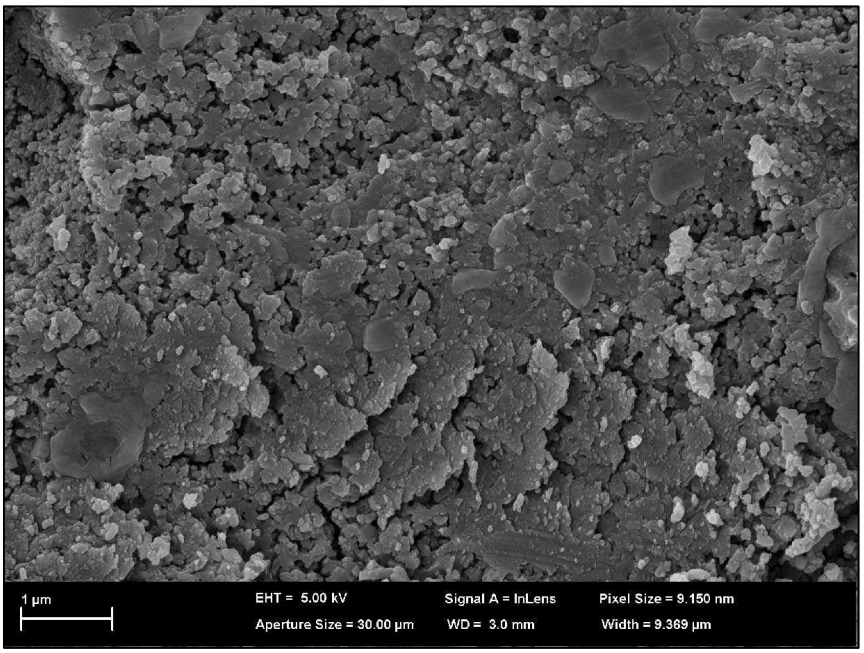

Figure 6.17: Secondary electron image of a NM-MFA geopolymer paste. The interlocked and melded geopolymer amorphous material can be observed to have differing size and shape. (Zeiss Neon 40EsB)

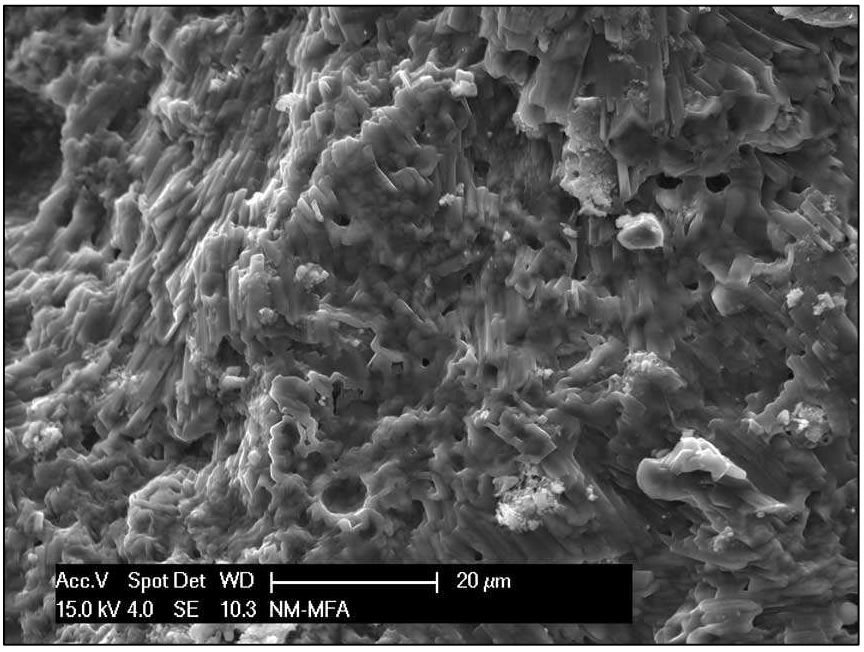

Figure 6.18: Secondary electron image of NM-MFA geopolymer paste. The interlocked and melded geopolymer appears to be made up of rectangular prisms. (Philips XL30)

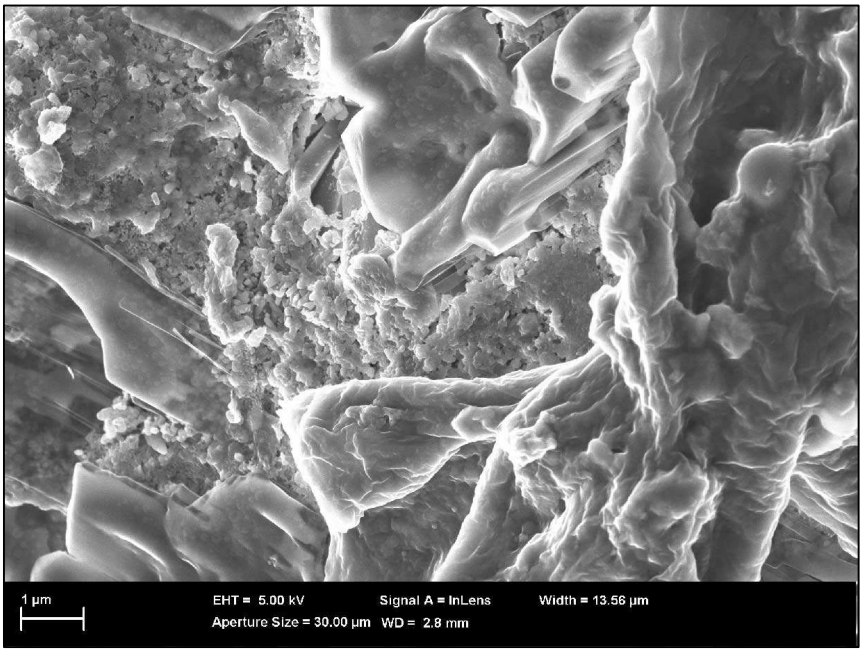

Figure 6.19: Secondary electron image of NM-MFA geopolymer paste. The interlocked and fused geopolymer particles can be observed to have differing size and shape. (Zeiss Neon 40EsB)

6.2.5 Dilatometry

Thermal expansion properties of geopolymer materials are important when considering their use for fire resistant coatings or panels. Dimensional changes can lead to failure of the material or lead to coating delamination from a substrate. The thermal expansion of geopolymer paste synthesised from unmodified and beneficiated fly ash were measured to ascertain the suitability of Collie fly ash based geopolymer for fire resistant applications.

Table 6.7 shows the length change of samples that have undergone heating and cooling at a rate of 5 ºC/min from room temperature to 900 ºC and back. Samples synthesised from UFA and SFA shrunk by the same amount and showed noticeable cracking. The NM-UFA samples shrunk the least, however displayed exaggerated cracking whilst the NM-SFA sample displayed only hairline cracking while undergoing large shrinkage. The largest length changes were observed by both MFA and NM-MFA samples although there were no visible signs of cracking. These observations can be explained by the amount and type of secondary phases in the geopolymer. The secondary phases all undergo separate rates of expansion and phase transformations. The presence of large quartz particles (UFA and NM-UFA) will restrict shrinkage however it will create cracking due to differential expansion between the quartz and geopolymer matrix. Sieving reduces the effect as the remaining quartz particles are smaller however the presence of iron oxides plus quartz will still cause cracking albeit to a lesser extent. With magnetic separation and milling, the reduction in both secondary phase content and particle size of secondary phases minimises the effect of the different shrinkage rates. This allows the shrinkage to be larger and more uniform without creating cracks.

Table 6:7: Shrinkage of geopolymer paste after cycling from ambient to 900 ºC and back to ambient.

Feedstock	Shrinkage (%)
UFA	2.6 ± 0.3
SFA	3.5 ± 0.5
MFA	9.3 ± 1.9
NMUFA	1.8 ± 0.6
NMSFA	6.4 ± 0.7
NMMFA	10.0 ± 2.6

Four well defined regions are present in the geopolymer expansion/shrinkage curves (Figure 6.20). The approximate temperature ranges of the four regions are: (1) room temperature – 100 ºC (2) 100 – 280 ºC (3) 280 – 580 ºC (4) 580 – 900 ºC.

Region 1 shows slight expansion during the initial dehydration of the sample with subsequent relaxation to its initial length by approximately 100 ºC. This can be attributed to water vapour causing slight expansion prior to its diffusion to the surface for evaporation. Region 2 demonstrates a decrease in sample length ranging from 2 % to 4 %, depending upon the feedstock utilised. The shrinkage observed in this region occurs due to further dehydration of the sample where chemically bound water is liberated. Fly ash that has undergone milling shrank the most leading to the impression that the reduction in particle size of crystalline material, particularly quartz, lessened the restriction that they imposed upon the geopolymer gel. Region 3 is almost a plateau where little microstructural change is occurring with temperature increase. The limited expansion that is seen in region 3 is due to the α-quartz (both primary and secondary) undergoing inversion to β-quartz (at approximately 573 ºC) in conjunction with the conversion of ferrihydrite (formed during the geopolymerisation process) to hematite. Region 4 does not show a general pattern of expansion/shrinkage that is shared by all samples. Initially all samples show shrinkage until approximately 600 ºC due to to the sintering of the geopolymer gel. For the milled samples (MFA and NM-MFA) the shrinkage continues consistently beyond the recording capabilities of the dilatometer. The NM-SFA sample also shrank past the capabilities of the dilatometer albeit showing a slower rate of

shrinkage after the initial rapid rate which halts at approximately 620 ºC. This could be attributed to the comparatively large β-quartz particles (compared to those from the milled samples) that would restrict shrinkage as the geopolymer gel is undergoing crystallisation via sintering. UFA, SFA and NM-UFA show a large increase in length in region 4 prior to a similar decrease in length. The increase in length is believed to be due to existing crystalline phases of varying composition, shape and size undergoing separate phase transformations leading to non-uniform rates of shrinkage. This, in conjunction with pore formation and growth, leads to the formation of stress within the material eventuating in large scale crack formation and propagation. The following shrinkage is believed to be due to the crystallisation occurring and subsequent rearranging of the structure (Rickard *et al.* 2010).

SEM images of the geopolymer after the heating cycle show large scale sintering in conjunction with an increase in average pore size (Figure 6.21). This follows similar trends witnessed by Bakharev (2006) and Rickard *et al.* (2010). The largest matrix disruption is viewed with UFA and NM-UFA geopolymer where the pores have managed to link up forming larger pore. All samples display smooth surface texture and less remnant fly ash spheres, indicating that undissolved amorphous material from the feedstock has melted producing a viscous flow.

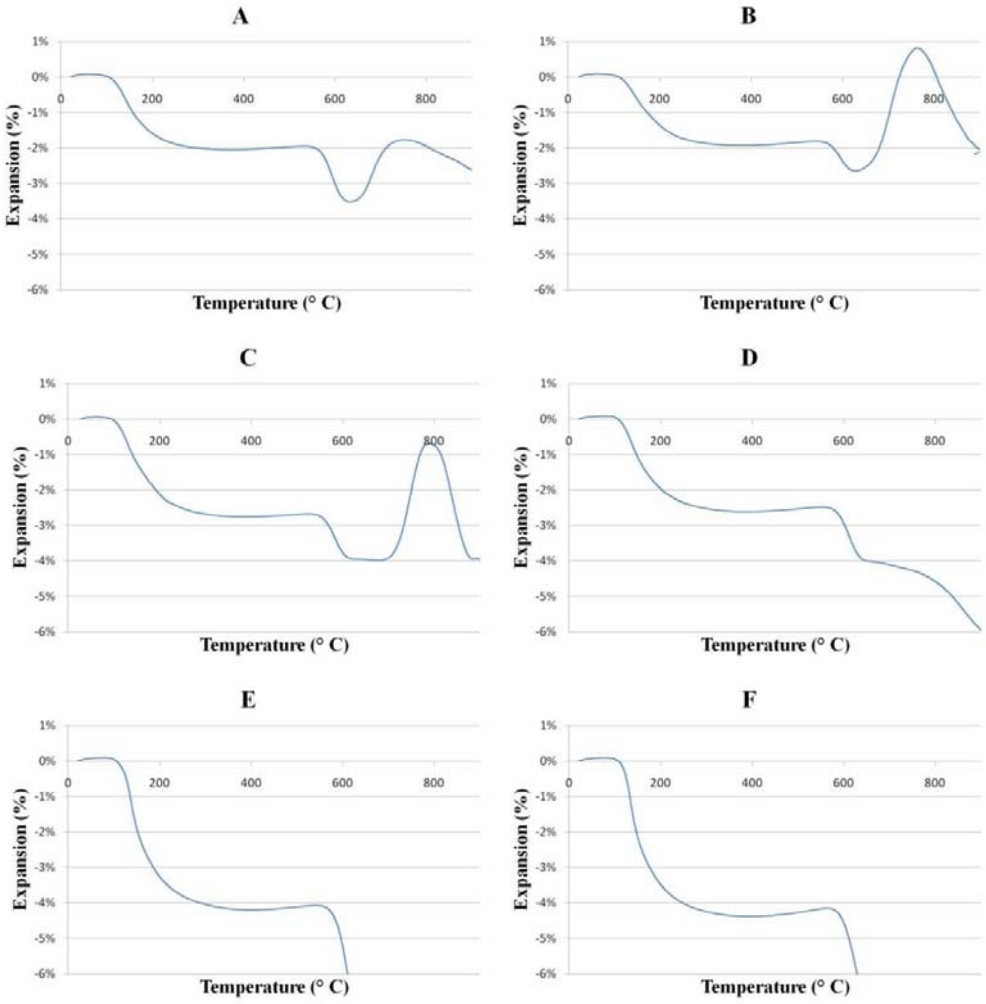

Figure 6.20: Thermal expansion of geopolymers synthesised from: (A) UFA, (B) NM-UFA, (C) SFA, (D) NM-SFA, (E) MFA and (F) NM-MFA.

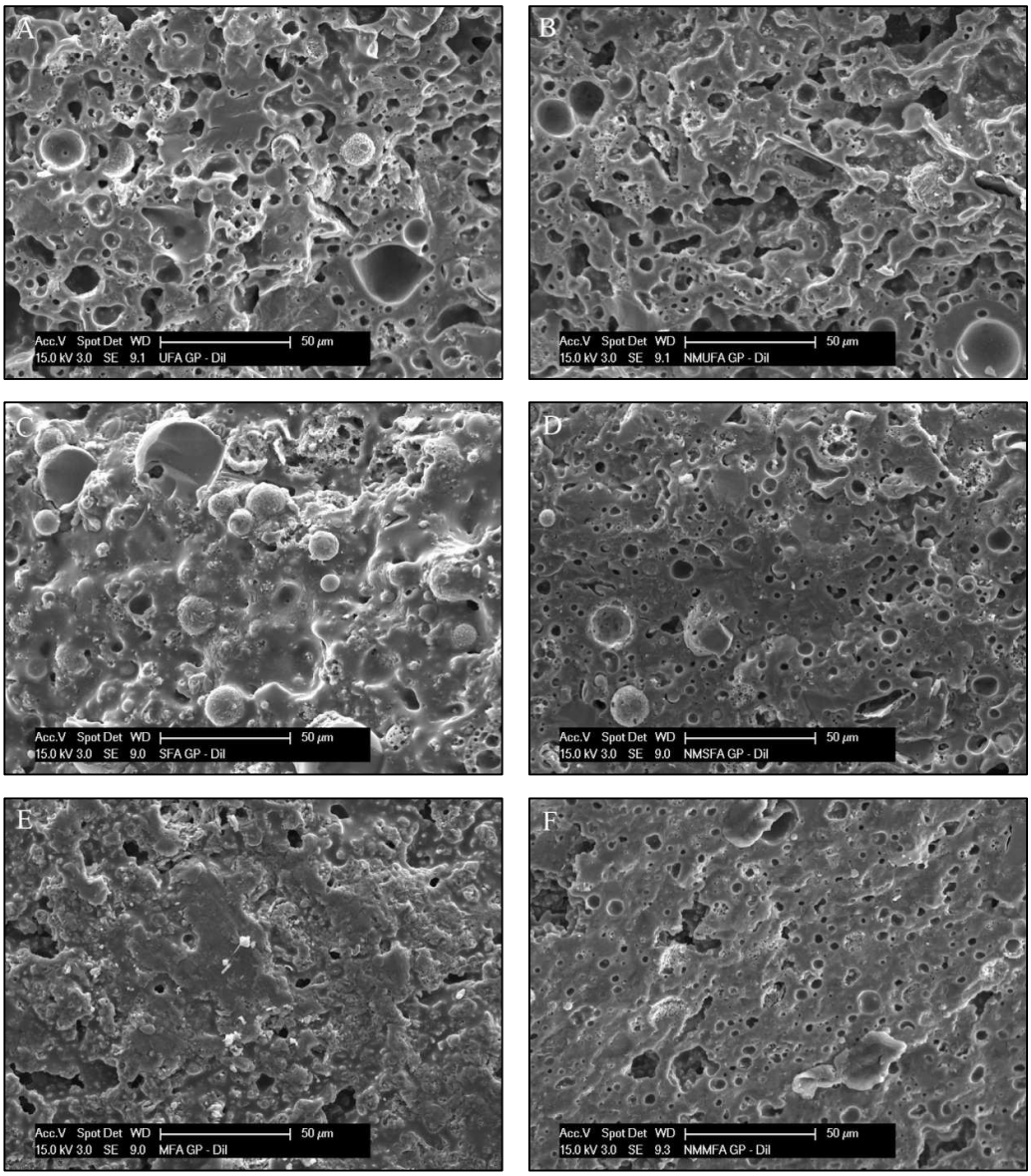

Figure 6.21: Secondary electron images of geopolymers after cycling from ambient to 900 ºC and back to ambient. Samples are: (A) UFA geopolymer, (B) NM-UFA geopolymer, (C) SFA geopolymer, (D) NM-SFA geopolymer, (E) MFA geopolymer and (F) NM-MFA geopolymer. (Philips XL30)

6.3 Summary

- Beneficiation increases rate and extent of dissolution, disallowing consistent Si:Al, Na:Al and H:Si molar ratios.
- A 20 – 30 % increase in compressive strength can be achieved for geopolymer made from SFA, MFA, NM-UFA and NM-SFA.
- MFA and NM-MFA geopolymers showed only a slight improvement in compressive strength when compared with geopolymer made from UFA. The lower than expected strength increase is directly attributable to changes in formulation required to maintain workability.
- Microstructure of geopolymer phase shows small particles which are melded and intimately interlocked rather than a continuous amorphous phase.
- Additional beneficiation produces an increase in the size of the geopolymer particles due to improved conditions for growth.
- MFA and NM-MFA geopolymer microstructure continued to change after demoulding and exposure to air. After 1 week, surfaces exposed to air show large orientated rectangular prisms.
- Dilatometry results show an increased rate of shrinkage with further beneficiation.
- MFA, NM-SFA and NM-MFA show consistent shrinkage with little or no cracking whilst UFA, SFA and NM-UFA exhibited severe cracking after high temperature exposure.

Chapter 7

Conclusions and Future Work

7.1 Conclusions

Unclassified Collie fly ash was thoroughly characterised. It is an iron rich Class F fly ash with the primary constituents being amorphous material, hematite, maghemite C, magnetite, mullite and quartz. The amorphous Al and Si oxide represents 40 wt.% of the bulk determined by combined XRF and QXRD while a 39 wt.% mass loss was obtained from dissolution measurements. Dissolution experiments and subsequent QEMSCAN analysis confirmed that crystalline phases were generally inert in concentrated NaOH and that amorphous iron does not directly affect the geopolymerismation process except to reduce the alkalinity of the activating solution.

The beneficiation of Collie fly ash was conducted in three stages: (1) separation of phases and size classification by sieving, (2) increase of surface area by milling and (3) removal of magnetic iron oxide. A noticeable reduction in quartz and carbon is observed when the fly ash is sieved to < 45 µm. Milling after sieving significantly increased surface area and the fracturing of spheres exposed more of the amorphous content to alkali dissolution. This produced a large increase in reactivity when compared to UFA. Magnetic separation only removed crystalline iron oxide phases and at the same time resulted in a reduced particle size and increased surface area for the non-magnetic fraction. There was a significant level of iron oxide present in the non-magnetic fraction believed to reside in the amorphous material.

Geopolymers created from the beneficiated fly ash demonstrated different properties. SFA and NM-SFA geopolymers exhibited improved physical properties with a more homogeneous microstructure compared to UFA geopolymer. MFA and NM-MFA geopolymers did not behave in a predictable manner. The milled samples showed a large decrease in apparent porosity and water absorption and produced the

most homogeneous microstructure. However, all other physical properties were similar to or worse than those of UFA geopolymer although this is in part due to changes in formulation required to maintain workability due to the increased reactivity.

As the level of fly ash beneficiation increased the resultant geopolymers exhibited increased homogeneity in the microstructure. The geopolymer gel when viewed at high magnification was shown to be comprised of small particles intimately interlocked and fused together rather than a continuous amorphous microstructure. These geopolymer particles increased in size with further beneficiation of the fly ash. The growth in particle size is attributed to the improved conditions for growth due to the increase in the amount of dissolution and subsequent increase in the level of geopolymerisation. Geopolymers made from highly beneficiated fly ash also showed increased shrinkage when exposed to high temperatures. MFA, NM-SFA and NM-MFA showed a consistent large shrinkage with little or no crack formation after exposure to 900 ºC.

It was shown that beneficiation of fly ash was capable of altering the properties of geopolymer. A simple process of sieving was capable of removing a modest amount of unreactive secondary phases leading to an increase in the physical properties of the geopolymers. Fully beneficiated fly ash (sieved, milled and magnetically separated) produced geopolymer which had similar or slightly reduced physical properties to those produced without any beneficiation. However, this geopolymer had reduced porosity and water absorption combined with large shrinkage with no crack formation when exposed to high temperatures which suggests that beneficiation can be used to manufacture superior fire resistant ash based geopolymer.

In conclusion, beneficiation of fly ash is a viable option for improving fly ash based geopolymer or for creating new geopolymer products that can be utilised in specialised roles.

7.2 Recommended Future Work

The information provided by this thesis can be considered a study into the effects the beneficiation of fly ash as a component of processing. It has been demonstrated that the beneficiation of fly ash can provide an increase in physical characteristics such as compressive strength however a more detailed study is required for optimisation of mixes and cost effectiveness.

The following recommendations would be suggested for future research endeavours:

1. Detailed studies into the optimisation of Si:Al and Na:Al molar ratios for producing geopolymers from beneficiated fly ash. This enables the optimisation of desired properties and a further understanding of the molar ratio constraints.
2. In situ XRD analysis of the geopolymer formation of the beneficiated fly ashes to observe the change in reactivity. By comparing the change in reaction rate via beneficiation, different processing procedures can be developed in conjunction with determining suitable roles for faster acting geopolymer.
3. A detailed study into the effect of ferrihydrite as nucleation sites and its effect upon physical properties is required. The addition of ferrihydrite finely dispersed and intimately linked to the geopolymer material would have an effect upon fire resistance and other properties.
4. Analysis of the adhesion and rheology of geopolymer synthesised from beneficiated feedstock. The information obtained would demonstrate the suitability of beneficiated fly ash geopolymer in comparison with unmodified fly ash geopolymer as pumpable cement in conjunction with its ability to be utilised as a spray on coat.
5. Fire testing beneficiated fly ash geopolymers would provide an interesting insight into the use of geopolymer as a fire resistant material. Dilatometry results have indicated that milling and magnetic separation affects the shrinkage and cracking of geopolymer.

7.3 Outlook

The majority of fly ash from coal fired power stations is currently placed in repositories that are ever increasing in size and demand a high ongoing maintenance cost. The high cost of allocating land for this purpose with the concomitant risk of contamination is no longer acceptable and alternative choices must be urgently investigated. Thus any solution that decreases the amount of ash stored in repositories should be welcomed and evaluated. It is clear that ash such as derived from Collie power station can be used, without further processing, to manufacture geopolymer for a range of applications. Beneficiation of the ash will expand the range of applications and enable higher performance geopolymer products to be manufactured. The additional cost of the beneficiation can be offset by the higher price of the specialist geopolymer product. In addition, separated phases such as activated carbon or pure quartz can be sold as high quality by-products. Ultimately all ash should be used as by products and one that should be given serious consideration is geopolymer.

References

- Alkan M., Hopa C., Yilmaz Z. & Güler H. 2005, "The effect of alkali concentration and solid/liquid ratio on the hydrothermal synthesis of zeolite NaA from natural kaolite", *Microporous and Mesoporous Materials*, Vol. 86, pp. 176 – 194
- Ash Development Association of Australia 2006, *Ash Development Association of Australia: Welcome*, http://www.adaa.asn.au/welcome.htm
- ASTM C 1069, *Standard Test Method for Specific Surface Area of Alumina or Quartz by Nitrogen Adsorption*, ASTM International, United States of America
- ASTM C 20, *Standard Test Methods for Apparent Porosity, Water Absorption, Apparent Specific gravity, and Bulk Density of Burned Refractory Bricks and Shapes by Boiling Water*, ASTM International, United States of America
- ASTM C 39/C 39M, *Standard Test Method for compressive Strength of cylindrical Concrete Specimens*, ASTM International, United States of America
- ASTM C 618, *Standard Specification for coal Fly Ash and Raw or Calcined Natural Pozzolan for Use in Concrete*, ASTM International, United States of America
- ASTM E 831, *Standard Test Method for Linear Thermal Expansion of Solid Materials by Thermomechanical Analysis*, ASTM International, United States of America
- Atkins P. & De Paula J. 2006, *Atkin's Physical Chemistry*, Oxford University Press, New York, United States of America
- Bakharev T. 2005, "Geopolymeric materials prepared using Class F fly ash and elevated temperature curing", *Cement and Concrete Research*, Vol. 35, pp. 1224 – 1232
- Bakharev T., 2006, "Thermal behaviour of geopolymers prepared using class F fly ash and elevated temperature curing", *Cement and Concrete Research*, Vol. 36, pp. 1134 – 1147

- Barbosa V.F.F., MacKenzie K.J.D. & Thaumaturgo C. 2000, "Synthesis and characterisation of materials based on inorganic polymers of alumina and silica: sodium polysilate polymers", *International Journal of Inorganic Materials*, Vol. 2, pp. 309 – 317
- Brouwer P. 2003, *Theory of XRF*, PANalytical B.V., Almelo, The Netherlands
- Brunauer S., Emmett O.H. & Teller E. 1938, "Adsorption of Gases in Multimolecular Layers", *Journal of the American Chemical Society*, Vol. 60, pp. 309 – 319
- Budinski K.G. & Budinski M.K. 2005, *Engineering Materials: Properties and Selection*, Pearson Education International, United States of America
- Callister W.D. 1999, *Materials Science and Engineering an Introduction*, John Wiley & Sons Inc., United States of America
- Chung F.H. & Smith D.K. 2000, *Industrial Applications of X-Ray Diffraction*, Marcel Dekker Inc., New York, United States of America
- Collins F. & Sanjayan J.G. 2001, "Microcracking and strength development of alkali activated slag concrete", *Cement & Concrete Composites*, Vol. 23, pp. 345 – 352
- Cornell R.M. & Schwertmann U. 2003, *The Iron Oxides: Structure, Properties, Reactions, Occurrence and Uses*, WILEY-VCH Verlag GmbH & Co. KGaA, Weinheim, Germany
- CPG Mineral Technologies, *Mineral Technologies – Mineral Separation and Mineral Processing Solutions*, http://www.mineraltechnologies.com.au/
- Cullity B.D. 1956, *Elements of X-ray Diffraction*, Addison-Wesley Publish Company Inc., Massachusetts, United States of America
- Cundy C.S. & Cox P.A. 2005, "The hydrothermal synthesis of zeolites: Precursors, intermediates and reaction mechanism", *Microporous and Mesoporous Materials*, Vol. 82, pp. 1 – 78
- Daux V., Guy C., Advocat T., Crovisier J-L. & Stille P. 1997, "Kinetic aspects of basaltic glass dissolution at 90 ºC: role of aqueous silicon and aluminium", *Chemical Geology*, Vol. 142, pp. 109 – 126
- Davidovits J. 1991, "Geopolymers: Inorganic Polymeric New Materials", *Journal of Thermal Analysis*, Vol. 37, pp. 1633 – 1656

- Davidovits J. 1994, “Properties of Geopolymer Cements”, *Proceedings First International Conference on alkaline Cements and concretes*, Kiev, Ukraine, pp. 131 – 149
- Debrincat D.P., Solnordal C.B. & van Deventer J.S.J. 2007, “Characterisation of inter-particle forces within agglomerated metallurgical powders”, *Powder Technology*, Vol. 182, pp. 388 – 397
- Dent Glasser L.S. & Kataoka N. 1981, “The chemistry of ‘alkali-aggregate’ reaction”, *Cement and Concrete Research*, Vol. 11, pp. 1 – 9
- Dent Glasser L.S. & Harvey G. 1984, “The Gelation Behaviour of Aluminosilicate Solutions containing Na^+, K^+, Cs^+ and Me_4N^+”, *Journal of the Chemical Society – Chemical Communications*, pp. 1250 – 1252
- De Silva P. & Sagoe-Crenstil K. 2007 “Medium-term phase stability of Na2O-Al2O-SiO2-H2O geopolymer systems”, *Cement and Concrete Research*, Vol. 38, pp. 870 – 876
- Dobbins M.S. & Burnet G. 1982, “Production of an iron ore concentrate from the iron-rich fraction of power plant fly ash”, *Resources and Conservation*, Vol. 9, pp. 231 – 242
- Drzal L.T., Rynd J.P. & Fort T. 1983, “Effects of Calcination on the Surface Properties of Kaolinite”, *Journal of Colloid and Interface Science*, Vol. 93, pp. 126 – 139
- Edugreen n.d., *EduGreen: Fly Ash*, http://edugreen.teri.res.in/explore/air/flyash.htm
- Fernandez-Jimenez A., Palomo A. & Criado M. 2005, “Microstructural development of alkali-activated fly ash cement: a descriptive model”, *Cement and Concrete Research*, Vol. 35, pp. 1204 – 1209
- García J.I.E., Campos-Venegas K., Gorokhovsky A &, Fernández A. 2006, “Cementitious composites of pulverised fuel ash and blast furnace slag activated by sodium silicate: effect of Na_2O concentration and modulus”, *Advances in Applied Ceramics*, Vol. 105, pp. 201 – 208
- Gomes S., François M., Abdelmoula M., Refait P., Pellissier C. & Evrard O. 1999, “Characterization of magnetite in silico-aluminous fly ash by SEM, TEM, XRD, magnetic susceptibility, and Mössbauer spectroscopy”, *Cement and Concrete Research*, Vol. 29, pp. 1705 – 1711

- Gomes S. & François M. 2000, “Characterization of mullite in silicoaluminous fly ash by XRD, TEM, and ^{29}Si MAS NMR”, *Cement and Concrete Research*, Vol. 30, pp. 175 – 181
- Goodwin R.W. 1993, *Combustion Ash/Residue Management: An Engineering Perspective*, Noyes Publications, United States of America
- Goretta K.C., Chen N., Gutierrez-Mora F., Routbort J.L., Lukey G.C. & van Deventer J.S.J. 2004, “Solid-particle erosion of a geopolymer containing fly ash and blast-furnace slag”, *Wear*, Vol. 256, pp. 714 – 719
- Gottlieb P., Wilkie G., Sutherland D., Ho-Tun E., Suthers S., Perera K., Jenkins B., Spencer S., Butcher A. & Rayner J. 2000, “Using quantitative electron microscopy for process mineral applications”, *Journal of the Minerals Metals and Materials Society*, Vol. 52, No. 4, pp. 24 – 25
- Gurba L, Heidrich C. & Ward C. 2007, *Coal Combustion Products Handbook*, Australian Black Coal Utilisation Research Limited, Australia
- Hardjito D. & Rangan B.V. 2005, *Development and Properties of Low-Calcium Fly Ash-Based Geopolymer concrete: Research Report C 1*, Curtin University of Technology, W.A., Australia
- Hart R.D., St Pierre T.G., Gilkes R.J., McKinley A.J., Siradz S. & Singh B. 2002, “Iron in soil kaolins from Indonesia and Western Australia”, *Clay Minerals*, Vol. 37, pp. 671 – 685
- Hinckley C.C., Smith G.V., Twardowska H., Saporoschenko M., Shiley R.H. & Griffen R.A. 1980, “Mössbauer studies of iron in Lurgi gasification ashes and power plant fly and bottom ash”, *Fuel*, Vol. 59, pp. 161 – 165
- Hosakawa Micron Ltd. n.d., *Hosokawa Alpine Laboratory Zig-Zag Classifier*, http://www.hosokawa.co.uk/zigzaglab.php
- Hower J.C., Rathbone R.F., Robertson D., Peterson G. & Trimble A.S. 1999, “Petrology, mineralogy, and chemistry of magnetically-separated sized fly ash”, *Fuel*, Vol. 78, pp. 197 – 203
- Inada M., Eguchi Y., Enomoto N. & Hojo J. 2004, “Synthesis of zeolite from coal fly ashes with different silica-alumina composition”, *Fuel*, Vol. 84, pp. 299 – 304
- Izquierdo M., Querol X., Davidovits, J., Antenucci D., Nugteren H & Fernández-Pereira 2009, “Coal fly ash-slag-based geopolymers: Microstructure and metal leaching”, *Journal of Hazardous Materials*, Vol. 166, pp. 561 – 566

- Jiang W. 1997, *Alkali Activated Cementitious Materials: Mechanisms, Microstructure and Properties*, UMI Dissertation Services, United States of America
- Jillavenkatesa A., Dapkunas S.J. & Lum L-S.H. 2001, *NIST Special Publication 960-1: Particle Size Characterization*, National Institute of Standards and Technology, Washington, United States of America
- Jones M.R., McCarthy A. & Booth A.P.P.G. 2006, "Characteristics of the ultrafine component of fly ash", *Fuel*, Vol. 85, pp. 2250 – 2259
- Kayali O. 2007, "Fly ash lightweight aggregates in high performance concrete", *Construction and Building Materials*, Vol. 22, pp. 2393 – 2399
- Khalil M.Y. & Merz E. 1994, "Immobilization of intermediate-level wastes in geopolymers", *Journal of Nuclear Materials*, Vol. 211, pp. 141 – 148
- Klobes P., Meyer K. & Munro R.G. 2006, *NIST Special Publication 960-17: Porosity and Specific Surface Area Measurements for Solid Materials*, National Institute of Standards and Technology, Washington, United States of America
- Kriven W.M., Bell J.L. & Gordon M. 2003, "Microstructure and microchemistry of fully-reacted geopolymers and geopolymer matrix composites", *Ceramics Transactions*, Vol. 153, pp. 227 – 250
- Kriven M.W. & Bell J.L. 2004, "Effect of alkali choice on geopolymer properties", *Proceedings of the 28th International Conference on Advanced Ceramics and Composites*, Daytona Beach, Florida, United States of America, pp. 99 – 104
- Kutchko B.G. & Kim A.G. 2006, "Fly ash characterization by SEM-EDS", *Fuel*, Vol. 85, pp. 2537 – 2544
- Lee W.K.W. & van Deventer J.S.J. 2002a, "The effect of ionic contaminants on the early-age properties of alkali-activated fly ash-based cements", *Cement and Concrete Research*, Vol. 32, pp. 577 – 584
- Lee W.K.W. & van Deventer J.S.J. 2002b, "The effects of inorganic salt contamination on the strength and durability of geopolymers", *Colloids and Surfaces A*, Vol. 211, pp. 115 – 126
- Lee W.K.W. & van Deventer J.S.J. 2002c, "Effects of anions on the formation of aluminosilicate gel in geopolymers", *Industrial & Engineering Chemistry Research*, Vol. 41, pp. 4550 – 4558

- Lee W.K.W. & van Deventer J.S.J. 2004, "The interface between natural siliceous aggregates and geopolymers", *Cement and Concrete Research*, Vol. 34, pp. 195 – 206
- Malhotra V.M. & Mehta P.K. 1996, *Pozzolanic and Cementitious Materials*, Gordon and Breach Publishers, England
- Malhotra V.M. & Mehta P.K. 2002, *High-Performance High-Volume Fly Ash concrete: Materials, Mixture Proportioning, Properties, Construction Practice and Case Histories*, Gordon and Breach Publishers, England
- Maoral M.C., Izquierdo M.T., Andrés J.M. & Rubio B. 2001, "Aluminosilicates transofmrations in combustion followed by DCS", *Thermochimica Acta*, Vol. 373, pp. 173 – 180
- Mie G. 1908, "Contributions to the optics and turbid media, particularly of colloidal metal solutions", *Annalen der Physik*, Vol. 25, pp. 377 – 445
- Murayama N., Yamamoto H. & Shibata J. 2001, "Mechanism of zeolite synthesis from coal fly ash by alkali hydrothermal reaction", *International Journal of Mineral Processing*, Vol. 64, pp. 1 – 17
- Nicholson C.L. & Fletcher R.A. 2005, *Geopolymers and Methods for their Production*, PCT Publication Number WO2005/019130
- Nugteren H.W., Butselaar-Orthlieb V.C.L. and Izquierdo M. 2009, "High strength geopolymers produced from coal combustion fly ash", *Global Nest Journal*, Vol. 11, pp. 155 – 161
- Odelson J.B., Kerr, E.A. & Vichit-Vadakan W. 2007, "Young's modulus of cement paste at elevated temperatures", *Cement and Concrete Research*, Vol. 37, pp. 258 – 263
- Palomo A., Grutzeck M.W. & Blanco M.T. 1999, "Alkali-actived fly ashes: A cement for the future", *Cement and Concrete Research*, Vol. 29, pp. 1323 – 1329
- Patil M.D., Eaton H.C. & Tittlebaum M.E. 1983, "$^{+57}$Fe Mössbauer spectroscopic studies of fly ash from coal-fired power plants and bottom ash from lignite-natural gas combustion", *Fuel*, Vol. 63, pp. 788 – 792
- Payá J., Monzó J., Borrachero M.V., Peris-Mora E. & González-López E. 1996, "Mechanical Treatment of Fly Ashes Part II: Particle Morphologies in Ground Fly Ashes (GFA) and Workability of GFA-Cement Mortars", *Cement and Concrete Research*, Vol. 26, pp. 225 – 235

- Premier Coal 2004, *Premier coal: Collie Basin Geology*, Premier Coal, Western Australia, Australia
- Provis J.L. & van Deventer J.S.J. 2007a, "Geopolymerisation kinetics. 1. In situ energy-dispersive X-ray diffractometry", *Chemical Engineering Science*, Vol. 62, pp. 2309 – 2317
- Provis J.L. & van Deventer J.S.J. 2007b, "Geopolymerisation kinetics. 2. Reaction kinetic modelling", *Chemical Engineering Science*, Vol. 62, pp. 2318 – 2329
- Quinn G.D. 2007, *NIST Special Publication 960-16: Fractography of Ceramics and Glasses*, National Institute of Standards and Technology, Washington, United States of America
- Ralph J. 2010, *Mineralogy Database – Mineral Collecting, Localities, Mineral Photos and Data*, www.mindat.org
- Ramsden A.R. & Shibaoka M. 1982, "Characterization and analysis of individual fly-ash particles from coal-fired power stations by a combination of optical microscopy, electron microscopy and quantitative electron microprobe analysis", *Atmospheric Environment*, Vol. 16, pp. 2191 – 2206
- Rees C., Lukey G.C. & van Deventer J.S.J. 2004, "The Role of Solid Silicates on the Formation of Geopolymers Derived from Coal Ash", *International Symposium of Research Students on Material Science and Engineering*, December 20 – 22, 2004, Chennai, India
- Rees C.A., Provis J.L., Lukey G.C. & van Deventer J.S.J. 2007, "The mechanism of geopolymer gel formation investigated through seeded nucleation , *Colloids and Surfaces*, Vol. 318, pp. 97 – 105
- Reilly M. 2008, "Tenn. Sludge Spill Challenges 'Clean Coal' Future", *Discovery News*, 25th December 2008, http://dsc.discovery.com/news/2008/12/25/tennessee-coal-ash.html
- Rickard W.D.A., van Riessen A. & Walls P. 2010, "Thermal Character of Geopolymers Synthesized from Class F Fly Ash Containing High Concentrations of Iron and α-Quartz", *International Journal of Applied Ceramic Technology*, Vol. 7, pp. 81 – 88
- Ristić M., De Grave E., Musić S., Popović S. & Orehovec Z. 2007, "Transformation of low crystalline ferrihydrite to α-Fe_2O_3 in the solid state", *Journal of Molecular Structure*, Vol 834, pp. 454 – 460

- Rowles M.R. & O'Connor B. 2003, "Chemical optimisation of the compressive strength of aluminosilicate geopolymers synthesised by sodium silicate activation of metakaolinite", *Journal of Materials Chemistry*, Vol. 13, pp. 1161 – 1165
- Rowles M.R. 2004, *The Structural Nature of Aluminosilicate Inorganic Polymers: A Macro to Nanoscale Study*, Ph.D. Thesis, Curtin University, Australia
- Scheetz B.E. n.d., *Chemistry and Mineralogy of Coal Fly Ash: Basis for Beneficial Use*, Materials Research Institute, United States of America
- Schmitt B., Brönnimann C., Eikenberry E.F., Gozzo F., Hörmann C., Horisberger R. & Patterson B. 2003, "Mythen detector system", *Nuclear Instruments and Methods in Physics Research A*, Vol. 501, pp. 267 – 272
- Shi C., Krivenko P.V. & Roy D. 2006, *Alkali Activated Cements and Concretes*, Taylor and Francis, London, England
- Singer M.J., Bowe L.H., Verosub K.L., Fine P. & Tenpas J. 1995, "Mössbauer spectroscopic evidence for citrate-bicarbonate-dithionite extraction of maghemite from soils", *Clays and Clay Minerals*, Vol. 43, pp. 1 – 7
- Silverstrim T., Rostami H., Larralde J. & Samadi A. 1996, *Fly ash cementitious material and method of making a product*, United States Patent 5,601,643
- Subaer 2004, *Influence of Aggregate on the Microstructure of Geopolymer*, Ph.D. Thesis, Curtin University, Australia
- Swanepoel J.C. & Strydom C.A. 2002, "Utilisation of fly ash in a geopolymeric material", *Applied Geochemistry*, Vol. 17, pp. 1143 – 1148
- Thomas A. 2005, *Western Australian Flyash: Investigation Into Collie & Muja Flyash Properties Influencing 20MPa Concrete Applications: Review of Preliminary Findings*, Flyash Australia, NSW, Australia
- van Jaarsveld J.G.S., van Deventer J.S.J. & Lorenzen L. 1997, "The potential use of geopolymeric materials to immobilise toxic metals: Part I. Theory and applications", *Minerals Engineering*, Vol. 10, pp. 659 – 669
- van Jaarsveld J.G.S., van Deventer J.S.J. & Schwartzman A. 1998, "The potential use of geopolymeric materials to immobilise toxic metals: Part II. Material and leaching characteristics", *Minerals Engineering*, Vol. 12, pp. 75 – 91

- van Jaarsveld J.G.S., van Deventer J.S.J. & Lukey G.C. 2002, "The effect of composition and temperature on the properties of the fly ash- and kaolinite-based geopolymers", *Chemical Engineering Journal*, Vol 89, pp. 63 – 73
- van Oorschot I.H.M. & Dekkers M.J. 1999, "Dissolution behaviour of fine-grained magnetite and maghemite in the citrate-bicarbonate-dithionite extraction method", *Earth and Planetary Science Letters*, Vol. 167, pp. 283 – 295
- Warren C.J. & Dudas M.J. 1988, "Leachability and partitioning of elements in ferromagnetic fly ash particles", *The Science of the Total Environment*, vol. 83, pp. 99 – 111
- Weng L., Sagoe-Crentsil K., Brown T. & Song S. 2005, "Effect of aluminates on the formation of geopolymers", *Materials Science and engineering B*, Vol. 117, pp. 163 – 168
- Williams R.P. & van Riessen A. 2010, "Determination of the reactive component of fly ashes for geopolymer production using XRF and XRD", *Fuel*, Vol. 89, pp. 3683 – 3692
- Willis S. 2003, *Mechanically Activated Fly Ash as a Reactant in the Production of High-Strength Aluminosilicate inorganic polymer Mortars and Carbon-Fibre Composites*, Ph.D. Thesis, University of Western Australia, Australia
- Winburn R.S., Grier D.G., McCarthy G.J. & Peterson R.B. 2000, "Rietveld quantitative X-ray diffraction analysis of NIST fly ash standard reference materials", *Powder Diffraction*, Vol. 15, pp. 163 – 172
- Xie Z. & Xi Y. 2001, "Hardening mechanisms of an alkaline-activated class F fly ash", *Cement and Concrete Research*, Vol. 31, pp. 1245 – 1249
- Xu H. & van Deventer J.S.J. 2000, "The geopolymerisation of alumina-silicate minerals", *International Journal of Mineral Processing*, Vol. 59, pp. 247 – 266
- Xu H. & van Deventer J.S.J. 2002, "Geopolymerisation of multiple minerals", *Minerals Engineering*, Vol. 15, pp. 1131 – 1139

List of Publications

Conference Publications during Ph.D. timeframe

- Chen-Tan N., Hart R. & van Riessen A. 2006, "Studies of Local Fly Ash for Geopolymer Production", *Proceedings of the 2006 Joint AXAA(WA) and WASM Conference*, ISBN 0-9586039-5-2, 22nd September – 24th September 2006, Margaret River, Western Australia, Australia
- Chen-Tan N.W., Williams R.P., Southam D.C., Lowe J.L., Hart R.D., van Riessen A. & Wright K. 2006, "Characterisation of class F fly ashes for alkali-activate aluminosilicate polymers: what's good and what's not", *Proceedings of the 16th Internationale Baustofftagung (Ibausil)*, ISBN 3-00-018263-2, 20th September – 23rd September 2006, Weimar, Germany
- Chen-Tan N., Southam D., van Riessen A., Ly C. 2007, "Characteristics of Fly Ash Precursors Effecting Geopolymerisation", *Proceedings of the Materials and Austceram 2007*, 4th July – 6th July 2007, Sydney, New South Wales, Australia
- Chen-Tan N. & van Riessen 2010, "Fly Ash Beneficiation and Geopolymer Properties", *Proceeding of the CIMTEC 2010 12th International Ceramics Congress*, ISBN 978-3-908158-44-8, 6th June – 11 June 2010, Montecatini Terme, Tuscany, Italy.
- Arie van Riessen and Nigel Chen-Tan, 2011 "Beneficiation of fly ash for production of geopolymers", *5th Australia-Korea Joint Symposia – Technology for Sustainabale Development of Minerals, Materials and Energy Resources*, 11-13 May 2011, Seoul, Republic of Korea, pp129-146. .

Journal Publications during Ph.D. timeframe

- Chen-Tan N.W., van Riessen A., Ly V.C., Southam D.C. 2009, "Determining the Reactivity of a Fly Ash for Production of Geopolymer", *Journal of the American Ceramic Society*, Vol. 92, pp. 881 – 887
- Temuujin J., Lee M., Chen-Tan N., van Riessen A. 2010, "Characterisation of geopolymers immersed in acid and alkaline liquids", *Cement and Concrete Composites*, submitted.
- Ahmed M.S., Zhao X., Zhou Z., Munroe P., Chen-Tan N., Li, L.K.Y., Xie Z. 2010, "Effect of thermal annealing upon residual stress and mechanical properties of nanostructured TiSiN coatings on steel substrates", *Journal of the American Ceramic Society*, accepted

Appendix 1 – ISCD Long views

Appendix 1 provides all the ISCD data used for Rietveld refinement of quantitative XRD using TOPAS 4.2 (Bruker).

Mullite

*data for ICSD #28544

Coll Code 28544
Rec Date 1980/01/01
Mod Date 2009/02/01
Chem Name Aluminium Silicon Oxide (4.64/1.38/9.68)
Structured Al4.644 Si1.357 O9.68
Sum Al4.644 O9.68 Si1.357
ANX A3X5
Min Name Mullite
D(calc) 3.16
Title A statistical model for the crystal structure of mullite
Author(s) Durovic, S.
Reference Kristallografiya
(1962), 7, 339-349
Soviet Physics, Crystallography (= Kristallografiya)
(1962), 7, 271-278
Unit Cell 7.549(8) 7.681(8) 2.884(3) 90. 90. 90.
Vol 167.23
Z 1
Space Group P b a m
SG Number 55
Cryst Sys orthorhombic
Pearson oP16
Wyckoff h4 g a
R Value 0.095
Red Cell P 2.884 7.549 7.681 90 90 90 167.225
Trans Red 0.000 0.000 1.000 / 1.000 0.000 0.000 / 0.000 1.000 0.000
Comments R(hk0,1,2)= 0.091, 0.084, 0.097, resp., R(h0l)= 0.093
Compound with mineral name: Mullite
The structure has been assigned a PDF number (calculated powder diffraction data): 01-074-2419
The structure has been assigned a PDF number (experimental powder diffraction data): 15-776
X-ray diffraction from single crystal
At least one temperature factor missing in the paper.

Atom	#	OX	SITE	x	y	z	SOF	H
Al	1	+3	2 a	0	0	0	1.	0
Al	2	+3	4 h	0.352(1)	0.161(1)	0.5	0.5567	0
Al	3	+3	4 h	0.233(5)	0.287(5)	0.5	0.1043	0
Si	1	+4	4 h	0.352(1)	0.161(1)	0.5	0.2863	0
Si	2	+4	4 h	0.233(5)	0.287(5)	0.5	0.053	0
O	1	-2	4 g	0.374(3)	0.279(3)	0	1.	0
O	2	-2	4 h	0.138(3)	0.078(3)	0.5	1.	0
O	3	-2	4 h	0.025(3)	0.475(3)	0.5	0.42	0

Std. Notes Transformation Method: Tidy
TRANS Origin 0 0 1/2
Std. Cell 7.5490 7.6810 2.8840 90 90 90
Std. Vol. 167.23
Std. Z 1
Std. SG PBAM
Std. Atom

Atom	#	OX	SITE	x	y	z	SOF
Al	1	+3	2 b	0	0	.5	1.
Al	2	+3	4 g	.35200	.16100	0	0.5567
Al	3	+3	4 g	.23300	.28700	0	0.1043
Si	1	+4	4 g	.35200	.16100	0	0.2863
Si	2	+4	4 g	.23300	.28700	0	0.053
O	1	-2	4 h	.37400	.27900	.5	1.
O	2	-2	4 g	.13800	.07800	0	1.
O	3	-2	4 g	.02500	.47500	0	.420

*end for ICSD #28544

Magnetite

*data for ICSD #30860

Coll Code 30860
Rec Date 1985/03/07
Mod Date 2007/08/01
Chem Name Iron Diiron(III) Oxide
Structured Fe3 O4
Sum Fe3 O4
ANX A3X4
Min Name Magnetite
D(calc) 5.2
Title Crystal structure and cation distribution in titanomagnetites (Fe3-x Tix O4)
Author(s) Wechsler, B.A.;Lindsley, D.H.;Prewitt, C.T.
Reference American Mineralogist (1984), 69, 754-770
Unit Cell 8.3958(2) 8.3958(2) 8.3958(2) 90. 90. 90.
Vol 591.82
Z 8
Space Group F d -3 m Z
SG Number 227
Cryst Sys cubic
Pearson cF56
Wyckoff e d a
R Value 0.01
Red Cell F 5.936 5.936 5.936 60 60 60 147.954
Trans Red 0.500 0.500 0.000 / 0.000 0.500 0.500 / 0.500 0.000 0.500
Comments Sample MT100-1350
Compound with mineral name: Magnetite
Neutron diffraction (powder)
The structure has been assigned a PDF number (calculated powder diffraction data): 01-075-1372
The structure has been assigned a PDF number (experimental powder diffraction data): 19-629
Temperature factors available
Structure type : Al2MgO4

Atom	#	OX	SITE	x	y	z	SOF	H	ITF(B)
Fe	1	+3	8 a	0.125	0.125	0.125	1.	0	0.37(4)
Fe	2	+3	16 d	0.5	0.5	0.5	0.5	0	0.47(4)
Fe	3	+2	16 d	0.5	0.5	0.5	0.5	0	0.47(4)
O	1	-2	32 e	0.25470(18)	0.25470(18)	0.25470(18)	1.	0	0.64(5)

Std. Notes Transformation Method: Tidy
TRANS Origin 1/2 1/2 1/2
Std. Cell 8.3958 8.3958 8.3958 90 90 90
Std. Vol. 591.82
Std. Z 8
Std. SG FD3-MZ
Std. Atom

Atom	#	OX	SITE	x	y	z	SOF
Fe	1	-2	16 c	0	0	0	0.5
Fe	1	+3	8 b	.375	.375	.375	1.
Fe	3	+2	16 c	0	0	0	0.5

*end for ICSD #30860

Zincite

*data for ICSD #34477

Coll Code 34477
Rec Date 1980/01/01
Mod Date 2006/04/01
Chem Name Zinc Oxide
Structured Zn O
Sum O1 Zn1
ANX AX
Min Name Zincite
D(calc) 5.66
Title Structure parameters and polarity of the wurtzite type compounds Si C - 2H
Author(s) Schulz, H.;Thiemann, K.H.
Reference Solid State Communications (1979), 32, 783-785
Unit Cell 3.253(1) 3.253(1) 5.213(1) 90. 90. 120.
Vol 47.77
Z 2
Space Group P 63 m c
SG Number 186
Cryst Sys hexagonal
Pearson hP4
Wyckoff b2
R Value 0.024
Red Cell P 3.253 3.253 5.213 90 90 120 47.773
Trans Red 1.000 0.000 0.000 / 0.000 1.000 0.000 / 0.000 0.000 1.000
Comments Compound with mineral name: Zincite
The structure has been assigned a PDF number (calculated powder diffraction data): 01-076-0704
The structure has been assigned a PDF number (experimental powder diffraction data): 36-1451
Temperature factors available
Structure type : ZnS(2H)
X-ray diffraction from single crystal

Atom	#	OX	SITE	x	y	z	SOF	H
Zn	1	+2	2 b	0.3333	0.6667	0	1.	0
O	1	-2	2 b	0.3333	0.6667	0.3820(8)	1.	0

Lbl	Type	U11	U22	U33	U12	U13	U23
Zn1	Zn2+	0.0061(1)	0.0061(2)	0.0081(3)	0.0030(1)	0	0
O1	O2-	0.0066(8)	0.0066(8)	0.0085(11)	0.0033(4)	0	0

Std. Notes Transformation Method: Tidy
Std. Cell 3.2530 3.2530 5.2130 90 90 120
Std. Vol. 47.77
Std. Z 2
Std. SG P63MC
Std. Atom

Atom	#	OX	SITE	x	y	z	SOF
Zn	1	+2	2 b	.33333	.66667	.00000	1.
O	1	-2	2 b	.33333	.66667	.38200	1.

*end for ICSD #34477

Quartz

*data for ICSD #41412

Coll Code 41412
Rec Date 2004/04/01
Mod Date 2008/02/01
Chem Name Silicon Oxide
Structured Si O2
Sum O2 Si1
ANX AX2
Min Name Quartz low
D(calc) 2.65
Title Crystal structures of quartz and magnesium germanate by profile analysis of synchrotron-radiation high-resolution powder data.
Author(s) Will, G.;Bellotto, M.;Parrish, W.;Hart, M.
Reference Journal of Applied Crystallography
(1988), 21(2), 182-191
Powder Diffraction
(1991), 6, 82-84
Unit Cell 4.91239(4) 4.91239(4) 5.40385(7) 90. 90. 120.
Vol 112.93
Z 3
Space Group P 32 2 1
SG Number 154
Cryst Sys trigonal/rhombohedral
Pearson hP9
Wyckoff c a
R Value 0.016
Red Cell P 4.912 4.912 5.403 90 90 120 112.934
Trans Red 1.000 0.000 0.000 / 0.000 1.000 0.000 / 0.000 0.000 1.000
Comments Stable up to 846 K, above P6222, above 1143 K tridymite is stable
Cell from 2nd ref. (Joergensen): 4.9145(6), 5.406(1)
Compound with mineral name: Quartz low
The structure has been assigned a PDF number (experimental powder diffraction data): 46-1045
Synchrotron radiation (powder)
Temperature factors available
Structure type : Quartz,low

Atom	#	OX	SITE	x	y	z	SOF	H
Si	1	+4	3 a	0.4704(4)	0	0.6667	1.	0
O	1	-2	6 c	0.4136(6)	0.2676(6)	0.7857(5)	1.	0

Lbl	Type	Beta11	Beta22	Beta33	Beta12	Beta13	Beta23
Si1	Si4+	0.0059(7)	0.003(1)	0.0043(8)	0.0017(5)	-.002(1)	-.0010(5)
O1	O2-	0.008(2)	0.009(3)	0.009(2)	0.012(3)	-.002(3)	0.0(2)

Std. Notes Transformation Method: Tidy
REMARK Transformed from enantiomorphic space group.--> P 31 2 1
TRANS -a,-b,-c
Std. Cell 4.9124 4.9124 5.4038 90 90 120
Std. Vol. 112.93
Std. Z 3
Std. SG P3121
Std. Atom

Atom	#	OX	SITE	x	y	z	SOF
Si	1	+4	3 a	.52960	0	.33333	1.
O	1	-2	6 c	.41360	.14600	.11903	1.

*end for ICSD #41412

Flourite

*data for ICSD #41413

Coll Code 41413
Rec Date 1999/11/30
Mod Date 2009/02/01
Chem Name Calcium Fluoride
Structured Ca F2
Sum Ca1 F2
ANX AX2
Min Name Fluorite
D(calc) 3.18
Title Electronic and thermal parameters of ions in Ca F2: regularized least squares treatment
Author(s) Strel'tsov, V.A.;Tsirel'son, V.G.;Ozerov, R.P.;Golovanov, O.A.
Reference Kristallografiya
(1988), 33, 90-97
Soviet Physics, Crystallography (= Kristallografiya)
(1988), 33, 49-52
Unit Cell 5.463 5.463 5.463 90. 90. 90.
Vol 163.04
Z 4
Space Group F m -3 m
SG Number 225
Cryst Sys cubic
Pearson cF12
Wyckoff c a
R Value 0.0159
Red Cell F 3.862 3.862 3.862 60 60 60 40.76
Trans Red 0.500 0.500 0.000 / 0.000 0.500 0.500 / 0.500 0.000 0.500
Comments Compound with mineral name: Fluorite
The structure has been assigned a PDF number (experimental powder diffraction data): 35-816
Standard deviation missing in cell constants
Temperature factors available
Structure type : CaF2
X-ray diffraction from single crystal

Atom	#	OX	SITE	x	y	z	SOF	H	ITF(B)
Ca	1	+2	4 a	0	0	0	1.	0	0.502(5)
F	1	-1	8 c	0.25	0.25	0.25	1.	0	0.750(4)

Std. Notes Transformation Method: Tidy
Std. Cell 5.4630 5.4630 5.4630 90 90 90
Std. Vol. 163.04
Std. Z 4
Std. SG FM3-M
Std. Atom

Atom	#	OX	SITE	x	y	z	SOF
Ca	1	+2	4 a	0	0	0	1.
F	1	-1	8 c	.25	.25	.25	1.

*end for ICSD #41413

Hematite

*data for ICSD #66756

Coll Code 66756
Rec Date 1995/10/17
Mod Date 2006/04/01
Chem Name Iron(III) Oxide - Alpha
Structured Fe2 O3
Sum Fe2 O3
ANX A2X3
Min Name Hematite
D(calc) 5.27
Title An XRD study on the structures of ferrites: Hematite, Ba-ferrite and Zn2 Y (Ba3 Zn2 Fe12 O22)
Author(s) Shin, H.-S.;Kwon, S.-J.
Reference Yoop Hakoechi (Journal of the Korean Ceramic Society) (1993), 30, 499-509
Golden Book of Phase Transitions, Wroclaw (2002), 1, 1-123
Unit Cell 5.0342 5.0342 13.746 90. 90. 120.
Vol 301.7
Z 6
Space Group R -3 c H
SG Number 167
Cryst Sys trigonal/rhombohedral
Pearson hR10
Wyckoff e c
R Value 0.012
Red Cell RH 5.034 5.034 5.426 62.361 62.361 60 100.565
Trans Red 1.000 0.000 0.000 / 1.000 1.000 0.000 / 0.667 0.333 0.333
Comments Stable above 773 K (2nd ref., Tomaszewski), below Ia3-, m.p. 1523 K
Compound with mineral name: Hematite
The structure has been assigned a PDF number (calculated powder diffraction data): 01-079-1741
The structure has been assigned a PDF number (experimental powder diffraction data): 33-664
Rietveld profile refinement applied
Standard deviation missing in cell constants
Temperature factors available
Structure type : Al2O3
X-ray diffraction (powder)

Atom	#	OX	SITE	x	y	z	SOF	H	ITF(B)
Fe	1	+3	12 c	0	0	0.3553	1.	0	0.75
O	1	-2	18 e	0.3072	0	0.25	1.	0	0.87

Std. Notes Transformation Method: Tidy
Std. Cell 5.0342 5.0342 13.7460 90 90 120
Std. Vol. 301.69
Std. Z 6
Std. SG R3-CH
Std. Atom

Atom	#	OX	SITE	x	y	z	SOF
Fe	1	+3	12 c	0	0	.14470	1.
O	1	-2	18 e	.30720	0	.25	1.

*end for ICSD #66756

Corundum

*data for ICSD #77810

Coll Code 77810
Rec Date 2003/04/01
Chem Name Aluminium Oxide - Alpha
Structured Al2 O3
Sum Al2 O3
ANX A2X3
Min Name Corundum
D(calc) 3.98
Title Calibratuion of the monochromator bandpass function for the X-ray
Rietveld analysis
Author(s) Riello, P.;Canton, P.;Fagherazzi, G.
Reference Powder Diffraction
(1997), 12, 160-168
Unit Cell 4.7598(1) 4.7598 12.9924(3) 90. 90. 120.
Vol 254.92
Z 6
Space Group R -3 c H
SG Number 167
Cryst Sys trigonal/rhombohedral
Pearson hR10
Wyckoff e c
R Value 0.101
Red Cell RH 4.759 4.759 5.129 62.354 62.354 60 84.972
Trans Red 0.000 1.000 0.000 / 1.000 1.000 0.000 / 0.333 0.667 -0.330
Comments R(Bragg)=0.03
Compound with mineral name: Corundum
The structure has been assigned a PDF number (calculated
powder diffraction data): 01-071-6478
The structure has been assigned a PDF number (experimental
powder diffraction data): 10-173
Temperature factors available
Structure type : Al2O3
X-ray diffraction (powder)

Atom	#	OX	SITE	x	y	z	SOF	H	ITF(B)
O	1	-2	18 e	0.3068	0	0.25	1.	0	0.26(2)
Al	1	+3	12 c	0	0	0.3521(1)	1.	0	0.26(2)

Std. Notes Transformation Method: Tidy
Std. Cell 4.7598 4.7598 12.9924 90 90 120
Std. Vol. 254.92
Std. Z 6
Std. SG R3-CH
Std. Atom

Atom	#	OX	SITE	x	y	z	SOF
O	1	-2	18 e	.30680	0	.25	1.
Al	1	+3	12 c	0	0	.14790	1.

*end for ICSD #77810

Maghemite C

*data for ICSD #87119

Coll Code 87119
Rec Date 2000/07/15
Chem Name Iron(III) Oxide (21.16/31.92) - Gamma
Structured Fe21.16 O31.92
Sum Fe21.16 O31.92
ANX A21X32
Min Name Maghemite C
D(calc) 4.83
Title A study on the structure of maghemite (gamma-(Fe2 O3)). I. Rietveld analysis pf powder XRD patterns
Author(s) Shin, H.-S.
Reference Yoop Hakoechi (Journal of the Korean Ceramic Society) (1998), 35(10), 1113-1119
Unit Cell 8.3457 8.3457 8.3457 90. 90. 90.
Vol 581.28
Z 1
Space Group P 43 3 2
SG Number 212
Cryst Sys cubic
Pearson cP53
Wyckoff e d c2 b
R Value 0.014
Red Cell P 8.345 8.345 8.345 90 90 90 581.284
Trans Red 1.000 0.000 0.000 / 0.000 1.000 0.000 / 0.000 0.000 1.000
Comments Compound with mineral name: Maghemite C
The structure has been assigned a PDF number (calculated powder diffraction data): 01-089-5892
The structure has been assigned a PDF number (experimental powder diffraction data): 39-1346
Rietveld profile refinement applied
Standard deviation missing in cell constants
Temperature factors available
Structure type : Fe21+xO32
X-ray diffraction (powder)

Atom	#	OX	SITE	x	y	z	SOF	H	ITF(B)
Fe	1	+3.017	4 b	0.625	0.625	0.625	0.35	0	0.5
Fe	2	+3.017	8 c	-.0044	-.0044	-.0044	1.	0	0.71
Fe	3	+3.017	12 d	0.125	0.3669	0.8831	0.98	0	0.71
O	1	-2	8 c	0.3817	0.3817	0.3817	0.99	0	0.7
O	2	-2	24 e	0.3817	0.8736	0.8819	1.	0	0.8

Std. Notes Transformation Method: Tidy
REMARK Transformed from enantiomorphic space group.--> P 41 3 2
TRANS -a,-b,-c
Std. Cell 8.3457 8.3457 8.3457 90 90 90
Std. Vol. 581.28
Std. Z 1
Std. SG P4132
Std. Atom

Atom	#	OX	SITE	x	y	z	SOF
Fe	1	+3.017	4 a	.375	.375	.375	.350
Fe	2	+3.017	8 c	.00440	.00440	.00440	1.
Fe	3	+3.017	12 d	.125	.13310	.38310	.980
O	1	-2	8 c	.13170	.13170	.13170	.990
O	2	-2	24 e	.12360	.36830	.36810	1.

*end for ICSD #87119

Rutile

*data for ICSD #109469

Coll Code 109469
Rec Date 2007/08/01
Chem Name Titanium Oxide
Structured Ti O2
Sum O2 Ti1
ANX AX2
Min Name Rutile
D(calc) 4.23
Title Relative merits of reflection and transmission techniques in laboraty powder diffraction
Author(s) Rasmussen, S.E.
Reference Powder Diffraction (2003), 18, 281-284
Unit Cell 4.60099(2) 4.60099(2) 2.96339(2) 90. 90. 90.
Vol 62.73
Z 2
Space Group P 42/m n m
SG Number 136
Cryst Sys tetragonal
Pearson tP6
Wyckoff f a
R Value 0.0876
Red Cell P 2.963 4.601 4.601 90 90 90 62.733
Trans Red 0.000 0.000 1.000 / 1.000 0.000 0.000 / 0.000 1.000 0.000
Comments Data measured in reflection, program GSAS, also results with transmission data reported
Compound with mineral name: Rutile
The structure has been assigned a PDF number (experimental powder diffraction data): 21-1276
Temperature factors available
Structure type : TiO2(tP6)
X-ray diffraction from single crystal

Atom	#	OX	SITE	x	y	z	SOF	H
Ti	1	+4	2 a	0	0	0	1.	0
O	1	-2	4 f	0.30470(26)	0.30470(26)	0	1.	0

Lbl	Type	U11	U22	U33	U12	U13	U23
Ti1	Ti4+	0.00168(3)	0.00168(3)	0.00179(5)	0.00004(5)	0	0
O1	O2-	0.00109(7)	0.00109(7)	0.00118(11)	-.00029(10)	0	0

Std. Notes Transformation Method: Tidy
Std. Cell 4.6010 4.6010 2.9634 90 90 90
Std. Vol. 62.73
Std. Z 2
Std. SG P42/MNM
Std. Atom

Atom	#	OX	SITE	x	y	z	SOF
Ti	1	+4	2 a	0	0	0	1.
O	1	-2	4 f	.30470	.30470	0	1.

*end for ICSD #109469

Appendix 2 – TOPAS Parameters

Appendix 2 provides all the emission and instrument parameters utilised for Rietveld refinement for quantitative XRD using TOPAS 4.2 (Bruker). The addendum for special positions outlined in TOPAS 4.2 is included.

Table A2-1: Emission profile for CuKα

Area	WL (Å)	Lortz. HW (mÅ)
0.0159	1.534753	3.6854
0.5791	1.540596	0.437
0.0762	1.541058	0.6
0.2417	1.544410	0.52
0.0871	1.544721	0.62

Table A2-2: Emission profile for PDB

Area	WL (Å)	Lortz. HW (mÅ)
1	1.000565	0.07231909

Table A2-3: Instrument parameters for D8 Advance

Parameter	Value
Goniometer radii (mm)	250
2Th angular range of LPSD (º)	3
FDS angle (º)	0.3
Source length (mm)	12
Sample length (mm)	25
RS length (mm)	17
Primary soller (º)	2.5
Secondary soller (º)	2.5

Table A2-4: Instrument parameters for PDB

Parameter	Value
Goniometer radii (mm)	217.5
Additional convolution (Hat, Constant)	0.02163356
Additional convolution (Gaussian, Tan(Th))	0.009654902
Additional convolution (Lorentzian, Tan(Th))	0.0001
Additional convolution (Cricles, 1/Tan(2 Th))	0.0001

TOPAS 4.2 Addendum

Special Positions:

It is mandatory to enter a fractional coordinate for a special position in the form of an equation such as

= 1/3, =1/6, etc. in the *Codes* page,

instead of entering a value with re-occuring digits such as

0.3333..., 0.1666..., etc. in the *Values* page.

The correct parameter value will be calculated automatically from the equation and displayed in blue color.

For more details refer to the User's Manual.
Not adhering to this convention may lead to severely wrong refinement results!

Appendix 3 – QEMSCAN Mineral Definitions

Appendix 3 provides all elemental ratios for QEMSCAN phase identification. Note that phases may have question marks as part of the title.

High Iron Mullite

Must Have

Al	45 – 70
Fe	30 – 212
O	30 –140
Si	56 – 20

May Have

C	0 – 30
Ca	0 – 80
Cl	0 – 41
F	0 – 45
Mg	0 – 60
Na	0 – 25
P	0 – 50
Ti	0 – 50

Other Elements: Not allowed

High BSE Crystalline Alumino Silicate

Must Have

Al	120 – 240
Al/Si	1.3 – 4.4
Fe	40 – 120
O	30 – 140
Si	40 – 120
Ti	30 – 120

May Have

None

Other Elements: Low amounts allowed

Low BSE Amorphous Aluminosilicate

Must Have

Al	130 – 360
Al/Si	0.4 – 2
Si	140 – 350

May Have

C	0 – 50
Ca	0 – 50
Co	0 – 40
Fe	0 – 50
K	0 – 50
Na	0 – 40
O	0 – 180
Ti	0 – 50
V	0 – 40

Other Elements: Not allowed

Crystalline Alumino Silicate

Must Have

Al	120 – 240
Al/Si	0.5 –1.4
O	40 – 140
Si	140 – 290

May Have

Fe	0 – 60

Other Elements: Low amounts allowed

Crystalline Aluminosilicate

Must Have

Al	39 – 82
Al/Fe	0.5 – 1.7
Fe	43 – 94

May Have

None

Other Elements: Low amounts allowed

Amorphous Aluminosilicate

Must Have

Al	130 – 360
Al/Si	0.4 – 1.8
O	30 – 160
Si	160 – 350

May Have

C	0 – 50
Ca	0 – 50
Fe	0 – 50
K	0 – 50
Na	0 – 40
Ti	0 – 50

Other Elements: Not allowed

Iron Bearing Amorphous Aluminosilicate

Must Have

Al	35 – 190
Al/Fe	0.8 – 4.6
Fe	15 – 100

May Have

Si	0 – 240

Other Elements: Low amounts allowed

CaD(SiL)

Must Have

Ca	60 – Max
Si	0 – 60

May Have

C	0 – Max
Cl	0 – 50
F	0 – Max
K	0 – 40
Na	0 – Max
O	0 – Max

Other Elements: Not allowed

CaD(FeLMgL)

Must Have

Ca	60 – Max
Fe	0 – 50
Mg	0 – 45

May Have

C	0 – Max
Cl	0 – 50
F	0 – Max
K	0 – 40
Na	0 – Max
O	0 – Max

Other Elements: Not allowed

Fe_Oxides

Must Have

Fe	250 – Max
O	0 – Max

May Have

C	0 – Max
Cl	0 – 50

Other Elements: Not allowed

CaD(FeL)

Must Have

Ca	60 – Max
Fe	0 – 50

May Have

C	0 – Max
Cl	0 – 50
F	0 – Max
K	0 – 40
Na	0 – Max
O	0 – Max

Other Elements: Not allowed

Fe-CO3

Must Have

Fe	50 – Max

May Have

C	0 – Max
Ca	0 – 60
Cl	0 – 50
F	0 – Max
Mg	0 – 45
Mn	0 – 40
Na	0 – Max
O	0 – Max

Other Elements: Not allowed

Ca-Fe ox/CO3

Must Have

Ca	60 – Max
Fe	50 – Max

May Have

C	0 – Max
Cl	0 – 50
F	0 – Max
K	0 – 40
Mg	0 – 45
Mn	0 – 40
Na	0 – Max
O	0 – Max

Other Elements: Not allowed

SiH(Al)

Must Have

Al	0 – 50
Si	300 – Max

May Have

C	0 – Max
F	0 – Max
Na	0 – Max
O	0 – Max
P	0 – 60

Other Elements: Not allowed

Mullite

Must Have

Al	20 – 384
O	20 – 168
Si	86 – 632

May Have

C	0 – 40
Ca	0 – 50
Cl	0 – 60
F	0 – 40
Fe	0 – 103
K	0 – 110
Mg	0 – 40
Na	0 – 40
Sb	0 – 51
Sn	0 – 168
Ti	0 – 40

Other Elements: Not allowed

Rutile

Must Have

Ti	0 – Max

May Have

C	0 – Max
F	0 – Max
Na	0 – Max
O	0 – Max

Other Elements: Not allowed

SiD(KSn)

Must Have

Si	60 – Max

May Have

C	0 – Max
F	0 – Max
K	0 – 40
Na	0 – Max
O	0 – Max
P	0 – 60
Sb	0 – 73
Sn	0 – 73

Other Elements: Not allowed

SiD(CaL)

Must Have

Si	60 – Max

May Have

C	0 – Max
F	0 – Max
Na	0 – Max
O	0 – Max
P	0 – 60

Other Elements: Not allowed

Mg-Ca-Fe ox/CO3

Must Have

Ca	60 – Max
Fe	50 – Max
Mg	45 – Max

May Have

C	0 – Max
Cl	0 – 50
F	0 – Max
K	0 – 40
Mn	0 – 40
Na	0 – Max
O	0 – Max

Other Elements: Not allowed

SiD

Must Have

Si	60 – Max

May Have

C	0 – Max
F	0 – Max
Na	0 – Max
O	0 – Max
P	0 – 60

Other Elements: Not allowed

SiH

Must Have

Si	300 – Max

May Have

C	0 – Max
F	0 – Max
Na	0 – Max
O	0 – Max
P	0 – 60

Other Elements: Not allowed

Fe(Mg)-CO3

Must Have

Fe	50 – Max
Mg	0 – Max

May Have

C	0 – Max
Ca	0 – 60
Cl	0 – 50
F	0 – Max
Mn	0 – 40
Na	0 – Max
O	0 – Max

Other Elements: Not allowed

Fe ??

Must Have

Fe	50 – Max

May Have

None

Other Elements: Any amounts allowed

Ti-Fe oxide ??

Must Have

Fe	50 – Max
Ti	40 – Max

May Have

None

Other Elements: Any amounts allowed.

Fe-oxides(??)

Must Have

Fe	250 – Max

May Have

C	0 – Max
F	0 – Max
Na	0 – Max
O	0 – Max

Other Elements: Low amounts allowed.

Si(K)??

Must Have

K	0 – Max
Si	0 – Max

May Have

None

Other Elements: Any amounts allowed.

SiH(Fe)

Must Have

Fe	0 – 50
Si	300 – Max

May Have

C	0 – Max
F	0 – Max
Na	0 – Max
O	0 – Max
P	0 – 60

Other Elements: Not allowed.

Al.Fe.Ca.Silic ??

Must Have

Al	50 – Max
Ca	60 – Max
Fe	50 – Max
Si	60 – Max

May Have

None

Other Elements: Any amounts allowed.

Ca-Fe ox/CO3 ??

Must Have

Ca	60 – Max
Fe	50 – Max

May Have

None

Other Elements: Any amounts allowed.

Ca-Fe ox/CO3(??)

Must Have

Ca	60 – Max
Fe	50 – Max

May Have

C	0 – Max
F	0 – Max
Na	0 – Max
O	0 – Max

Other Elements: Low amounts allowed.

Mg-Ca-Fe ox/CO3 (??)

Must Have

Ca	50 – Max
Fe	50 – Max
Mg	45 – Max

May Have

C	0 – Max
F	0 – Max
Na	0 – Max
P	0 – Max

Other Elements: Low amounts allowed.

Fe-CO3(??)

Must Have

Fe	50 – Max

May Have

C	0 – Max
F	0 – Max
Na	0 – Max
O	0 – Max

Other Elements: Low amounts allowed.

Mn Ca (Fe, Al) Silicate

Must Have

Ca	0 – 100
Mn	0 – Max
O	0 – 210
Si	0 – Max

May Have

Al	0 – 100
C	0 – 94
F	0 – Max
Fe	0 – 108
Sn	0 – 82

Other Elements: Not allowed.

Fe.Mn Silicate

Must Have

Fe	0 – Max
Mn	0 – Max
O	0 – 210
Si	0 – Max

May Have

F	0 – Max

Other Elements: Not allowed.

Ca Silicate ??

Must Have

Ca	60 – Max
Si	60 – Max

May Have

None.

Other Elements: Any amounts allowed.

Ca.Fe.Mg Silic ??

Must Have

Ca	60 – Max
Fe	50 – Max
Mg	45 – Max
Si	60 – Max

May Have

None

Other Elements: Any amounts allowed.

Ca.Fe.K Silica ??

Must Have

Ca	60 – Max
Fe	50 – Max
K	40 – Max
Si	60 – Max

May Have

None

Other Elements: Any amounts allowed.

Si ??

Must Have

Si	60 – Max

May Have

Other Elements: Any amounts allowed.

Ti Silicate ??

Must Have

Si	60 – Max
Ti	40 – Max

May Have

None

Other Elements: Any amounts allowed.

Si.Cl ??

Must Have

Cl	0 – Max
Si	0 – Max

May Have

None

Other Elements: Any amounts allowed.

Fe.Mn.Ca Silic ??

Must Have

Ca	60 – Max
Fe	50 – Max
Mn	40 – Max
Si	60 – Max

May Have

None

Other Elements: Any amounts allowed.

Fe.Mn Silicate ?

Must Have

Fe	0 – Max
Mn	0 – Max
O	0 – 210
Si	0 – Max

May Have

F	0 – Max

Other Elements: Low amounts allowed.

Ti ??

Must Have

Ti	40 – Max

May Have

None

Other Elements: Any amounts allowed.

Appendix 4 – Collie Fly Ash: Product Data Sheet

Appendix 4 provides the available Collie Product Data Sheet from Fly Ash Australia.

Product Data Sheet

COLLIE FLY ASH

Collie Fly ash is a natural pozzolan. It is a fine cream/grey powder, which is low in lime content. In itself it possesses little or no cementitious properties. However, in its finely divided form and in the presence of moisture, it will react chemically with calcium hydroxide (e.g. from lime or cement hydration) at ordinary temperatures to form insoluble compounds possessing cementitious properties.

Uses

Collie Fly ash can be combined with other materials to produce high quality and economical results for:

- Pre-mixed concrete
- Stabilised road base
- Roller compacted concrete pavements
- Concrete sub-base
- Conventional concrete pavements
- Roller constructed concrete dams
- Concrete products

Fly ash can also be used as a filler in the manufacture of other products. It has been successfully used in asphalt, rubber and other manufactured products.

Typical Chemical Composition

The following table provides an example of the typical chemical composition of **Collie Fly ash**:

Element	Collie Fly ash
Al_2O_3	26.40%
CaO	1.61%
Fe_2O_3	13.20%
K_2O	0.68%
MgO	1.17%
MnO	0.10%
Na_2O	0.31%
P_2O_5	1.39%
SiO_2	51.80%
TiO_2	1.44%

Test	Collie Fly ash
LOI	0.5%
Fineness	86%
Relative Strength:	
- 28 days	99%
Relative Water	92%
Relative Density	2.59
SO_3	0.21%
Cl^-	0.001%
Available Alkali	0.2%

Technical Features

- Improved workability
- Improved pumpability
- Reduction in heat of hydration
- Improved resistance to alkali aggregate reaction
- Resistance to sulphate attack

Product Data Sheet

COLLIE FLY ASH

- Reduction in permeability
- Reduction in drying shrinkage and creep
- Good carbonation and corrosion protection with appropriate curing

Properties
The three main tests for **Collie Fly ash** are fineness, loss on ignition (LOI) and chemical composition. These are governed by Australian Standards covered in AS 3582.1

- *Fineness:* Fineness measured by determining the wet sieve residue on a 45 micron sieve.
- *Loss on Ignition (LOI):* Loss on ignition provides an indication of the unburnt carbon (coal) present in the ash.
- *Chemical Composition:* The chemistry of an ash affects its performance.

Mix Design
Proposed mix designs using **Collie Fly ash** should be evaluated for performance prior to commencing production.

Availability
Collie Fly ash is delivered in bulk pressure tankers to site.

Storage
The "shelf life" of **Collie Fly ash** is dependent on the storage conditions, as contact with air and moisture will cause deterioration in performance and handling difficulties.

Safe Handling
Avoid generating dust. Wash product off unprotected skin immediately with water. The use of goggles, dust masks, barrier creams and rubber gloves is recommended.

For further safety information consult the Flyash Australia Material Safety Data Sheet for the product.

For more information please contact:

Flyash Australia Pty Ltd
ABN 68 002 840 271

Level 1, 564 Princes Hwy
Rockdale NSW 2216
PH: (02) 9597 9967
Fax: (02) 9597 9901
Email: sales@flyash.com.au

Appendix 5 – Images of Dilatometer Samples

Appendix 5 provides all photos of post heating dilatometer samples (UFA GP, SFA GP, MFA GP, NM-UFA GP, NM-SFA GP AND NM-MFA GP).

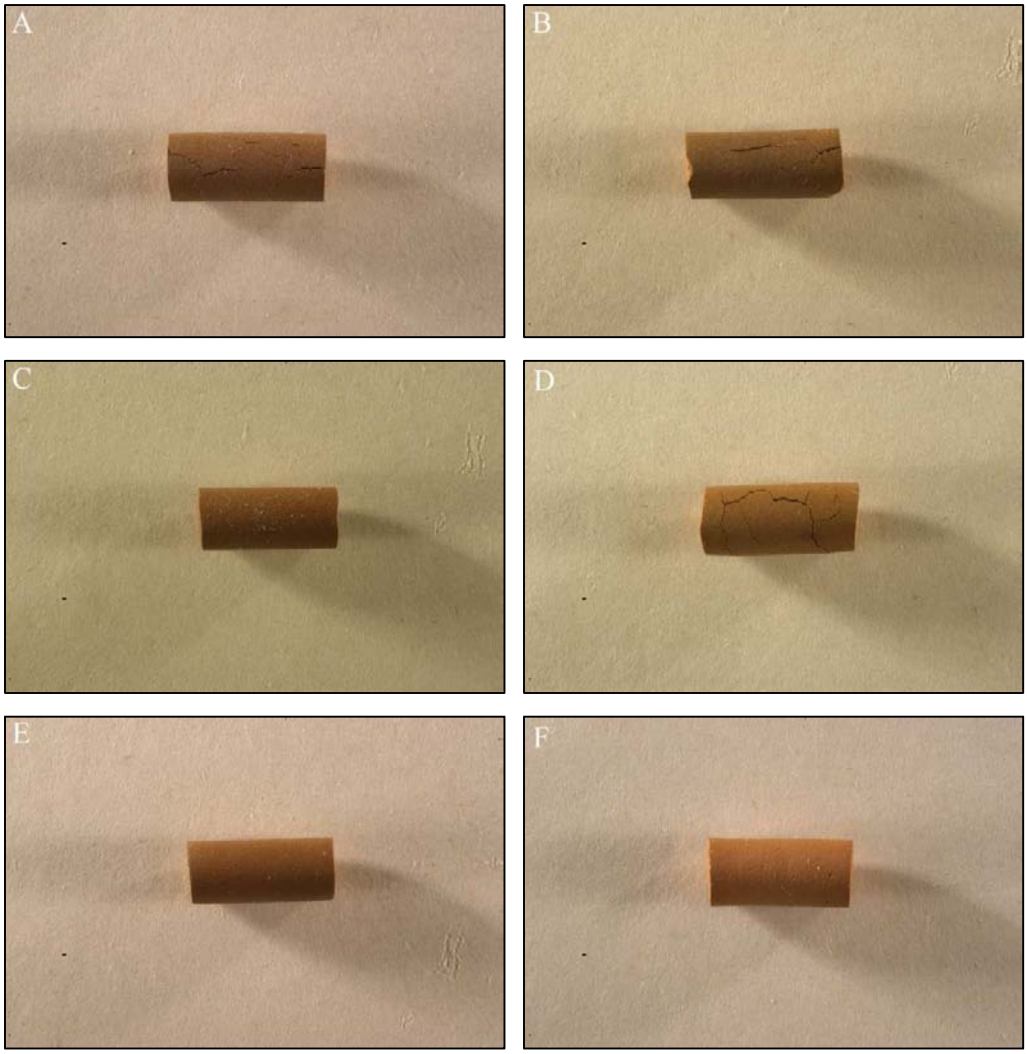

Figure A3-1: Images of heat treated geopolymer using (A) UFA, (B) SFA, (C) MFA, (D) NM-UFA, (E) NM-SFA and (F) NM-MFA.